STRUCTURE, ELECTRONIC LEVELS, AND IONIC INTERACTIONS OF 1 NANOMETER SILICON PARTICLES

BY

KEVIN ANDREW MANTEY

DISSERTATION

Submitted in partial fulfillment of the requirements
for the degree of Doctor of Philosophy in Physics
in the Graduate College of the
University of Illinois at Urbana-Champaign, 2011

Urbana, Illinois

Doctoral Committee:

Professor Robert Clegg, Chair
Professor Munir Nayfeh, Director of Research
Professor David Ceperley
Professor John Stack

Abstract

Silicon particles are created via anodic or platinum catalyzed etching of bulk silicon. A peroxide and HF etchant provides uniform surface termination, and results in discrete stable sizes for particles below 3 nm in size. The smallest of these are 1 nm silicon particles, which is amenable to first principles quantum calculations of the structure, electronic levels, and ionic interactions. The vibrational modes of several candidate structures of the 1 nm particles are calculated at the Hartree-Fock level, and compared to previously acquired Raman spectra to determine the structure. The vibrational modes are also compared to the vibrational structure in low temperature photo-luminescence to indicate surface reconstruction bonds play a role in the fluorescence. The fluorescence mechanism is explored further with calculations of the excited state potential energy surface using time dependent density functional theory, which show radiative traps accessible via direct excitation at the band edge of the ground state geometry. The self-trapped excitons proposed by Lannoo et al. [1, 2] are found to be unstable for the Si29H24 structure, with the outer-well leading to non-radiative recombination via conical intersection of the excited state with the ground state. Absorption measurements indicate the silicon nanoparticles may form charge complexes with iron ions in aqueous solutions. Calculations including solvation effects provide a proposed structure for the complex, with a binding energy of 0.49 eV. The binding mechanism is quite general and suggests many other ions could form charge complexes with the silicon particles in aqueous solutions, potentially leading to new applications.

Acknowledgments

I would like to thank my adviser Munir Nayfeh for his support and the many discussions that helped guide this project. His upbeat approach and ability to view potential difficulties from multiple angles have helped me learn more along the way. I also would like to acknowledge the other members of the lab. In particular, the experimental Raman and low temperature photoluminescence data from Satish Rao played an essential role in comparing to calculations in this thesis. I would also like to thank former and current group members Adam Smith, Tuan Hoang, and Matt Stupca whose help and collaboration was invaluable.

Gratitude is also extended to Sahraoui Chaieb and his student Chris Holt for guidance, collaboration, and discussion regarding the silicon nanoparticle interactions with salt solutions. Chris' enthusiasm and support for interesting side projects also helped me gain a fair amount of eclectic electronic hardware experience which helped during job searching. I very much enjoyed those projects.

I would also like to thank John Stack who has been the physics graduate student director during most of my time at UIUC. His understanding and support are very much appreciated. As much of my financial support came from teaching assignments, I am also grateful he gave me the opportunity to teach a large variety of classes including upper level discussion sections and labs.

Finally, I owe a great deal of gratitude to the numerous friends I've made at Urbana-Champaign during my time here. It would be futile to try to list everyone here, and the adventures they have enabled. Hopefully there are many more adventures to come as well. Please know that I am forever grateful for all you have shared with me. Thank you.

Table of Contents

Chapter 1

Introduction

Crystalline silicon is the workhorse material for modern electronic devices. Continual increases in the capability to use silicon efficiently in manufacturing integrated circuits has lead to an exponential growth in the density of active components in devices for over half a century now [3]. This drive for ever smaller components has led to an increased need to understand the properties of silicon in nanostructued form.

A significant deviation from bulk properties was found in 1990 when L. T. Canham noticed visible photoluminescence in porous silicon he produced via chemical etching of bulk silicon [4]. This was unexpected as bulk silicon is an indirect gap material, which means the lowest energy electronic transition requires not only a photon but also a change in crystal momentum with a phonon produced or absorbed. Therefore efficient recombination of electron hole pairs, and hence photo-absorption or emission, are suppressed by the momentum selection rule. Since the etched pores and resultant networks of silicon structures were on the nanometer scale, Canham hypothesized that the structures were small enough to allow quantum size effects to significantly affect the band structure of the silicon. This discovery has since generated considerable interest in the physics of confined semiconductor structures.

One important length scale in semiconductor materials is the radius of the Bohr exciton, where an electron excited to the conduction band is bound to the positively charged hole left in the valence band, in analogy to a hydrogen atom with the vacuum replaced by the crystal field. For bulk silicon this length is about 4.3 nm [5]. Therefore investigating structures of silicon approaching this length scale should intuitively lead one to find marked deviations of electronic properties from bulk. Such deviations are often referred to in the literature as 'quantum confinement effects'.

Since the first observation of strong luminescence in porous silicon, the search for confinement effects in nanostructured silicon have led to several

interesting discoveries which are already being exploited to make improved devices. In effectively '1-dimensional' silicon nanowires the thermo-electric properties have been found to be greatly enhanced and have been proposed for use toward efficient conversion of electricity from waste heat [6] [7]. In '2-dimensional' silicon thin films, dependence of the optical band gap on silicon phase and composition allow improvements in photo-voltaic devices [8]. This work will be focusing on effectively '0-dimensional' silicon nanocrystals below the bulk exciton size.

The study of these effects in porous silicon was complicated by the randomness of the etching and the sponge like network connecting the smallest structures in the porous silicon. The non-uniformity of the etching on the small scale is what allowed the porous silicon to form in the first place. However this very same effect also made it difficult to discuss the local configuration of the smallest structures, where the greatest confinement effects should occur, for many different configurations would result from the etch. Additionally, the thin network in the sponge itself may exhibit confinement effects.

In 1992, Heinrich et al. used sonication to remove nanocrystals of silicon from the porous network[9]. By applying ultrasonic waves to the porous silicon while immersed in a solvent, he could break off nanoparticles and suspend them in the solvent. This is a 'from bulk' method in contrast to other popular means of producing silicon nanoparticles which are 'bottom up', such as creating particles via laser ablation where particles condense from a plume of ablated atoms[10], induced growth from silane gas [11], silicon ion implantation in oxides or PECVD growth of Si rich oxides followed by annealing [12], or even wet chemistry techniques involving reduction of silicon salts in solution [13]. However these processes incorporated silicon dioxide or other impurities into the particles including structural defects producing non-crystalline particles. The 'from bulk' method of Heinrich et al. had the advantage that the particles were etched from bulk and thus retained their crystalline structure. Additionally, the hydrofluoric acid based etching used to form the porous silicon should produce a hydrogen passivated surface, which was confirmed with FTIR spectroscopy. The disadvantage was that the excessive sonication necessary, along with the non-uniformity of the porous silicon etching process, led to a very wide range of particle sizes (from sub-nanometer to greater than a micron). To improve the situation,

this distribution can be narrowed by various size selection methods. While there will still be a distributions of sizes, the configurations could now be approximated as spherical with some average size to allow a more detailed study of their band structure and emission properties.

In addition to the size distribution, another issue of importance was that while the particles had a chemically pure termination on the surface, their surface structure varied. Mono-, di-, and tri-hydride terminations were all present according to FTIR. In 1997, a new etching procedure involving hydrogen peroxide was developed by the Nayfeh group at the University of Illinois which left mono-hydride terminated surfaces [14]. In addition, further investigation showed that this produced spherical particles of preferred sizes [15].

The smallest of these particles is 1 nm and fluoresces blue [16], and will be the focus of this work. The other methods of silicon particle production previously mentioned either cannot produce particles this small, or do not provide these discrete sizes nor uniformity of the interior (crystallinity) or the surface. This enhanced uniformity of our particles provides a great advantage for studying the electronic structure and fluorescence mechanisms of silicon nanocrystals.

In principle, any interactions of the particles with the environment can be used to manipulate the particles or sense details of the environment. The 1 nm silicon nanocrystals produced by our group have already been incorporated into interesting devises. The interaction of the 1nm nanoparticles with UV light has lead to developing the optoelectronic properties into a silicon based UV photo-detector [17]. The charging energy of the particles was used to create charge memory with advantages over that of floating polysilicon gates in normal flash memory [18]. Recent experiments in our group and that of collaborators have shown particular promise for interactions with ions in solutions. They have demonstrated that such interactions can be used to pattern thin films of particles via electro-plating them in the presence of salts [19]. Also of note is an electrochemical device capable of using the particles to sense glucose in the presence of the particles, demonstrating the potential of these silicon nanocrystals in bio-sensing applications [20].

Despite the success of existing applications, these devices were made with little understanding of the underlying interactions with the particles. Furthermore, it is clear that these devices have only begun to touch upon the full

variety of interactions with the environment that can occur. More knowledge of the chemical and electronic structure of these particles is crucial to allow greater diversity of applications and better selectivity in sensing devices. The remaining sections of work will be devoted to discussing computational modelling work and comparisons to light absorption, fluorescence, and scattering experiments performed on the 1 nm silicon nanoparticles. The work presented will investigate the molecular structure of the particles, dynamics in the excited state, and look at the ion interactions with the structure.

Chapter 2

Fabrication of Silicon Nanocrystals

The silicon nanocrystals studied in our group are obtained through two different methods, both of which can produce particles on the order of a nanometer in size. The methods are similar in that both start with crystalline silicon and involve etching in a mixture of aqueous hydrofluoric acid, methanol, and hydrogen peroxide. The porous silicon is then sonicated in a solvent of choice, resulting in a suspension of silicon nanoparticles. These particles can then be studied directly in solution, or dispersed on a substrate for further investigation.

To provide background information for comparison, first a discussion of previous methods for porous silicon fabrication will be presented. Then the two methods used by the Nayfeh group will be presented. The first method is the most directly related to previous methods as it uses current driven anodization. The second method is an electrodeless method involving a platinum catalyst.

2.1 Porous silicon in previous methods

When strong fluorescence was first observed in porous silicon by Canham, the method of fabricating samples was an anodic cell in aqueous or ethanoic HF [4]. He found formation of fluorescent porous silicon could be obtained in all dopings from n+, n-, p-, and p+ if the etching conditions produced high density porosity. The fluorescence was not observed in material with porous structure too large for one to expect quantum confinement effects, nor was it observed in material made amorphous by defect concentration with ion implantation before anodization. Therefore if fluorescence is desired, a porous silicon fabrication technique can be largely judged by the crystallinity and size scale of the resulting structure.

Investigations into the formation of porous silicon by Beale et al. used

cells in which a 3 inch silicon wafer formed a seal against a chamber of etchant, and the entire exposed wafer surface was used as an electrode through which current was driven [21]. This was to promote as uniform etching across the surface as possible. They found the formation of porous silicon would only occur under anodized conditions, which corresponds to forward biasing with a positive electrode on p-type silicon and negative biasing of n-type silicon. Anodizing was found to occur much easier with p-doped materials.

The dependence of the etching rate on current density reported by Beale et al. found that there is an ideal range. At very high current densities the etchant would uniformly etch and polish, but at low current non-uniform etching would occur creating a rough anodized surface. This may go against intuition, for in many chemical reactions a higher surface area leads to greater area for the chemical process to proceed and therefore increased reactivity. Therefore one may naively expect the increased surface area of the porous silicon to react faster, therefore leading to polishing in slow etching and porous silicon to form only in the non-uniformities that may appear during the driven non-equilibrium conditions in rapid etching. From current and voltage measurements during etching, Beale et al. find evidence that the actual chemistry is most likely quite complex but luckily it appears the etching is determined almost solely by the semiconductor properties and electrolyte interface. The current-voltage measurements indicate that the silicon surface in depleted of carriers. Therefore initial etching pits have a small electrical resistance advantage, which leads to preferred current flow through the electrolyte into the tips of pores and thus etching further into the substrate. Comparing the mass density of the resulting porous film vs current density during etching, it is found that there is less silicon per volume for larger current until it starts etching fast enough to polish instead of form porous silicon. So to get the smallest silicon structures there is an ideal range, with the current density as large as possible before starting to switch to a polishing regime.

In addition to the doping and current density parameters, the final parameter to discuss is the choice of orientation for the single crystal wafers. On a (100) oriented wafer pores form perpendicular to the surface and etch downward [4]. As etching continues these pore enlarge and sometimes branch, forming a sponge like material [21]. The anodic etching appears to have additional dependencies on the crystallographic directions, with Beale et al. noticing crazing along the (110) directions as currently densities were in-

6

creased to near that of polishing conditions. A systematic study of orientation dependence found that pore growth is preferred in the (100) direction, and conversely the (111) surfaces most resistant to etching [22].

2.2   Current driven method

An improved anodization method to fabricate nanometer scale silicon particles has recently been developed [15]. The process starts with a 4 inch diameter prime grade p-type Silicon wafers polished on one side. The wafer has a (100) surface orientation and boron doped to 4-8 Ω-cm. The wafer is then scored with a diamond tip and broken into strips 14 x 17 mm in size. To ensure good electrical contact the wafers are cleaned with acetone, isopropanol, de-ionized water, and then soaked in dilute HF (50:1, de-ionized H_2O to standard 49% concentrated HF) to remove surface oxidation. The strips are then loaded into a teflon array which clamps to each strip a platinum wire firmly along the top long edge of the polished side.

The array is then loaded into a custom built etching system (Figure 2.1). The array sits in the top block which rests on lugs attached to a threaded rod. When the rod is turned by a stepper motor, the top block is lowered. This allows one to lower the silicon strips further into the etchant bath in a teflon basin at a controlled rate.

Etching generates heat so the bottom of the basin is very thin and sits on a heat exchanger. A small bore hole was placed on the side of the basin to a depth that left only a thin teflon separator. This allowed a thermocouple to be placed close to the bath to monitor its temperature. The heat sink is formed from two metal blocks with a serpentine channel cut in it for coolant to flow through. Initially a peltier cooler was placed under the bath to draw heat from the etchant bath to the tap water cooled heat sink. However the heat load the peltier could handle was small and when etching just a few strips, the temperature could swing over 20 deg C. Another issue was the peltier coolers were run near their limit and would eventually fail, which required them to be changed periodically. So the design was updated by removing the peltier cooler entirely, and instead of cold tap water a refrigerated coolant system with a pump was used. The heat sink is now pressed directly against the bottom of the basin with thermal grease.
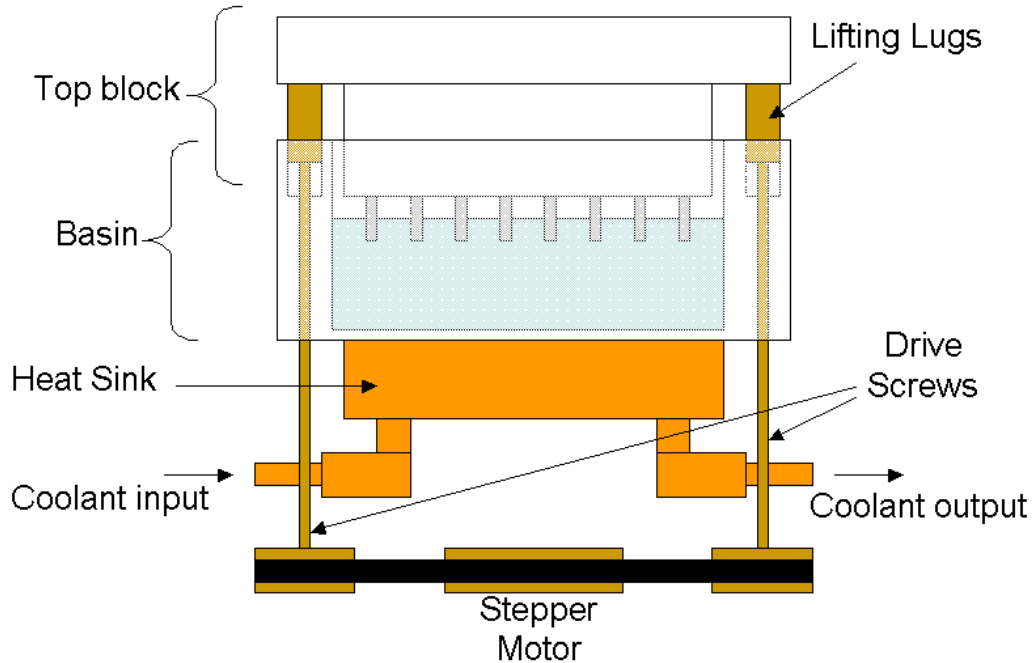
Figure 2.1: Diagram of the etching system. An array of silicon wafer strips is placed in the top block. A stepper motor lowers the strips at a controlled rate into an etching bath in the basin. Refrigerated coolant is pumped through a metal block to remove heat from the bath during etching.

The chilled coolant consists of an ethylene glycol and water mixture to allow safely cooling near the freezing point of water. Common running parameters were: 60-65 mA per silicon strip, coolant running at 2 deg C, with the thermocouple reading of the bath reporting 15-20 deg C during etching. With this enhanced heat exchange capability 5 strips could be etched at the same time with the thermocouple reading increasing only about 5 deg C during an hour of etching.

The chemical bath and electrical configuration for the anodization is summarized in Figure 2.2. The etchant is a solution of hydrofluoric acid, methanol, and hydrogen peroxide in a ratio HF : CH_3OH : H_2O_2 = 1:2:3 by volume of standard commercially available concentrations (while the methanol can be purchased pure, non-fuming aqueous HF has a standard concentration of 49% HF , and hydrogen peroxide was purchased as an aqueous solution of 30% H_2O_2). A current source is attached to the silicon strip and a platinum electrode in the etchant bath, with the positive voltage terminal on the p-doped silicon. The dopant level of the silicon is low enough that its resistivity is less than the etchant solution. This means the current is strongly
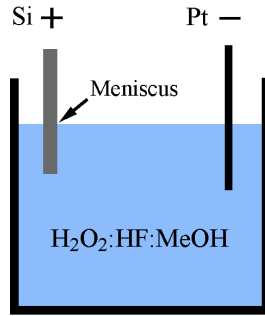
Figure 2.2: Simplified view of etching setup. Current is driven through a silicon strip, then the etching solution, to a platinum electrode also in the solution. The solution is a 1:2:3 ratio of HF : CH$_3$OH : H$_2$O$_2$ which has a lower resistivity than the silicon, so the current and etching is focused on the meniscus.

focused at the meniscus of the solution. This allows current densities of $\sim 100~mA/cm^2$ to be achieved [23].

The purpose of lowering the strips into the etchant bath at a controlled rate is to slowly sweep this etching across the surface of the silicon strip producing a uniform etch. Typically an etch would be performed for 60-90 minutes with the strips lowered at a rate of 3 mm/hr. Etching longer than this starts reducing the smaller structures in the porous silicon eventually giving a mostly polished surface. After the etching is complete the array of strips is removed, rinsed in de-ionized water, then isopropanol and dried. The strips are then placed in a solvent of choice and sonicated for 10 minutes. Large chunks of porous silicon will settle to the bottom leaving a suspension of nanocrystalline silicon in the solvent. Samples are passed through 50 nm filters to ensure the removal of any larger pieces.

The peroxide is a strong oxidizer and increases the etching rate by partially oxidizing the bulk silicon surface, which is quickly removed by the hydrofluoric acid [24]. The peroxide also increases the pH, reducing the available hydrogen ions in solution. While the detailed kinetics of the reaction are unclear, the peroxide/HF etchant preferably leaves behind mono-hydride terminated surfaces. This is evidenced in FTIR spectra by a strong increase in the mono-hydride vibrational modes along with an almost complete elimination of the di- and tri-hydride vibrational modes [14]. The primary purpose of the methanol is to reduce surface tension and bubbling during etching.
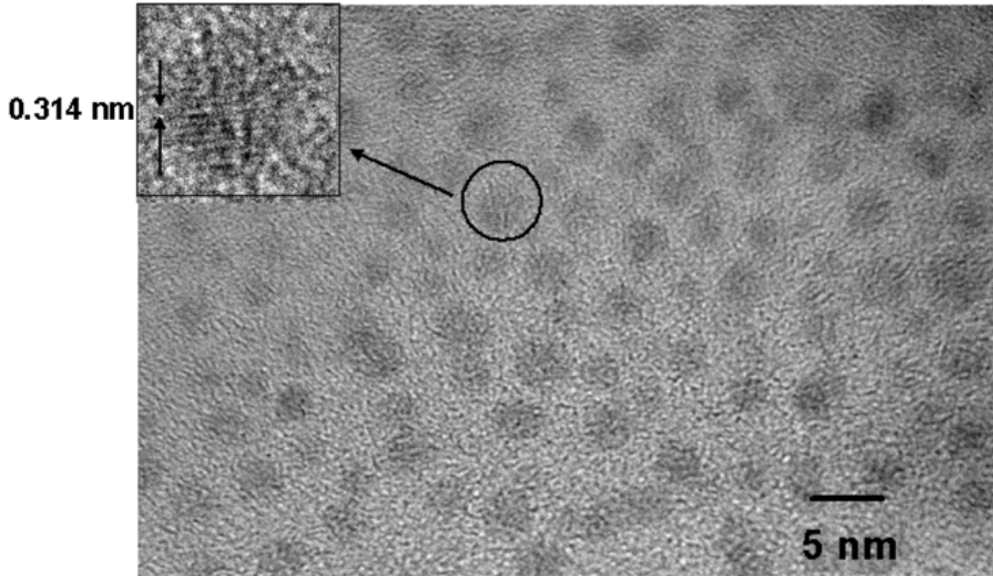
9

Figure 2.3: A high resolution TEM image obtained by Osama Nayfeh et al. of particles created by the anodization system described here using a peroxide and HF etching solution [26]. A lattice fringe spacing of 3.14 Å is visible which corresponds to the spacing of Si (111) planes.

In measuring the resultant particle size distribution using a TEM, it was discovered that the peroxide with HF etching solution produced spherical particles with preferred sizes [15]. Below about 3 nm the size distribution became peaked in discrete sizes of 1 nm, 1.7 nm, 2.2 nm, 2.9 nm. The smallest size exhibits fluorescence in the blue (410 nm), with the emission wavelength increasing for the larger particles through green, yellow, and red (650 nm).

The distribution can be tuned by changing the current source during etching [25]. Larger currents shift the distribution toward the smaller sizes. While this does not allow precise enough control to obtain just one intermediate value, at larger currents it is possible to obtain predominantly the smallest of the discrete sizes: the 1 nm particles.

Figure 2.3 shows particles created with this etching method which Osama Nayfeh et al. dispersed on a carbon TEM grid [26]. These particles were created at a lower current to obtain primarily 2.7 nm particles suspended in isopropanol . The particles have low defect density as the lattice fringing can clearly be seen, with no obvious oxide capping visible. Previous studies have shown via x-ray photo-spectroscopy in a TEM that oxygen is nearly
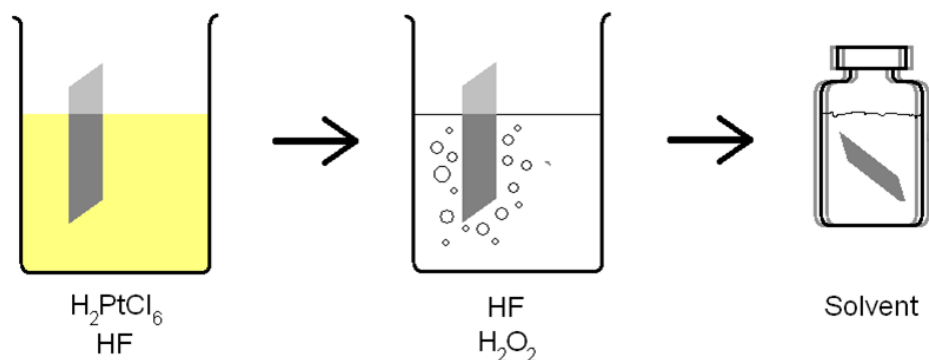
10

Figure 2.4: Overview of particle fabrication with Pt catalyst. A strip of silicon is first treated in a solution of hexachloroplatinic acid, then etched in a solution of hydrogen peroxide and HF, and finally sonicated in a solvent of choice.

absent on the particles, and shown lattice fringing clearly visible on particles down to 1.7 nm in size with 1 nm particles being slightly too small to clearly discern internal structure [27]. So crystallinity and the hydrogenated surface is stable enough to last over times necessary to handle and perform experiments. When illuminated by a handheld UV lamp, the fluorescence of samples is still visible to the naked eye after months, indicating the particles created with this method are quite stable and robust in solution.

2.3 Electrode-less platinum catalyst method

The external electrodes of the previous method provided an advantage by allowing the current, and thus etching, to be narrowly focused on the meniscus. This however also causes the disadvantage of requiring a sweep across the surface and the additional machinery to make such a procedure reliably repeatable. It would be beneficial if intense etching could be focused without the need of externally driven current.

A method has recently been developed that uses a platinum catalyst instead of externally driven current [28]. Any piece of crystalline silicon can be used in this method, however it is convenient to use strips of the same wafers used in the previously discussed method. An overview of the process is shown in Figure 2.4. The process involves three steps: a step which plates platinum on the surface, a step which creates porous silicon, and the final step

of sonicating in a solvent of choice to create a silicon nanoparticle suspension.

The plating solution contains hexachloroplatinic acid, hydrofluoric acid, and de-ionized water. A stock solution of hexachloroplatinic acid, initially obtained as a salt, is prepared by mixing 1 gm per 100 mL of water resulting in about a 0.025 M mixture. Then a plating solution is made by mixing in the volume ratio 3:10:27 = H_2PtCl_6:HF:H_2O from the stock platinic solution and 49% concentration HF.

Like the current driven method described previously, the etchant solution contains hydrofluoric acid, hydrogen peroxide, and methanol. However the concentrations are different. This etching mixture is HF:CH_3OH:H_2O_2:H_2O = 2:4:3:3 by volume (again using 49% HF, and 30% peroxide stock solutions).

The full etching procedure starts with a cleaned silicon strip. Then it is soaked in the plating solution for 10-15 min. The strip is then removed and rinsed in water to remove any residual acid. Then it is placed in the etching solution bath for 30 sec. At this point the solution bubbles rapidly indicating etching is occurring. At the end of etching the strip is removed and rinsed in water to remove residual etching solution and stop the reaction. The strip is then rinsed in the solvent desired for the particle suspension, and placed in a vial of the solvent. The vial is sonicated for 10 minutes which breaks up the porous silicon releasing nanoparticles into the solvent. Big porous silicon pieces will settle out, and the remaining solution will be pushed through a 50 nm filter to ensure larger pieces are removed. The resulting silicon nanoparticle solutions fluoresce strongly in the orange and red spectrum, indicating this process succeeds in producing silicon structures small enough to observe quantum confinement effects.

The mechanism of this etching is illustrated in Figure 2.5. During the plating step a spontaneous electrochemical reaction reduces the platinic acid to platinum on the silicon surface. The thermodynamics of the platinum leads to formation of small spherical platinum deposits instead of a uniform layer on the surface. Hydrogen peroxide dissociates on the surface of many metals, including platinum. Therefore when this surface is placed in the etchant solution, rapid dissociation of the peroxide occurs causing the bubbling seen during this step as well as oxidation of the silicon near the platinum deposits. This oxide is continually etched and removed by the hydrofluoric acid, overall allowing the deposits to burrow into the silicon. The rapid oxidation and etching near the platinum causes porous silicon to form on the surface of the
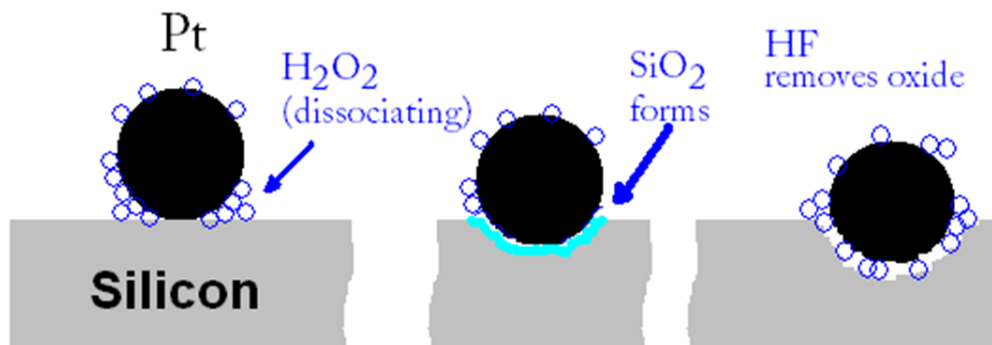
Figure 2.5: The etching mechanism of the Pt catalyst is summarized as follows: peroxide dissociates on the surface of platinum particles, which oxidizes the surrounded silicon, and the oxide is in turn removed by the hydrofluoric acid. This process allows the platinum particles to effectively 'eat' into the silicon.

pores as the platinum randomly eats through the underlying substrate.

The process of the platinum burrowing into the silicon can be seen in SEM images taken of the surface of a sample which was etched for only a couple seconds (Figure 2.6). Many bright platinum deposits can be seen sitting in rounded pits which they have already started etching into the silicon surface. The platinum deposits vary greatly in size from below 0.2 microns to about 1.3 microns. In Figure 2.7 a higher magnification is used to reveal the smallest platinum deposits are about 100 nm in size. After allowing etching for 30 seconds the silicon surface becomes riddled with etching pits (Figure 2.8). Porous silicon forms on the walls of the pits where the dissociated peroxide and HF caused rapid oxidation and etching. In essence, the platinum deposits create intense focused etching, and in this sense plays the role of the current focused on the meniscus in the anodization method.

In order to analyze the resulting nanoparticle sizes, samples created with the Pt catalyzed method were deposited on Cu TEM grids with a formvar support structure. One such grid was prepared via placing a small drop of nanoparticles solution on it and allowing it to dry. As the size of the particles is actually smaller than the thickness of the support structure, achieving good contrast in bright field imaging was difficult. So dark field imaging in a scanning transmission electron microscope (STEM) was used. A detector placed off of the bright field path detects electron scattering as the beam is swept across the sample. As scattering is highly Z dependent this helps
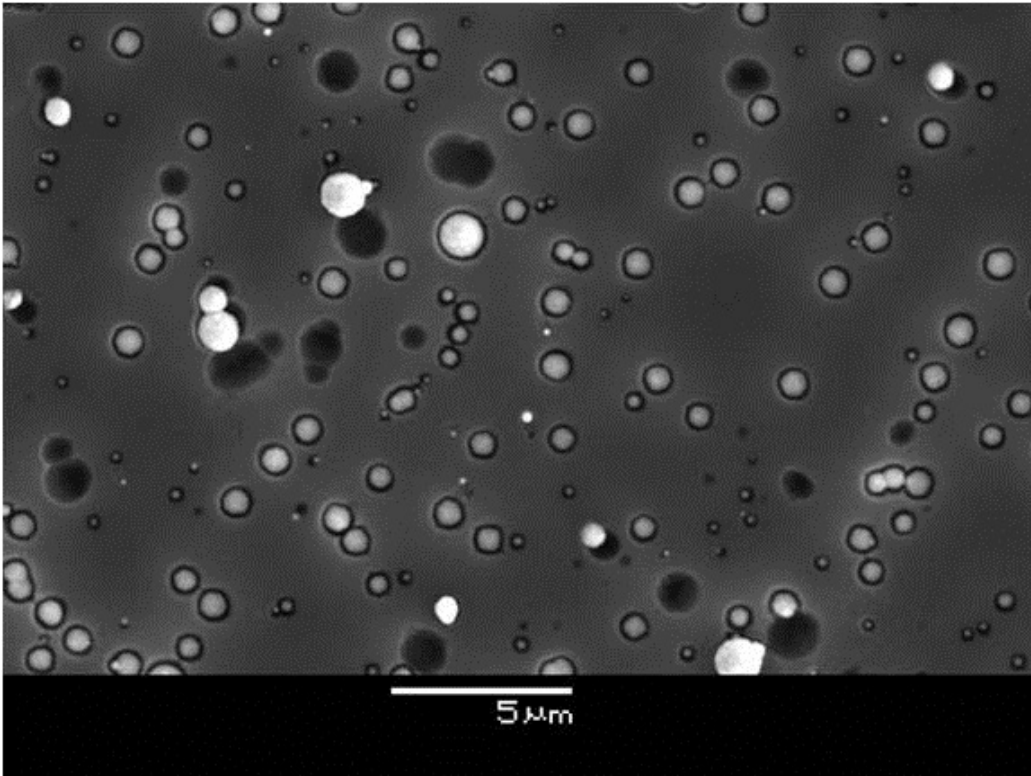
Figure 2.6: An SEM image showing the platinum catalyzed etching, with the platinum deposits burrowing into the silicon surface.
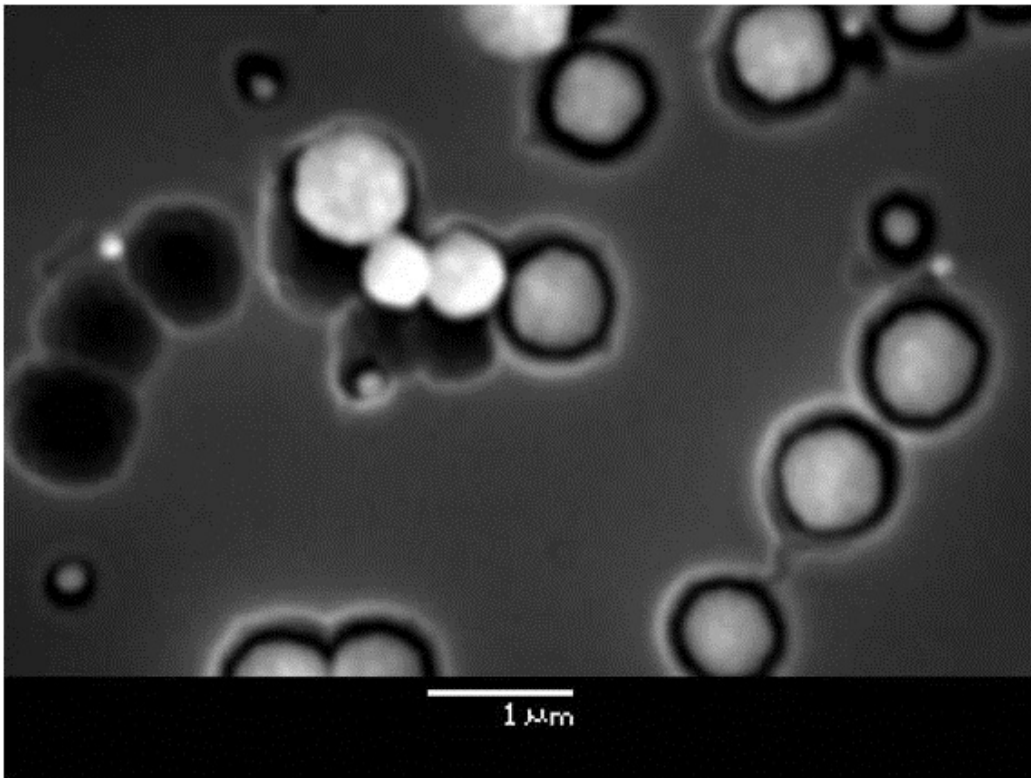
Figure 2.7: An SEM image at higher magnification to highlight some of the smaller platinum deposits.
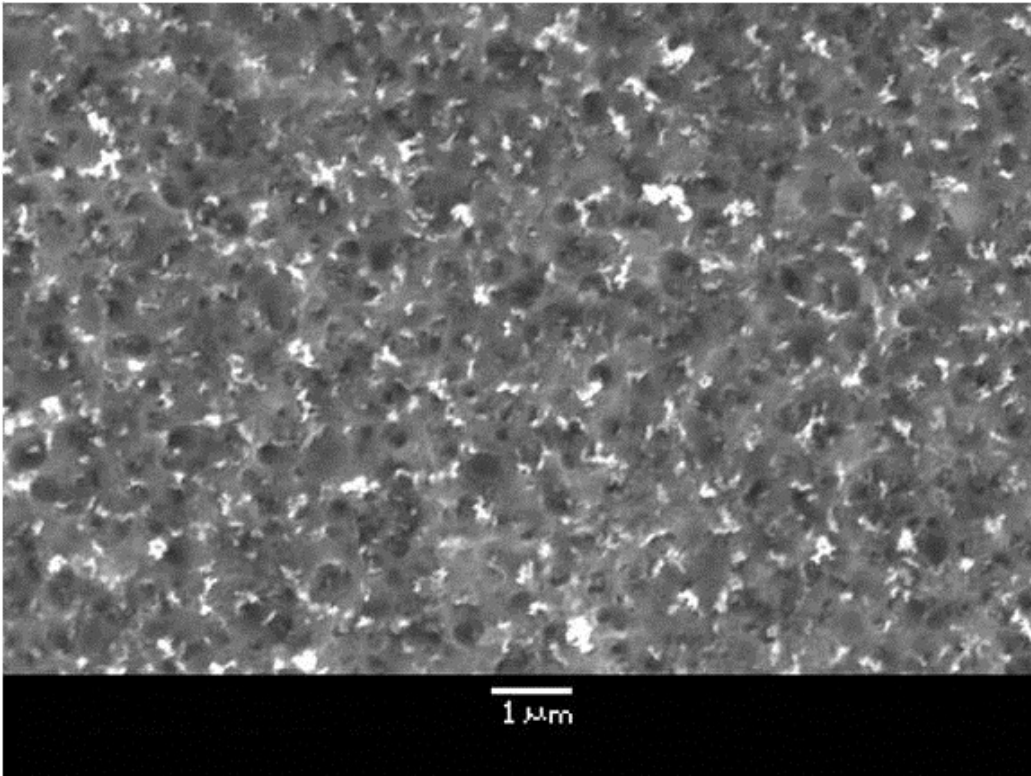
Figure 2.8: An SEM image showing the silicon surface after 30 seconds of etching, resulting in a highly pitted surface covered in porous silicon.
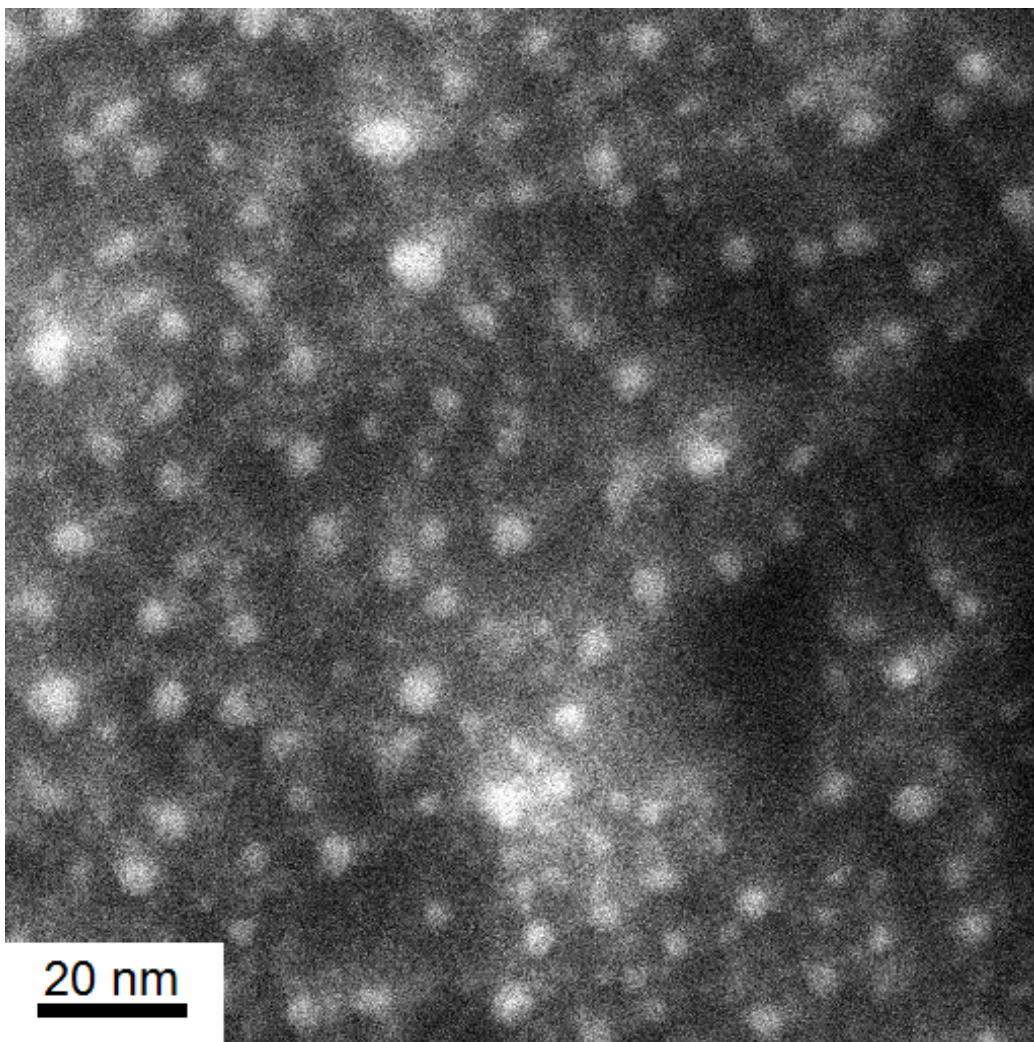
Figure 2.9: STEM image of Si particles created with the Pt catalyst method and drop dried onto a TEM grid. The brighter spots indicate more electron scattering, while dark indicates less.

increase contrast. In Figure 2.9 particles appear predominantly spherical in shape with particles ranging in size from about 6.5 nm down to about 1.6 nm which is near the resolution limit that could be obtained in this image. Further investigation with a grid having a thinner support structure would be necessary to fully investigate the size distribution.

The size distribution using this platinum catalyzed method currently cannot be controlled very well. Therefore to obtain the 1 nm particles studied in the further chapters, the anodization method was used. However the platinum catalyzed method shows promise for a couple reasons. First, it is much quicker than the anodization method. Secondly, because no electrodes are

needed, it can be performed on any crystalline silicon including the silicon dust which is currently just a waste product when cutting wafers from silicon boules [28]. This indicates that the catalyzed etching method may prove to be the best route to manufacturability if silicon nanoparticles are to be used in large quantities in future devices or applications.

Chapter 3

Molecular Structure of 1nm Nanocrystals

The discovery of preferred sizes in the fabrication of nanoparticles leads to the natural question of what makes these sizes preferred, and what is the actual structure of these particles. As discussed in the previous chapter, anodic etching in HF preferentially etches (100) hydrogenated silicon surfaces over (111) hydrogenated silicon surfaces [22]. This indicates the di-hydride termination on the (100) surface is more reactive to the etchant, while the mono-hydride termination on the (111) surface is relatively resistant. Furthermore, the addition of hydrogen peroxide to the etchant was found to increase this selectivity to create porous silicon with near ideal mono-hydride termination [14]. This selectivity is most likely the key to the preferred sizes, for if a spherical chunk of silicon was carved out of a bulk single crystal, every two layers of silicon added to the sphere would result in the surface atoms having predominantly only one dangling bond (in etching, these of course are terminated with hydrogen).

The small size of nanocrystals lends itself well to computational methods. The structure and electronic properties of silicon clusters have been previously studied by numerous methods including tight-binding[29, 1], empirical pseudo-potentials[30], GW-Bethe Salpeter (GW-BSE)[31, 32], density functional theory (DFT) [33, 34, 35], and quantum Monte Carlo (QMC) [36, 37]. However it has been noted that while significant progress has been made in matching computational models with experimental data for clusters larger than 2 nm, there remains difficulty interpreting properties in the smaller regime where the surface atoms become a significant portion of the volume [38]. Indeed previous work has noted that experimentally determined energy levels of particles larger than 2 nm can be fit well even with a simplified 'quasi-particle in a box' confinement model, while smaller silicon nanocrystals do not [27]. This indicates that below 2 nm the molecular nature of the particles becomes increasingly important. Therefore when discussing the
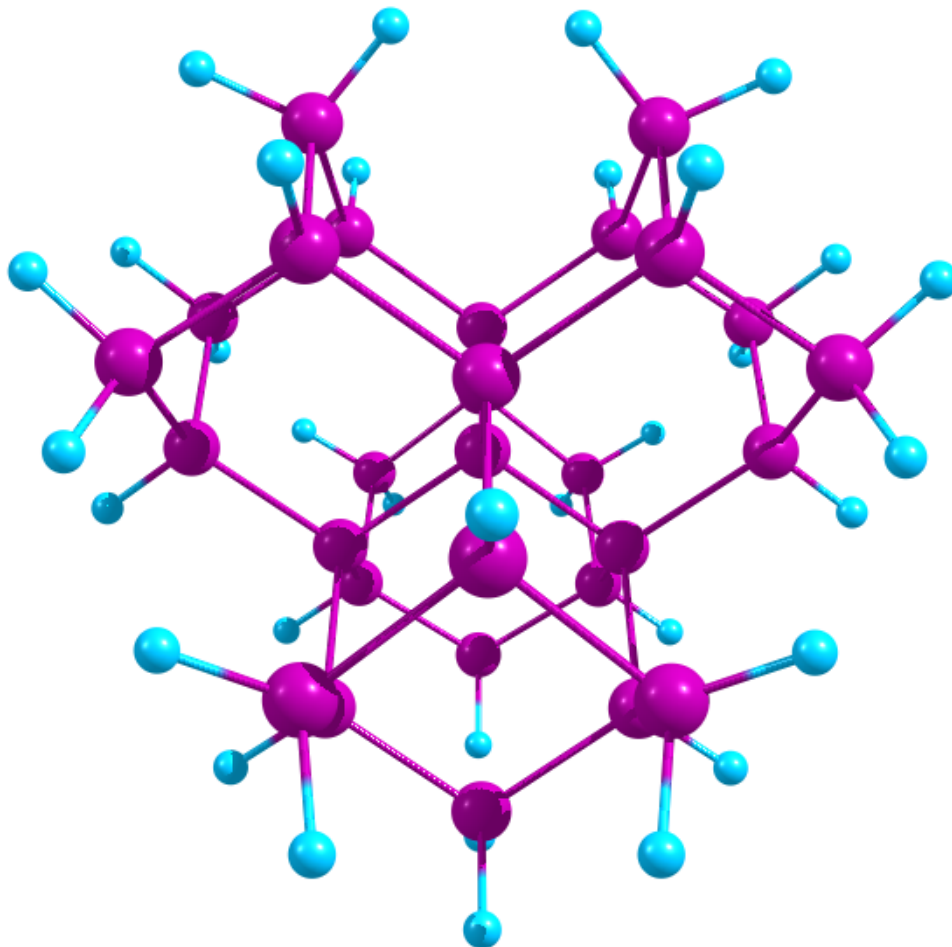
Figure 3.1: $Si_{29}H_{36}$ - 'bulk configuration' 1 nm silicon particle. The silicon atoms (purple) have position similar to that in bulk, with surface bonds terminated with hydrogen atoms (light blue).

smallest of the preferred sizes, the 1 nm silicon particle, an understanding of the surface structure and composition are crucial.

A good starting point for investigating the structure of the 1 nm silicon particle is taking a spherical cut out of bulk and replacing any dangling bonds with hydrogen. The resulting structure, $Si_{29}H_{36}$, will be referred to as the bulk configuration and is illustrated in Figure 3.1. The particle has a tetrahedral core of 5 silicon atoms, surrounded with 24 silicon on the surface of which 12 have single termination and the other 12 have di-hydride termination.

It was argued earlier that there is a strong indication the preferred sizes come from the preference for mono-hydride termination. In the bulk con-
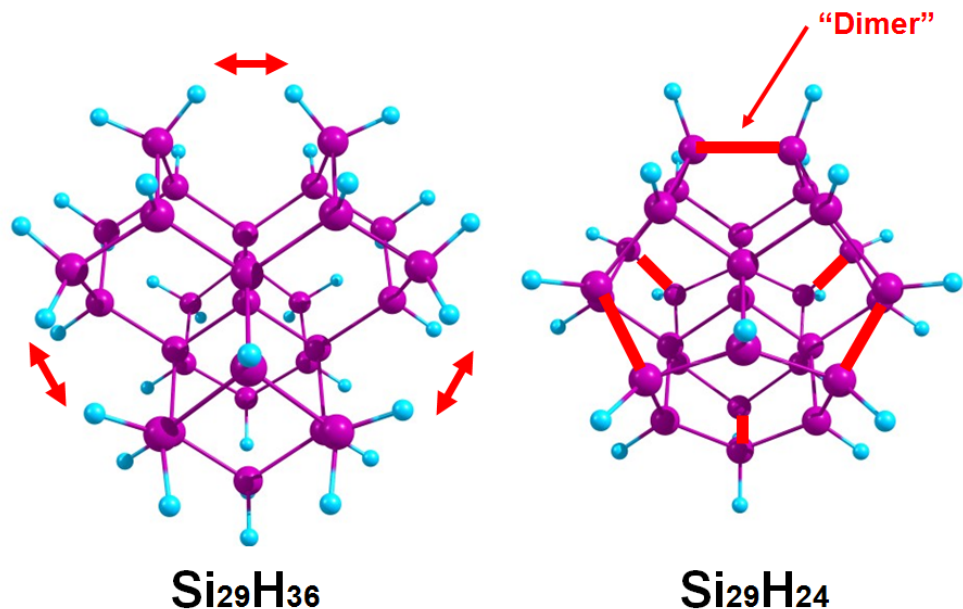
Figure 3.2: Surface reconstruction dimers. For each pair of di-hydride terminated silicon atoms in the $Si_{29}H_{36}$ 'bulk configuration', two hydrogen are removed and the silicon atoms are bonded. This bond is referred to as a dimer.

figuration, the 1 nm particle has just as many mono-hydride and di-hydride surface terminations. This may therefore not appear to be very stable in light of the mono-hydride preference. Compare this however to the structure created by adding just one more layer of silicon atoms to the bulk configuration, which would have 12 di-hydride and 24 tri-hydride terminations.

While there is no spherical cut out of the bulk that will leave only mono-hydride surface atoms, it is possible via surface reconstruction of the bulk configuration to obtain a 1 nm silicon particle with only mono-hydride termination. The 12 di-hydride silicon atoms in the bulk configuration sit such that they form 6 pairs. If two hydrogen are removed from each silicon pair and a bond between them is added, the surface now only has mono-hydride termination. This is similar to a (100) Si surface reconstruction dimer, so such reconstructed bonds are referred to in literature as a dimer (to avoid confusion, please note the reconstructed surface bonds here do not have a double bond nature like in the (100) dimer case, because here the atoms each have a single hydrogen termination as well). This suggested reconstruction is illustrated in Figure 3.2.

To compare possible structures for the 1 nm silicon particle, previous calculations have primarily made predictions and comparisons with the experimental absorbance measurements. In particular, the absorption edge at the 'band gap' energy has been particularly focused on. This band gap was experimentally determined to be 3.5 eV [37].

For the bulk like configuration $Si_{29}H_{36}$ with no surface reconstruction, Delerue et al. [39] calculated a gap ~ 5 eV using a tight binding (TB) method. Using fixed-node diffusion quantum Monte Carlo (QMC) methods, Mitas et al. [37] and Williamson et al. [40, 41, 42] also found the bulk configuration had a band gap larger than the experimental value. Mitas et al. calculated a gap of 4.8 eV, while Williamson et al. reported 5.3 ± 0.1 eV. Time dependent density functional theory (TDDFT) has also been employed by Vasiliev and Martin to predict an absorption edge of 4.2 eV [43].

These initial calculations found the band gap of the bulk configuration to be significantly greater than the experimental value, so various changes in the structure were proposed. It was found that either double bonded Si=O surface oxidation or bridging Si-O-Si oxidation will reduce the band gap according to tight binding [44, 45, 46] and TDDFT [47, 48] calculations. Also surface reconstruction via the formation of one or more dimers will also reduce the band gap according to TB [2, 44], QMC [37], and TDDFT [49, 43].

However there is disagreement in literature over which structure fits best with the experimental evidence. After comparing structures Martin et al. [50] and Mitas et al. [37, 38] conclude the fully reconstructed $Si_{29}H_{24}$ with 6 dimers fits the data best. However more recent reports in 2005 by Lehtonen et al. [51] and in 2008 by Zhanpeisov et al. [52] provide calculations and interpret structures with only bulk configuration and hydrogen termination to be best fits to the data. And most recently in 2009, Garoufalis et al. consider the purely hydrogenated bulk configuration structures to be ruled out although note that surface oxygen in addition to dimers may play a role [49].

To resolve these debates over surface reconstruction, it would be advantageous to turn away from band-gap or absorption predictions and measurements, and use instead a technique which could give a more direct finger print of the surface state itself. If the particles are quite homogeneous in not just size but also molecular structure, it is possible to use Raman spectroscopy of the particles in solution to provide information on vibrational modes of

22
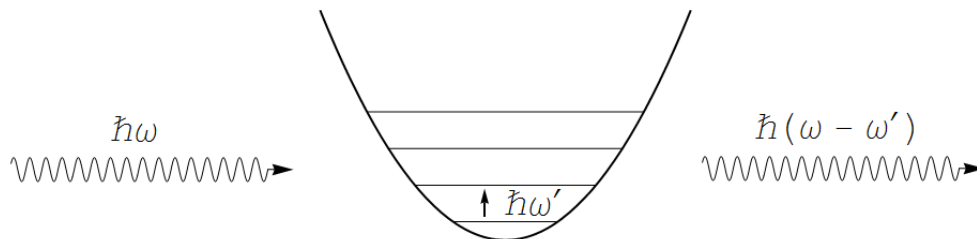
Figure 3.3: Raman Stokes scattering: Incoming light of frequency ω scatters off of a material, exciting a vibrational mode of frequency ω'. The resulting scattered light has a frequency $\omega - \omega'$.

the particles. Such an experiment was successfully carried out by Satish Rao [23], providing measurements of the frequency of Raman active modes and the polarization of light scattering by these modes.

In this chapter, vibrational modes of several potential 1 nm silicon particle structures containing surface reconstruction dimers or surface oxidation will be calculated at the Restricted Hartree-Fock (RHF) level with a 6-311G(d,p) atomic basis. The symmetry of the vibrational modes will be used to determine if they are Raman active, and whether scattering will be unpolarized. Comparison to the Raman measurements of Rao can then indicate which 1 nm structure is preferably created in our etching system.

3.1   Raman scattering

Raman scattering is an inelastic scattering process where light scattering off a molecule transfers energy to or from vibrational modes of the material. If the molecule is excited to a higher vibrational energy, this is referred to as Stokes scattering (Fig. 3.3). At non-zero temperature, even before any external interaction with light, not all of the molecules will be in the vibrational ground state. For the population in an excited vibrational state, it is also possible for the light to inelastically scatter by gaining a quantum of vibrational energy from the molecule while the molecule transitions down one level in vibrational energy. This scattering is referred to as Anti-Stokes scattering.

Raman scattering can be measured by focusing a laser on a solid or liquid sample, and collecting scattered light away from the transmitted or reflected

beam. The scattered light is collected onto a diffraction grating to separate the much larger elastic scattering signal still at the source laser frequency. The diffracted light then falls on a CCD camera allowing measurement of the intensity of the scattered light versus frequency. Because the equilibrium ground state population of the molecules will always be non-zero at any temperature, the Stokes scattering will always be larger and therefore scattered light with lower energy than the laser stimulation is recorded.

The difference in energy between the recorded scattering peaks and laser line therefore provide the energy of vibrations in the molecule. So Raman scattering gives an experimental insight in the molecular structure. In addition to the peak position, by placing polarizers in front of the incident light as well as the scattering detector the degree of polarization that is retained during scattering can provide information about the symmetry of the vibrational mode. However, not all vibrations are Raman active. So before discussing calculations of vibrational modes of different potential nanoparticle structures, first a overview of the theory of Raman scattering will be presented.

Light scattering from a molecule can be adequately treated as an external classical perturbation for our purposes here. With an external oscillating electric field

$$\mathbf{E} = \mathbf{E}_0 \cos \omega_0 t \tag{3.1}$$

this field will induce a dipole μ in the molecule according to the polarizability tensor α.

$$\mu = \alpha \cdot \mathbf{E} = \alpha \cdot \mathbf{E}_0 \cos \omega_0 t \tag{3.2}$$

Since the induced dipole is oscillating it will radiate, which describes the scattered light. Now if the molecule is classically vibrating along a normal mode such that the atomic displacements are given by:

$$q_n = A_n \cos \omega t \tag{3.3}$$

then if vibrational motion of the molecule affects the polarization tensor, classically we can consider separating it into a static term α_0 and a term oscillating with the vibrational motion

$$\alpha = \alpha_\mathbf{0} + \alpha_\mathbf{1} \cos \omega t \tag{3.4}$$

where

$$\alpha_1 = \sum_n \frac{\partial \alpha}{\partial q_n}\bigg|_{q_n=0} A_n \qquad (3.5)$$

Putting this all together yields

$$
\begin{aligned}
\mu &= (\alpha_0 + \alpha_1 \cos \omega t)\mathbf{E} \\
&= (\alpha_0 + \alpha_1 \cos \omega t)\mathbf{E}_0 \cos \omega_0 t \\
&= \alpha_0 \mathbf{E}_0 \cos(\omega_0 t) + \alpha_1 \mathbf{E}_0 \frac{1}{2}\left[\cos(\omega_0 - \omega)t + \cos(\omega_0 + \omega)t\right]
\end{aligned} \qquad (3.6)
$$

The first term is just elastic scattering which is referred to as Rayleigh scattering. The $\omega_0 + \omega$ and $\omega_0 - \omega$ terms are the Raman Anti-Stokes and Stokes scattering respectively. The coefficient α_1 as defined above is equal to the amplitude of the vibrational motion times the derivative of the polarization tensor along the normal mode. The Raman scattering selection rule is therefore: a vibrational mode is Raman active if it changes the polarization of the molecule.

The polarization of the scattered light provides additional information about the vibrational modes. If the incident laser light is polarized, and the scattered light is detected in the plane perpendicular to this polarization, it is possible for the resulting scattering to become depolarized (Fig. 3.4). By placing a polarizer in front of the detector, the scattering intensity $I_\parallel$ parallel to the initial polarization and the perpendicular intensity $I_\perp$ can be measured. Because the molecular orientation cannot be controlled and the absolute scattering cross section is uninteresting here, the spatial average given by the depolarization ratio $\rho = I_\perp/I_\parallel$ is the important resulting factor.

To discuss the polarization of the scattered light, it is convenient to look at the components of the derivative of the polarization tensor along a vibrational mode Q

$$\alpha' = \frac{\partial \alpha}{\partial Q}\bigg|_{Q=0} = \begin{pmatrix} \alpha'_{xx} & \alpha'_{xy} & \alpha'_{xz} \\ \alpha'_{yx} & \alpha'_{yy} & \alpha'_{yz} \\ \alpha'_{zx} & \alpha'_{zy} & \alpha'_{zz} \end{pmatrix} \qquad (3.7)$$

Because the polarization tensor α is symmetric, so is the polarization derivative α'. This means it is always possible to appropriately choose axes to diagonalize the tensor. These coordinate axes are referred to as the principle axes. The tensor can also be decomposed into a fully symmetric term
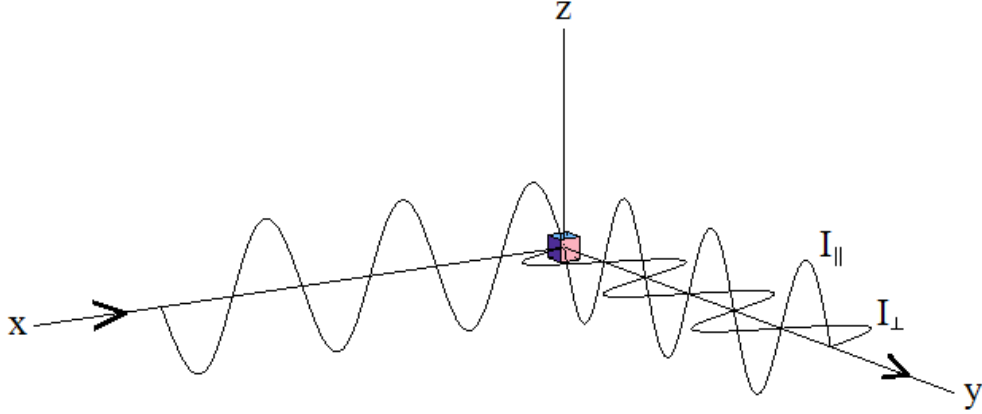
Figure 3.4: Depolarization in Raman scattering: Here light initially linearly polarized in the $\hat{z}$ direction scatters off of material at the origin. The light scattered along the y-axis can have a component of polarization along the original $\hat{z}$ direction and a component perpendicular in the $\hat{x}$ direction. The intensity of light in these polarizations are referred to as $I_\parallel$ and $I_\perp$ respectively, and the depolarization ratio is defined as $\rho = I_\perp / I_\parallel$.

proportional to the identity and the remaining anisotropic part.

$$\alpha' = \alpha'_{iso} + \alpha'_{aniso} \tag{3.8}$$

In the principle axes coordinate system the isotropic part has a magnitude

$$a = \frac{1}{3}(\alpha'_{xx} + \alpha'_{yy} + \alpha'_{zz}) \tag{3.9}$$

while the anisotropic part is characterized by the value

$$\gamma^2 = \frac{1}{2}\left[(\alpha'_{xx} - \alpha'_{yy})^2 + (\alpha'_{yy} - \alpha'_{zz})^2 + (\alpha'_{zz} - \alpha'_{xx})^2\right]. \tag{3.10}$$

After spatial averaging the depolarization ratio ρ is found to be [53]

$$\rho = \frac{I_\perp}{I_\parallel} = \frac{3\gamma^2}{45a^2 + 4\gamma^2} \tag{3.11}$$

Therefore the depolarization ratio is restricted to the range $0 \leq \rho \leq 3/4$.

It should be noted that the previous classical analysis may give a misleading impression of Raman scattering in the quantum mechanics treatment. The main issue is the discussion of vibration itself. The classical analysis al-

lows useful insight and correctly gives details on selecting which vibrational modes are Raman active as well as the range of depolarization ratios. However in quantum mechanics, the different energy levels of a harmonic well is described by a stationary state. There is no oscillating vibrational motion as the expectation value of the nuclear positions is independent of time. Because the classical results are related to the quantum mechanics treatment in the appropriate limit, it should not be surprising that we can obtain an understanding of the scattering requirements and polarization relations from studying the classical picture.

In the quantum treatment of emission or absorption, instead of the classical picture of an oscillating dipole, the relevant quantity is matrix elements of the dipole operator. If there is a non-zero transition moment $\langle f|\hat{\mu}|i\rangle$ between initial state i and final state f, then such a transition is 'dipole allowed' for absorption and emission of photons. In analogy, for a quantum treatment of Raman scattering, the polarizability derivative and vibrational motion of classical treatment is replaced with a matrix element representing the polarization transition moment $\langle f|\hat{\alpha}|i\rangle$.

The polarization operator $\hat{\alpha}$ can be built from a tensor product of the dipole operator and thus the α_{xx} component acts under symmetry operations the same way as the cartesian function xx (and α_{yz} as yz, etc.) [54]. If one knows the symmetry of the initial and final state, it is then possible to predict whether a Raman scattering transition is allowed solely from symmetry principles.

T_d	E	$8C_3$	$3C_2$	$6S_4$	$6\sigma_d$		
A_1	1	1	1	1	1		$x^2 + y^2 + z^2$
A_2	1	1	1	-1	-1		
E	2	-1	2	0	0		$(2z^2 - x^2 - y^2, x^2 - y^2)$
T_1	3	0	-1	1	-1	(R_x, R_y, R_z)	
T_2	3	0	-1	-1	1	(x, y, z)	(xy, xz, yz)

Table 3.1: The character table for the T_d symmetry point group. The five irreducible representations are listed in the first column, and the effect of the symmetry operations of the group listed on the top row are signified by character values in the table. Some Cartesian functions and rotations are given in the last columns to denote their irreducible representation in this point group.

The nuclear positions of $Si_{29}H_{24}$ and $Si_{29}H_{36}$ have T_d point group symme-

try. This symmetry is summarized in Table 3.1. Just as in the simple case that the integral over space of an even function times an odd function will be zero, the integral representing the matrix element $|\langle 1|\hat{\alpha_{ij}}|0\rangle|^2$ can be non-zero only if the irreducible representation products of the final state, polarization tensor, and initial state

$$\Gamma(\psi_1^*) \otimes \Gamma(\alpha_{ij}) \otimes \Gamma(\psi_0) \tag{3.12}$$

contains the irreducible representation of the identity. This representation is A_1 as seen in the table by all the characters equalling one. The ground state will also be in the same irreducible representation as the identity, A_1. The final states after Stokes Raman scattering will have one quanta of vibrational energy more than this ground state. The final state will therefore be in the irreducible representation of the vibrational mode under consideration. Since the components of the polarization tensor transform like binary products of the cartesian coordinates, in T_d symmetry they are represented by A_1, E, and T_2.

The only tensor products of two irreducible representations which contain the identity are the product of each irreducible representation with itself. Therefore the only vibrational modes which will be Raman active in T_d symmetry are represented by A_1, E, and T_2. Furthermore, since A_1 modes have the same symmetry as the cartesian function $(x^2 + y^2 + z^2)$ this means the components of the polarization transition moment will give a depolarization ratio $\rho = 0$ because $\gamma = 0$. Conversely, modes of E and T_2 symmetry will produce maximally depolarized Raman scattering with $\rho = 3/4$ because the isotropic component is zero.

3.2 Hartree-Fock

Hartree-Fock theory is an *ab initio* quantum chemistry method. The starting point is the following Hamiltonian (cast into a dimensionless equation using

atomic units for simplicity)

$$H = -\sum_{i=1}^{N_e} \frac{1}{2}\nabla_i^2 - \sum_{A=1}^{N_n} \frac{1}{2M_A}\nabla_A^2$$
$$-\sum_{i=1}^{N_e}\sum_{A=1}^{N_n} \frac{Z_A}{r_{iA}} + \sum_{i=1}^{N_e}\sum_{j>i}^{N_e} \frac{1}{r_{ij}} + \sum_{A=1}^{N_n}\sum_{B>A}^{N_n} \frac{Z_A Z_B}{r_{AB}} \tag{3.13}$$

N_e is the number of electrons, N_n the number of nuclei, and i, j refer to electrons while A, B refer to nuclei. Note that the Hamiltonian does not include any magnetic interactions. Furthermore, this is non-relativistic, so it is necessary to add the additional requirement that the electron wavefunctions are anti-symmetric to exchange. Solving for the eigenfunctions and eigenvalues of this using analytical methods is intractable. Therefore a series of approximations are necessary to allow solving this in an efficient manner.

The $m_{electron} \ll m_{nuclei}$ (even for hydrogen $\frac{m_{electron}}{m_{nucleus}} < 10^{-3}$). So the electrons will have much larger velocities than the nuclei. To good approximation we can consider the electrons being able to adjust fast enough that at any point in time the electron wave function is the same as if the nuclei were fixed in position. This is the Born-Oppenheimer approximation, and decouples the electron and nuclear wavefunction. That is

$$\psi = \psi_{electron}\psi_{nuclear} \tag{3.14}$$

where $\psi_{electron}$ still depends parametrically on the nuclei coordinates, but only explicitly on the electron coordinates.

The next approximation is the use of the variational method to approximate the ground state. The wavefunction is written as a 'trial wavefunction' depending not only on the electron positions, but also several parameters. The parameters are then varied to minimize the expectation value of the Hamiltonian. As the actual eigenfunctions of the Hamiltonian form a complete set, minimizing the trail function expectation value can be seen as reducing the coefficients of excited states in the actual eigenfunction expansion. The wavefunction obtained using this method is the best approximation to the ground state using the chosen trial wavefunction parameterization. In the limit of an infinite and complete parametrization, the ground state solution is exact.

In practice, a finite parameterization of the ground state wavefunction is of course necessary. The Hartree-Fock approximation, also called the molecular orbital approximation, is to build a trial wavefunction from a slater determinant of molecular orbitals

$$\psi(\mathbf{x}_1, \mathbf{x}_2, \ldots, \mathbf{x}_N) = \frac{1}{\sqrt{N!}} \begin{vmatrix} \phi_1(\mathbf{x}_1) & \phi_2(\mathbf{x}_1) & \cdots & \phi_N(\mathbf{x}_1) \\ \phi_1(\mathbf{x}_2) & \phi_2(\mathbf{x}_2) & \cdots & \phi_N(\mathbf{x}_2) \\ \vdots & \vdots & & \vdots \\ \phi_1(\mathbf{x}_N) & \phi_2(\mathbf{x}_N) & \cdots & \phi_N(\mathbf{x}_N) \end{vmatrix}. \tag{3.15}$$

The molecular orbitals themselves are parameterized as a linear combination of atomic orbitals (LCAO). Often the atomic orbitals are further built from a linear combination of gaussians times cartesian functions in order to simplify integrations. The slater determinant structure guarantees the wavefunction is anti-symmetric to exchange of electron coordinates.

This choice of wavefunction with a product of individual molecular orbitals has no spatial correlation between electron coordinates. So the Hartree-Fock approximation deals with inter-electron interactions by essentially averaging over the molecular orbital. Now each orbital is decoupled in a sense, anf the variational principle leads to the Hartee-Fock equation which is an eigenvector equation for each molecular orbital individually [55].

$$F\phi_i = \varepsilon_i \phi_i \tag{3.16}$$

Where ϕ_i is the ith molecular orbital, and ε_i is its associated energy. The Fock operator F is defined as

$$F\phi_i = \left[\frac{1}{2}\nabla_i^2 - \sum_A \frac{Z_A}{r_i A} + \sum_{j \neq i} (J_j - K_j) \right] \phi_i \tag{3.17}$$

Where J is the coulomb operator and K is the exchange operator defined as

$$J_j \phi_i(r_1) = \left[\int d^3 r_2 \; \phi_j^*(r_2) \; r_{12}^{-1} \; \phi_j(r_2) \right] \phi_i(r_1) \tag{3.18}$$

$$K_j \phi_i(r_1) = \left[\int d^3 r_2 \; \phi_j^*(r_2) \; r_{12}^{-1} \; \phi_i(r_2) \right] \phi_i(r_1) \tag{3.19}$$

Since the Fock operator itself depends on the molecular orbitals, the

equation is non-linear and must be solved iteratively. Some 'initial guess' molecular orbitals are used, the Fock operator is calculated, and then the eigenvectors are solved for with standard linear algebra methods. These new molecular orbitals are used and the process is repeated until it hopefully converges (ie. the orbitals used to build the Fock operator are the same as the resulting eigenvectors). For this reason, the method is called the SCF (Self-Consistant Field) method.

There are more advanced techniques that, instead of using the new eigenvectors directly, use the results of the current iteration along with past results to predict where the final answer is. This greatly reduces the number of SCF iterations necessary. While the math behind these 'convergers' is more complicated, the basic idea behind the method remains the same.

The Hartree-Fock ground state for an N electron system is just the slater determinant of the N lowest energy molecular orbitals.

$$\psi_{HF-GND} = |\phi_1 \phi_2 ... \phi_N\rangle \tag{3.20}$$

The energy of this ground state is not just the sum of the orbital energies. This is because each orbital energy accounts for the interaction of that orbital with all other filled orbitals. So adding them together double counts the electron-electron interactions.

Hartree-Fock ground state (and all individual slater determinants made from the orbitals) have no electron correlation effects. In reality the electrons don't just feel an 'averaged effect' from another electron's orbital. Their positions can be correlated to rarely be near each other, and thus reduce the total energy. This energy is called the correlation energy.

At the level of the Hartree-Fock approximation, the orbital energies do have a physical meaning. For the filled orbitals, the orbital energy is the vertical ionization potential for that electron from the HF ground state. For the unfilled 'virtual orbitals', the orbital energy is the vertical electron affinity (adding an electron to the HF ground state). Note that this is only true for adding or removing one electron, beyond that would be adjusting a state that is not the HF ground state (to get the correct answer it would be necessary to recalculate the orbital energies with one more (or less) electron in the system). The electron affinities calculated this way are however not very accurate as correlation effects are very important in reducing the energy

in negatively charged systems. Comparatively, the HF vertical ionization potential predictions are much better, especially when the ground state is a neutral molecule.

While the absolute energies of the HF ground state itself are not very accurate, the differences in energy between two similar configurations are useful for experimental predictions. As in all levels of multi-electron theory, any question about molecular properties are best phrased in terms of differences between structures. Even minimal atomic basis sets can achieve predictions that on average only deviate from experiment 0.05 Å for bond lengths and $\pm 10°$ for bond angles [56].

Predictions of molecular properties at the HF level can be improved by adding additional freedom to the atomic basis by splitting the valence functions into multiple pieces and adding higher order polarization functions. The double or triple split valence functions gives extra freedom basically allowing the valence functions to contract or expand slightly during application of the variational method. Additional polarization functions, such as p orbitals for hydrogen and d functions for oxygen or silicon, allow better description of the resulting bonds. A triple valence basis with polarization functions can obtain improvements to experimental predictions, bringing bond lengths within 0.02 Å and bond angles to $\pm 3°$ on average. Improvement beyond this accuracy cannot be achieved with larger basis sets, but instead require using methods beyond Hartree-Fock which include electron correlation effects [56].

Once the Hartree-Fock wavefunction is obtained for a particular nuclear position, the gradient of the energy with respect to the nuclear position can be calculated analytically. The equilibrium ground state geometry can then be calculated through an iterative process of calculating the gradient, adjusting the nuclear positions, and repeating until the energy change and nuclear gradient is less than some threshold. If needed, the nuclear wavefunction can be given as a harmonic well approximation of the nuclear position potential energy surface around this minimum.

In quantum chemistry the second derivative of the energy with respect to the nuclear positions is referred to as simply the Hessian. This can be calculated analytically for small molecules, but for larger molecules a numeric differentiation is necessary. This is done by calculating the energy in the equilibrium position, and then for each atom, performing a gradient calculation at a structure with that atom displaced slightly along each cartesian

direction. This provides a straight forward estimate of the Hessian

$$\frac{\partial^2 E}{(\partial q_i)(\partial q_j)} \approx \frac{1}{d}\left[\frac{\partial E(q_i)}{\partial q_j} - \frac{\partial E(0)}{\partial q_j}\right] \tag{3.21}$$

where q_i are the nuclear coordinates, $E(q_i)$ is the energy of the structure with the q_i coordinate displaced by d, and $E(0)$ is energy of the undisplaced structure. This may not produce a Hessian symmetric in i, j and due to finite displacement, the results can also depend on the direction of the displacement.

To improve accuracy, usually a calculation for each of a positive and negative displacement in each cartesian direction is done. Therefore to calculate the Hessian, the gradients are calculated for a total of $6N$ geometries, where N is the number atoms in the structure. The result is:

$$\frac{\partial^2 E}{(\partial q_i)(\partial q_j)} \approx \frac{1}{4d}\left[\frac{\partial E(+q_i)}{\partial q_j} - \frac{\partial E(-q_i)}{\partial q_j} + \frac{\partial E(+q_j)}{\partial q_i} - \frac{\partial E(-q_j)}{\partial q_i}\right]. \tag{3.22}$$

The Hessian is now symmetric by design, and the effects of anharmonic terms are reduced. If the equilibrium geometry has non trivial symmetry, it is possible to reduce the number of calculations further by only doing displacements of symmetry unique atoms.

Errors in the calculation of the vibrational energies from the Hessian come from both mis-calculation of bond strength and the anharmonicity of the potential well [57]. First, Hartree-Fock is known to overestimate the strength of a bond given by the change in energy from stretching a bond. Second, since the energy is quantized and the expectation of x^2 increases with the harmonic mode, the nuclear positions necessarily 'sample' a finite region on the potential energy surface. The anharmonic terms can effect the true frequency.

Comparing calculated harmonic results to experiment shows the error can be largely handled with a systematic scaling factor. A comprehensive study found that the scaling factor for Hartree-Fock calculations is consistent with 0.90, with minimal dependence on the choice of basis set [58][59]. The National Institute of Standards and Technology (NIST) maintains a Computational Chemistry Comparison and Benchmark Database (CCCBDB) which can be used to check the accuracy of vibrational predictions of several computational methods. As an example of a hydrogenated silicon molecule, for

Si$_2$H$_6$ calculations performed using Hartree-Fock with a triple-split valence basis set with polarization functions on the hydrogen and silicon (basis set 6-311G(d,p)) gave predictions for the vibrations with only a rms deviation of 33 cm^{-1} from experiment [60]. A large part of this deviation is from the Si-H stretching modes ~ 2100 cm^{-1}, while all the remaining modes are below 950 cm^{-1}. So a more appropriate comparison of the error may be the percent deviation. The mean magnitude of the percent deviation is about 2.5% for all modes as well as for just the subset of modes below 950 cm^{-1}, indicating this may be a better measure of the error.

3.3 Calculations

Along with the bulk configuration Si$_{29}$H$_{36}$ and the structure with full surface reconstruction Si$_{29}$H$_{24}$, four other potential structures for the 1 nm silicon particle were considered. These six structures are illustrated in Fig. 3.5. As discussed earlier in this chapter, oxidation or surface reconstruction dimers have been predicted to give 1 nm structures a band gap close to experimental measurements. So the structures were chosen to give a variety in the number of dimers and oxygen included. Four structures give a range of surface reconstruction with 6 dimers (Si$_{29}$H$_{24}$), 5 dimers (Si$_{29}$H$_{26}$), 1 dimer (Si$_{29}$H$_{34}$), and no dimers with the bulk configuration (Si$_{29}$H$_{36}$). These can either be viewed as 'missing dimer' defects from the reconstructed structure or dimer defects from the bulk configuration.

Oxidation was considered by addition of bridging Si-O-Si (siloxane) bonds in place of dimers. Other types of oxidation are potentially possible, however the stability of siloxane bonds lends them to being a likely candidate. Another possibility are Si=O (silanone) bonds which have been studied theoretically on 1 nm silicon particles [46, 47], but these were not considered here due to their reactivity. Unlike carbon one row up in the periodic table, silicon does not easily form double bonds. In fact silanone has such high reactivity that the difficulty in preparing stable species with a silanone group has inhibited detailed study of them [61]. Another possible oxidation route are Si-OH (silanol) groups which are much more stable than silanone. However silanol groups are reactive with each other, as this is the basis of silicone polymer production reactions. While silanol species in very dilute solution may rarely

interact, they can react with the surface of glass vials leading to the coating of a glass surface [62]. Therefore when considering stable solutions of silicon particles, siloxane bonds are a likely oxidation method.

The equilibrium geometries for all structures were calculated with RHF (Restricted Hartree Fock) theory using the quantum chemistry computational package GAMESS (General Atomic and Molecular Electronic Structure System) [63, 64, 65] using the 6-311G(d,p) basis set. Restricted Hartree Fock only adds the requirement that every molecular orbital is doubly occupied (closed shell). Since all structures have an even number of electrons, this is reasonable. The 6-311G(d,p) basis set is built from a product of gaussians and cartesian function with a triple split valence set with p-type polarization functions added to hydrogen atoms and d-type polarization functions added to all other atoms. Technically the 'official' 6-311G basis [66] is not defined for atoms beyond Ne, so for silicon it is understood to mean a similarly defined (and standard) basis called MC (McLean/Chandler 'triple split' basis) [67].

From the equilibrium geometries, the Hessian was then calculated through numerical differentiation of analytic gradients. To obtain vibrational frequencies the Hessian must first be converted to 'mass-weighted' coordinates before diagonalizing to get the normal modes. Classically the Hessian can be viewed as the force constant matrix K_{ij} for springs between the nuclei. If the displacement of nuclear coordinate from equilibrium are collected into a vector x, the force on the particle and direction corresponding to x_i is

$$F_i = -K_{ij}x_i = M_{ij}\frac{d^2}{dt^2}x_i \tag{3.23}$$

where summation over repeated indices is implied and M_{ij} is just a diagonal matrix with M_{ii} equal to the mass of the nuclei corresponding to coordinate x_i. After taking the Fourier transform this becomes the matrix equation

$$-Kx = -\omega^2 Mx \tag{3.24}$$

This equation can be cast into an eigen value problem by reforming it as

$$(M^{-1/2}KM^{-1/2})(M^{1/2}x) = \omega^2(M^{1/2}x) \tag{3.25}$$
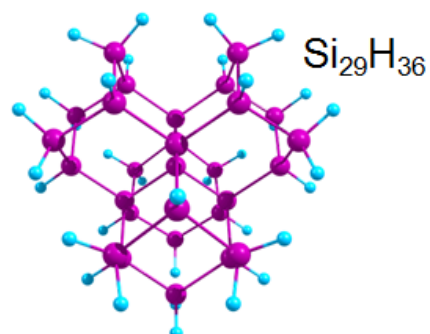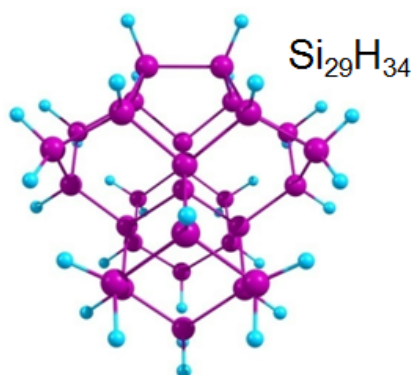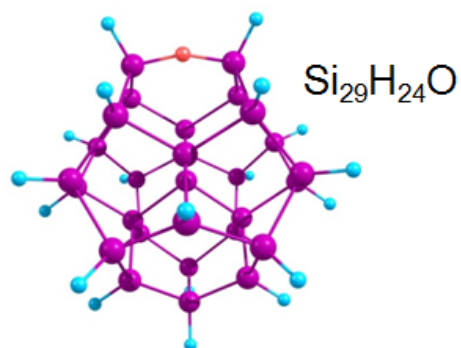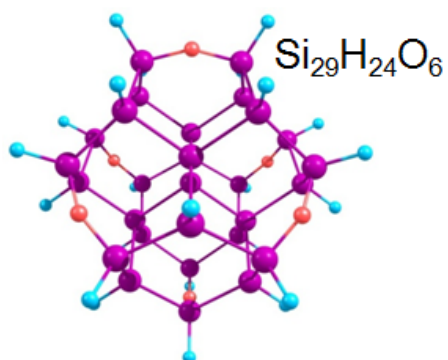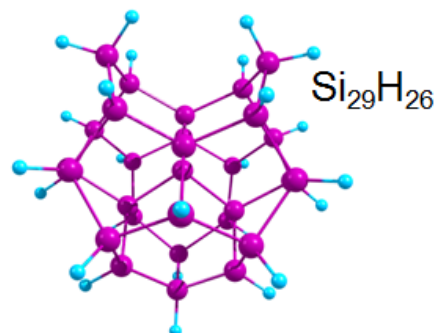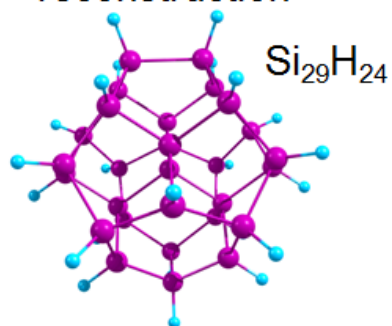
Figure 3.5: Candidate structures for 1 nm silicon particles. The small atoms on the surface with one bond are hydrogen (light blue). The atoms with two bonds are oxygen (red). The largest atoms, with four bonds, represent silicon (purple).

The matrix $M^{-1/2}KM^{-1/2}$ is usually referred to as the Hessian in 'mass weighted' cartesian coordinates. Because the masses are positive and M was diagonal, this matrix is still Hermitian. It is now possible to diagonalize the mass-weighted Hessian to solve for eigen values and eigen vectors to obtain the vibrational normal modes and their associated frequencies.

To determine whether a mode can be Raman active and obtain predictions of the polarization of scattering from such modes, it is then necessary to determine the irreducible symmetry of each mode. Three of the structures being considered have T_d symmetry ($Si_{29}H_{24}, Si_{29}H_{36}, Si_{29}H_{24}O_6$), while the remaining three have C_{2v} symmetry ($Si_{29}H_{26}, Si_{29}H_{34}, Si_{29}H_{24}O$). As the Hessian is Hermitian, the eigenvectors will form a complete basis for describing motion of the nuclei. Therefore if a symmetry operation is written as a matrix C acting on the original cartesian basis of nuclei coordinates, this can be transformed into the vibrational basis. In this new basis the matrix C will be block diagonal relating only modes forming an irreducible representation. For example in the T_d point group symmetry, the representations A_1, E, T_1 are 1,2, and 3 dimensional representations respectively and so 1,2, and 3 modes respectively can be mixed during a symmetry operation. The $N \times N$ sub-matrix block C' from the block-diagonal C relating modes within one N dimensional irreducible representation fully determines the effect of the symmetry operation on that representation. The trace of C' gives the character of that operation for the representation. If the character is determined for each symmetry operation, the representation can then be read directly off the character table.

C_{2v}	E	C_2	$\sigma_v(xz)$	$\sigma_v(yz)$		
A_1	1	1	1	1	z	(x^2, y^2, z^2)
A_2	1	1	-1	-1	R_z	xy
B_1	1	-1	1	-1	(x, R_y)	xz
B_2	1	-1	-1	1	(y, R_x)	yz

Table 3.2: The character table for the C_{2v} symmetry point group. The four irreducible representations are listed in the first column, and the effect of the symmetry operations of the group listed on the top row are signified by character values in the table. Some Cartesian functions and rotations are given in the last columns to denote their irreducible representation in this point group.

This process of identifying the irreducible representation each vibrational mode corresponds to is greatly simplified for C_{2v} symmetry. The character table for the C_{2v} point group symmetry is given in Table 3.2. Because each irreducible representation is one dimensional, there is no need to take the extra step of block diagonalizing the symmetry operation matrix to obtain the dimension of the representation and the corresponding sub-matrix operating on it. Instead each symmetry operation will only have the effect of multiplying the mode by 1 or -1.

In C_{2v} symmetry, every irreducible representation is Raman active. Also, every mode can have depolarized scattering. However representations A_2, B_1, and B_2 can only have maximally depolarized scattering. While representation A_1 can have depolarized scattering, it is the only representation allowing perfectly polarized scattering with $\rho = 0$.

3.4   Comparison to experiment

Raman scattering of 1 nm silicon particles suspended in solution were reported by Satish Rao in 2007 [68]. Solvent Raman peaks restricted the frequency range that the silicon peaks could be clearly distinguished, but four peaks not matching known solvent scattering were observed. Comparing separately fabricated samples in iso-propanol, benzene, and THF, and control samples of just solvent showed that the peaks were repeatable, independent of the solvent, and not a systematic artifact of the measuring setup or quartz cuvettes used to hold the samples.

The four peaks are in the region 250 cm^{-1} - 500 cm^{-1} which the calculations indicate correspond to Si-Si stretching modes. This therefore will allow comparison of all the candidate structures. The summary of the measured peak locations, line widths, and depolarization ratios are given in Table 3.3 from Ref [23].

Without the aid of the vibrational calculations, the relatively strong peak at 485 cm^{-1} could be taken as evidence of oxidation for the Si-O-Si symmetric stretch which is known to be strongly Raman active and lie in the range 450-550 cm^{-1} [69, 70]. To assist in assignment of the modes, the Chemcraft [71] molecular visualization tool was used to animate the vibrational modes. In $Si_{29}H_{24}O$ there was a single Si-O-Si symmetric stretching mode which oc-

curred at 510 cm^{-1} with A_1 representation. In Si$_{29}$H$_{24}$O$_6$ there were six total modes, collected into representations E, T_2, A_1 which frequencies 531, 532, 535 cm^{-1} respectively. So Raman scattering is symmetry allowed from all of these Si-O-Si modes. At a difference of 25 cm^{-1} the calculated vibrational frequency for the singly oxidized structure may be consistent with assigning the experimental 485 cm^{-1} peak to the Si-O-Si stretch. However, for the Td symmetric structure Si$_{29}$H$_{24}$O$_6$ the difference in experimental peak from the calculated oxygen modes is > 45 cm^{-1} ruling out this assignment.

As argued by Satish Rao et al. [68], the 485 cm^{-1} peak is most likely associated with Si-Si vibrations similar to that in the main strong Raman peak from bulk silicon. In bulk silicon the only first order allowed Raman transitions provide a strong peak at 521 cm^{-1} . In amorphous silicon, a broad peak at 480 cm^{-1} also becomes Raman allowed [72]. So there are Si-Si vibrations which are strongly Raman active and it is reasonable to expect one of the resolved peaks for 1 nm silicon particles to be assigned to such vibrations. Theoretical considerations show that the 521 cm^{-1} TO mode peak in silicon should shift to lower energies for nanocrystalline material [73, 74]. Rao found the peak for 2.2 nm silicon particles to shift down to 502 cm^{-1} , and argued the 485 cm^{-1} peak in the 1 nm particles is a further red shift of this mode as the size was reduced, thus assigning this mode to a vibration similar to the TO silicon mode [68]. As a Si-Si peak is strongly expected in this region, and the Raman measurement data for the 1 nm particles shows no other peaks in the 450-550 cm^{-1} region, this assignment is the most straight-forward of the four observed peaks.

With the 485 cm^{-1} peak assigned to an Si-Si mode, the lack of other peaks in the 450-550 region rules out a strong Si-O-Si symmetric stretching peak according to the calculated vibrational predictions. Therefore even

Peak center(cm^{-1})	FWHM(cm^{-1})	ρ
267	17	0.63
292	7	0
315	13	0
485	8	0.74

Table 3.3: Summary of Raman measurements for 1 nm silicon particle from ref [23]. The measured peak positions, width, and depolarization ratio is given for the four resolved peaks.

before proceeding to further peak assignments, the oxidized structures are disfavored by this data.

As a comparison for all the peaks, for each structure the calculated vibrational modes within 40 cm^{-1} of the measured peaks, and which also have a representation in the symmetry group allowing Raman scattering, are shown in comparison to the experimental data in Fig. 3.6 for the T$_d$ symmetric structures. The frequency of each vibrational mode is illustrated with a Lorentzian peak of width 5 cm^{-1} to aid visualization. In both point group symmetries only the A_1 representation can provide polarized Raman scattering, therefore these modes are denoted differently with a black Lorentzian curve as opposed to a grey lorentzian.

In the T_d symmetric case, there are few enough vibrations that can scatter the light without depolarization, that the assignment assuming a particular structure is straightforward. Because the symmetry arguments only tell which modes are symmetry *allowed* to Raman scatter, and not the intensity of the Raman scattering, the calculated vibrational modes listed do not need to each show up in the measured data. Indeed it is clear that each structure has more depolarized Raman allowed vibrational modes than measured peaks in the region. It is likely that these vibrational modes have low Raman scattering amplitude, such that they are below the noise level of the experimental measurement.

The bulk configuration for the 1 nm silicon particle (Si$_{29}$H$_{36}$) is lacking a polarized peak near the measured 292 cm^{-1} peak. The other measured polarized peak at 315 cm^{-1} does not line up well either. The configuration with full surface reconstruction (Si$_{29}$H$_{24}$) fits the spectrum much better, with the only peaks in the 445-525 cm^{-1} region lining up almost perfectly with the measured 485 cm^{-1} peak.

If for each T_d structure the closest depolarized peaks to the measured peaks are chosen in order to represent a best fit, the comparison of fit calculated frequencies to the experimental data is summarized in Table 3.4. It is clear that even in this idealized fit, the bulk structure is disfavored by the data. The oxidized structure fits these four peaks well, but as previously discussed is ruled out due to the experimental data lacking the Si-O-Si peak at 535 cm^{-1} .

For comparison of the vibrational modes in the C_{2v} symmetric structures, each calculated vibrational mode within 40 cm^{-1} of the measured peaks are

Figure 3.6: Raman active modes calculated for Td symmetric structures. The experimental data from ref [23] is shown for comparison at the top, with light gray indicating the scattering of that peak is depolarized, while black indicates polarized peaks. The calculated vibrational modes with symmetry allowed Raman activity are indicated with Lorentzians shaded gray for depolarized and black for polarized peaks.

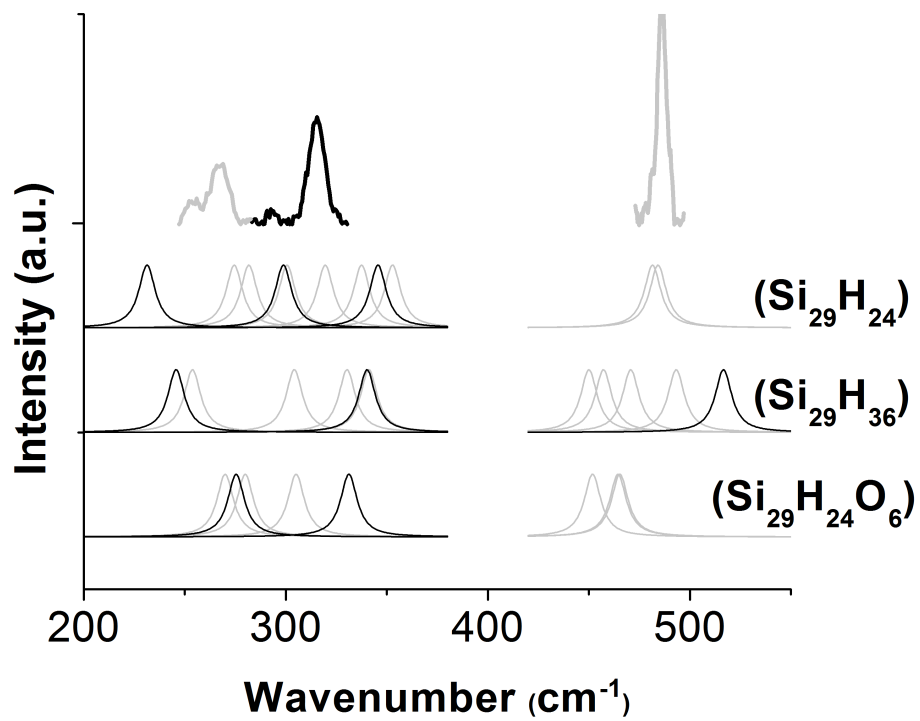Figure 3.7: Raman active modes calculated for C2v symmetric structures. The experimental data from ref [23] is shown for comparison at the top, with light gray indicating the scattering of that peak is depolarized, while black indicates polarized peaks. The calculated vibrational modes with symmetry allowed Raman activity are indicated with Lorentzians shaded gray for depolarized and black for polarized peaks.
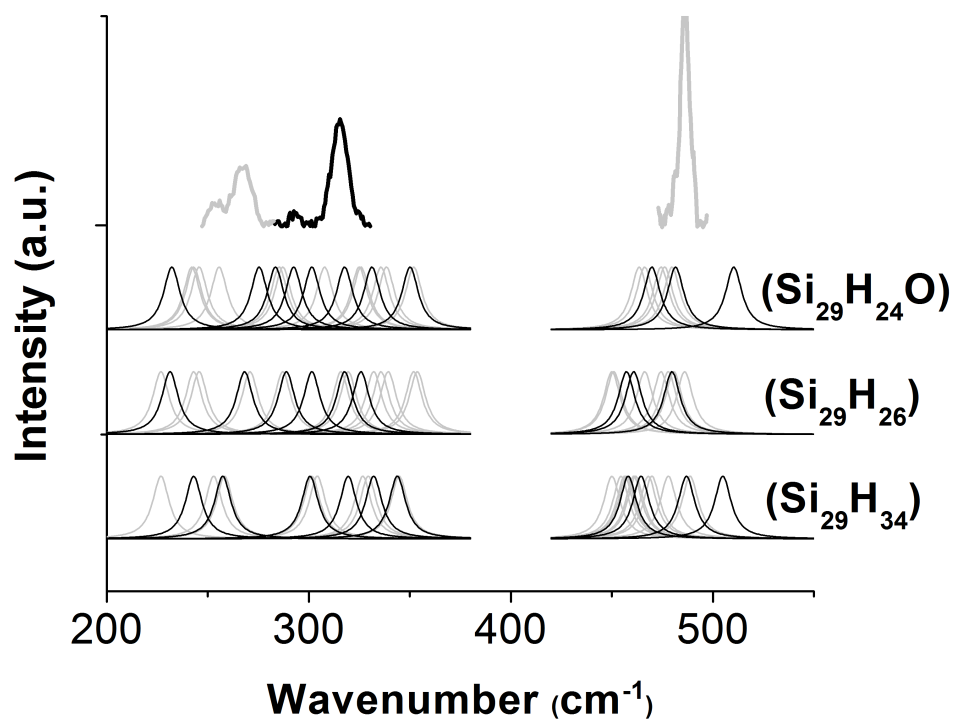
shown in comparison to the experimental data in Fig. 3.7. The representation table for the C_{2v} point group symmetry shows that all representations are symmetry allowed to Raman scatter. Therefore every mode is shown, which in addition to the spread of modes due to these 'defects' breaking the T_d symmetry of the bulk or reconstructed structure, makes the illustration of these modes crowded. As an artifact of the number of possible peaks, if only the calculated modes located by the measured peaks were active, all three structures could fit the spectrum well. However this is unlikely, and the lack of extra peaks in the 445-525 cm^{-1} region makes these structures disfavored in comparison with the data. As noted previously the calculated 510 cm^{-1} peak for Si$_{29}$H$_{24}$O is a Si-O-Si symmetry stretching mode which should be strongly Raman active. Additionally, the Si-Si related modes around 480 cm^{-1} are expected to be strongly active as well. As the 485 cm^{-1} peak is assigned to an Si-Si mode, and amorphous silicon has a broad Raman peak at 480 cm^{-1}, it is unreasonable to expect only one (or a few which happen to lie on top of each other) of the calculated modes in the 480 cm^{-1} 'band' to be active while the others are not despite the vibrations being of a similar nature.

Furthermore, the measured polarization of the peaks indicates the C_{2v} structures are unlikely. The A_2, B_1, B_2 representations can only scatter with maximal depolarization with depolarization ratio $\rho = 3/4$. While the A_1 mode is the only mode that can have perfectly polarized scattering ($\rho = 0$), it can also have any depolarization ratio up to $\rho = 3/4$. In light of this, the

Experiment	Si$_{29}$H$_{24}$	Δ	Si$_{29}$H$_{36}$	Δ	Si$_{29}$H$_{24}$O$_6$	Δ
267	275	8	245	-12	270	3
292	299	7	254	-38	275	17
315	346	31	340	25	331	16
485	485	0	493	8	466	-19
avg $|\Delta|$		12		21		14
rms Δ		16		24		15
avg $|\%\Delta|$		3.8%		7.7%		4.0%

Table 3.4: Experimental Raman peaks compared to best fit computed modes of Td symmetric structures. All frequencies are in units of cm^{-1}. Differences between theory and experiment are included, as well as average magnitude of the deviation (avg $|\Delta|$), the root mean square deviation (rms Δ), and mean percent deviation (avg $|\%\Delta|$).

measured depolarization ratio of 0 for both the 292 and 315 cm^{-1} peaks is anomalous, and more naturally explained by the higher symmetry Si$_{29}$H$_{24}$ structure whose modes of A_1 representation guarantee via symmetry that the depolarization ratio $\rho = 0$.

In conclusion, of the six structures considered, the Raman measurements when compared to the calculated vibrational modes indicate Si$_{29}$H$_{24}$ as the most likely structure for the 1 nm silicon particle. With the surface fully re-constructed with 6 dimers and only mono-hydride termination on the surface, this matches with expectations of the fabrication procedure which involves an etchant that leaves preferably mono-hydride terminated surfaces. Of the six structures the vibrational modes of the bulk configuration Si$_{29}$H$_{36}$ were the worst fit to the measured peaks. This provides independent validation of the claims that Si$_{29}$H$_{24}$ is the more likely structure compared to Si$_{29}$H$_{36}$ based on comparison of measured absorption to a calculated spectra.

Chapter 4

Fluorescence Mechanism

In a semiconductor material there is an energy gap between the conduction bands and the valence bands. Electrons excited into the conduction band will predominantly occupy the states near the bottom of the band, while the holes left in the valence band will collect near the top of the valence band. In a direct gap semiconductor these states have the same crystal momentum, which allows radiative recombination in which an electron in the conduction band annihilates a hole in the valence band with the energy difference released in the form of a photon.

In an indirect gap material such as silicon, the lowest energy conduction band state has a different crystal momentum than the highest energy valence band state. Therefore radiative recombination in indirect gap materials require a phonon to be absorbed or emitted in the process in order to conserve momentum. The necessity of a phonon at a particular momentum suppresses this process in indirect gap materials, and the dominate recombination process is non-radiative. This is why most commercial optoelectronics such as light emitting diodes (LED) are currently made with direct gap III-V materials such as Gallium-Arsenide, Gallium-Phosphide, Indium Gallium Nitride, etc.

When Canham reported strong fluorescence in porous silicon in 1990, he interpreted this as the quantum confinement effects turning nanostructured material into a more direct gap like material [4]. This appears plausible for the 1 nm silicon particles which have an absorption band edge of about 3.5 eV [50, 37], while the direct band gap of bulk silicon is 3.4 eV [75]. In this description, the quantum confinement can be visualized as both lifting up the indirect gap of the conduction band and relaxing the selection rules of radiative recombination, increasingly making the material more direct gap like and thus making the silicon able to interact with light more effectively. It has been argued the momentum selection rules are relaxed by quantum

confinement causing a spread in momentum due to the finite size and the Heisenberg uncertainty principle [76, 77]. In the smallest particles the momentum spread may become large enough that the radiative recombination can occur without a phonon at all.

Since Canham's discovery of fluorescence in porous silicon, more recent reviews of silicon nanostructures point out that the increased radiative recombination rate is actually largely due to a decrease in the non-radiative process, without any large increase in the intrinsic radiative rate itself [78, 79, 80, 81]. In bulk silicon at room temperature kT is greater than the binding energy of the exciton, so electrons and holes are more mobile. This can lead to non-radiative recombination through defect traps in the material. Auger interactions involving an electron hole pair plus an additional hole or electron is the dominant non-radiative pathway in near defect free crystalline silicon [80, 79]. In silicon nanocrystals, the electrons and holes are spatially confined and multiple excitations in a single structure are unlikely therefore greatly reducing the three-body Auger recombination. Additionally while a defect in bulk silicon can cause non-radiative recombination of any excitons that can wander to the trap within its lifetime, a defect on an individual nanocrystal will not cause trapping of excitons created in the other nanocrystals, thereby reducing its effect.

While quantum confinement effects increase the oscillator strength in indirect gap materials, the absorption and emission rates in silicon nanoparticles remain below those of direct gap materials [82]. Radiative lifetimes in direct gap particles can be on the order of picoseconds [79], while the silicon particles even at the size of 1 nm have a fluorescence lifetime of 3 nanoseconds [83] and large nanocrystals can have a radiative lifetime on the order of microseconds to milliseconds [81]. Therefore it has been argued that silicon and other indirect gap materials, retain a sense of their 'indirect gap' nature even as small nanostructures [82, 78, 79, 80, 81].

With the non-radiative transition rate in silicon nanoparticles greatly reduced compared to bulk, the quantum efficiency of radiative recombination can be on the order of 1. This means nanostructured material can potentially provide a path to efficient optoelectronics compatible with current silicon processing [84, 85].

The fluorescence of silicon nanoparticles has also gained considerable interest as a new probe for biological applications [86, 87]. Silicon quantum dots

can be fabricated to provide a range of emission wavelengths [15], are more stable against photo-bleaching than dyes [88], have exceptionally bright fluorescence [89] with twice the brightness of fluorescein (which has a quantum efficiency of about 90%) under the same excitation conditions [90]. Silicon is also expected to be more biologically compatible than direct gap materials with metallic elements like Cadmium, Zinc, or Arsenic. For example Zinc Sulfide nanocrystal have been studied for use as anti-bacterial agents [91]. Even CdSe particles with the surface capped to reduce release of Cadmium were found to be more toxic than silicon particles [92].

The 1 nm silicon particle is ideal for investigating the details of how small silicon nanocrystals fluoresce. As discussed in the previous chapter, the structure of this particle has been the most studied and the predominate molecular configuration created during fabrication has been determined from absorption and Raman scattering measurements. Also it is small enough that the molecular properties can be modelled directly with quantum mechanics methods.

Modelling the 1 nm particle as a molecule should be more appropriate than descriptions in terms of bulk condensed matter such as 'indirect gap' and momentum conservation with phonons. The energy levels of silicon particles larger than 2 nm has been found to match well with a confined exciton model using averaged descriptions of the silicon such as permittivity, and effective electron and hole masses. However this description didn't fit the data for particles below 2 nm [27]. It has also been argued in the study of Raman activity in silicon nanoparticles that the discussion of crystal momentum for particles as small as 1 nm is beyond the appropriate applicable scale for treating nanostructures as a perturbation from bulk [23].

In this chapter, first a brief review of molecular fluorescence will be presented. This is followed by describing a fluorescence mechanism due to the surface reconstruction dimers on silicon particles proposed by Lannoo, Deleue, and Allan. Time dependent density functional theory (TD-DFT) calculations will be presented which investigate this dimer method for the $Si_{29}H_{24}$ nanoparticle. Lastly, to investigate the relaxation of the molecule in the excited state a more detailed study of the excited state potential energy surface will be presented.

4.1 Molecular fluorescence

The discussion using the bulk approach in the previous discussion can be largely rephrased to the molecular picture by introducing some molecular terms. The top of the 'valence band' is called the highest occupied molecular orbital (HOMO), while the bottom of the 'conduction band' is referred to as the lowest un-occupied molecular orbital (LUMO). The direct or indirect band gap energy is therefore referred to as the HOMO-LUMO gap. Since there is no translational symmetry anymore, the notion of crystal momentum no longer applies and electronic states are labelled by their symmetry and energy but not momentum. The radiative recombination of a hole and electron is now seen as a transition between total energy states of the molecule which results in the emission of a photon.

Photoluminescence is the excitation of a substance by absorbing light and the subsequent re-radiation during de-excitation. The details of this process are illustrated in Fig. 4.1. The absorption of a photon will transition a molecule from the ground state to an excited electronic level of the same spin. This process is a vertical transition, meaning that the nuclear coordinate do not change since according to the Franck-Condon principle the electronic transitions are essentially instantaneous relative to the time scale of nuclear motions. In most cases after excitation the excited molecule will transition through the relatively closely spaced excited states to the lowest excited singlet state. This transition to the S_1 state is called internal conversion, and occurs quickly on the time scale of 10^{-12} seconds [93]. Internal conversion results in Kasha's Rule [94] which states that the fluorescence emission spectra will be largely independent of the excitation wavelength.

The molecule will remain in the lowest singlet excited state until either a non-radiative radiative process transitions the molecule in a lower state, or fluorescence occurs which results in vertical transition to the ground state with an emission of a photon. Possible non-radiative processes include a resonant energy transfer to another molecule via dipole-dipole interactions, dynamic collisional quenching, charge transfer to another molecule, or intersystem crossing which leaves the molecule in a triplet state.

The transition from a triplet state to a singlet state is a spin forbidden process as it violates the $\Delta S = 0$ selection rule. Therefore the triplet state is usually long lived. This transition is not completely forbidden though,
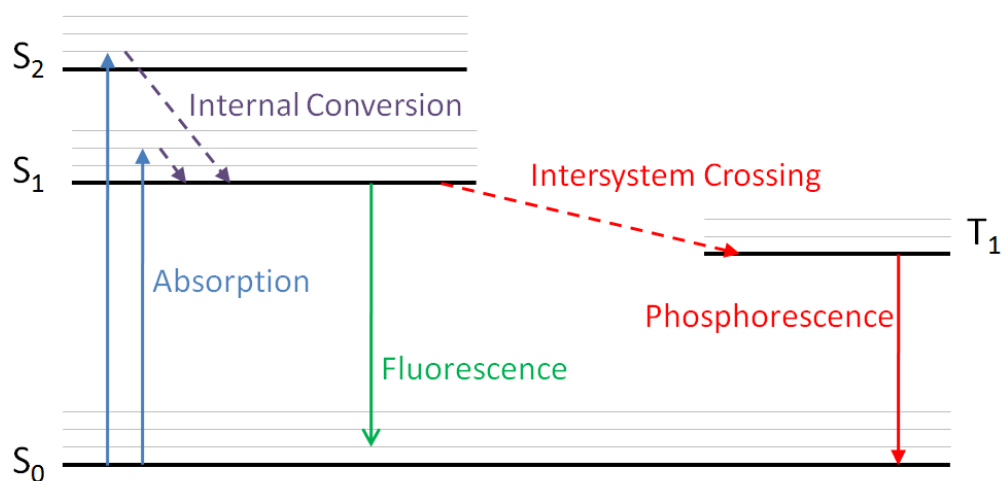
Figure 4.1: Absorption and emission processes. The labels S_0, S_1, S_2, T_1 represent the singlet ground state, first and second singlet excited states, and the first triplet excited state respectively. The multiple light grey lines correspond to the nuclear vibrational states in each electronic level. After absorption of a photon, internal conversion will predominantly bring the state to the lowest singlet state. The state can evolve by transitioning to the ground state and emitting a photon (fluorescence), or transition to a triplet state (intersystem crossing) which can then emit a photon (phosphorescence).

eventually allowing the emission of a photon and a transition to the ground state. This emission is referred to as phosphorescence. Intersystem crossing and phosphorescence is facilitating by the presence of heavy atoms which have larger spin-orbit coupling terms.

Because the absorption and emission processes are vertical transitions, the change in state will rarely occur between the minimum vibrational states of each electronic level unless the minimums on the nuclear potential energy surface happen to occur at close to the same nuclear coordinates. An excited state is usually created in a molecule by exciting an electron to an anti-bonding molecular orbital, thus intuitively fitting the picture of the excited molecule being slightly less 'bound'. It is common for the molecular equilibrium nuclear coordinates to be different in the excited state. While small compared to a dissociation event, the change is large enough to make the most likely transitions for absorption to be an increase in vibrational state as well as the electronic level.

Like absorption, the emission transition is also nearly instantaneous relative to the time scale of nuclear motions, and thus is a vertical transition as well. This means the brightest fluorescence transition is often not to the lowest vibrational state in the ground level. The full cycle of this process of interacting with a photon and eventually returning to the initial state is illustrated in Fig. 4.2. The molecule will absorb a photon, relax in the excited level, then emit a photon, and relax in the ground level. The difference between the excitation frequency and the emission frequency is called the Stokes shift, and is due to the relaxations after each vertical transition.

One source of the relaxation after a vertical transition has already been discussed, internal conversion to lower vibrational states. Another source is due to the surroundings of the molecule when it is in a solvent. An excited state of the molecule will often have a different charge distribution and dipole moment than the ground state. After a vertical transition the average solvent arrangement around the molecule will relax to a lower energy state in response to the change in charge distribution. This relaxation will occur in all solvents, but can be enhanced in solvents with large permittivity or of polar nature.
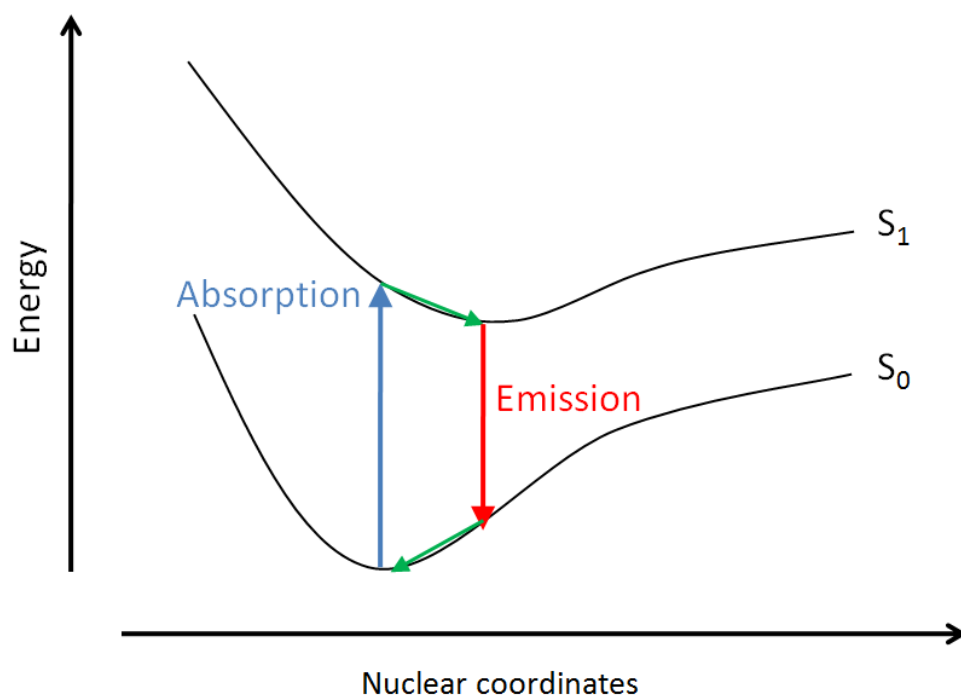
Figure 4.2: Vertical excitation from the ground state is followed by relaxation in the excited state, due to internal conversion and solvent rearrangement. After emission, relaxation will then occur in the ground state. This causes the emission frequency to be lower than the absorption frequency, the difference of which is referred to as the Stokes shift.

4.2 Proposed surface dimer role in fluorescence mechanism

Allan, Delerue, and Lannoo proposed a mechanism for fluorescence in silicon nanocrystals that involves the surface reconstruction dimers playing a primary role [2, 1]. They argued that while the calculated band gaps for silicon nanocrystals are in agreement with experimental data, the large Stokes shift (about 1 eV for 1.5 nm particles) suggests a deep trap aids radiant recombination. In particular they investigated a model where a weakened bond in the excited state permits a new local minimum in a stretched state. In this outer-well they postulate the exciton will become localized on this bond, which they call a self trapped exciton (STE). The localized nature of this excitation will lead to an increase in the radiant recombination rate.

The surface reconstruction dimer bond moves the surface atoms closer together than their position in the bulk configuration. In the limit that the bond is dissociated, the atoms should return to a longer separation equilibrium close to the bulk value. So the dimer bond is a likely candidate for the type of 'outer-well' minimum on the excited state potential surface to allow for a self trapped exciton.

In the molecular orbital picture, an isolated system of two atoms with a single covalent bond can be represented by σ bonding orbital filled with two electrons and an empty σ^* anti-bonding orbital. Optical absorption will promote one electron to the σ^* anti-bonding orbital, leaving the atoms with essentially no binding. This bond weakening can lead to dissociation. However, if the atoms were part of a cluster, the remaining bonds will prevent dissociation if the bond is weakened or even broken. Therefore it is predominantly the other atoms in the cluster that shape the outer-well.

For the excitation to become localized or 'self trapped' this outer-well must become stable. The possibility of this trapping, is shown schematically in Fig. 4.3. The excited state will have a minimum in a nuclear coordinate configuration similar to the ground state. For illustration purposes if this is represented with a harmonic well, and the weakened bond outer well is also represented with a parabola, then the bond length at which these two parabolas cross will represent the point at which the nature of the bond is changing. How these curves intersect determines if a stable outer-well is
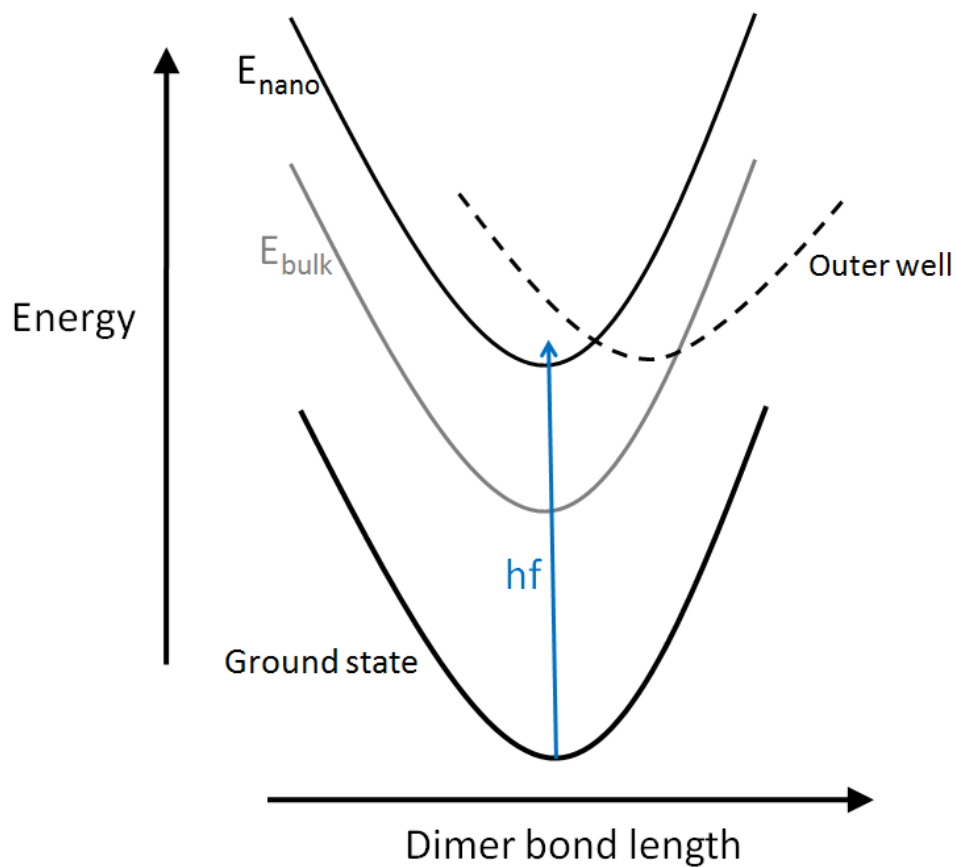
Figure 4.3: The band gap increases in nanoparticles compared to bulk, raising the excited state level from E_{bulk} to E_{nano}. If there is an outer equilibrium position when the bond is sufficiently weakened or stretched, and the excited state level is raised enough, it is possible to form an a double well in the excited state. This allows the formation of a 'self trapped' exciton.

possible. As shown in the figure, in bulk it is possible that the transition point only appears as a kink (relatively quick change in slope) in the excited state potential energy surface. If the band gap is raised sufficiently high by quantum confinement effects, the transition point in the bond nature can become a saddle point in the excited state surface, with the formation of a new local minimum in the outer well.

Allan et al. investigated this proposal on the 1 nm silicon nanoparticle $Si_{29}H_{34}$. This structure is the bulk configuration with one pair of hydrogen removed to create a single surface reconstruction dimer. For a given dimer length, they optimized the geometry by allowing the other nuclear coordinates to relax. The ground and excited states were calculated with Local Density Approximation (LDA) density functional theory and by tight binding calculations. A double well structure was found (Fig. 4.4). It is known that LDA underestimates the excited state energy by a consistent amount, so the LDA results include a 0.6 eV energy shift to compensate [1]. Despite the empirical nature and parameter optimization for much larger structures, and the tight binding calculations match the LDA calculations very well. One can also observe a kink in the ground state curve, which likely indicates where the bond nature transitions. It is only in the excited state that an outer well forms.

The formation of an outer well is encouraging, but for the proposal to work the radiative rate must also increase. Allan et al. calculated the radiative lifetimes of the excited state at varying dimer lengths for a 1.67 nm hydrogenated nanocrystal with 123 silicon atoms. Again a double well was found in the excited state and the lifetime varies by several orders of magnitude along this coordinate path (Fig. 4.5). A sharp increase in the radiative rate is seen near the transition point as well as an increase near the minimum of the outer-well.

A potential difficulty in this proposed mechanism is the height of the barrier connecting the two wells, which is about 0.5 eV for both the 1 nm and 1.67 nm silicon particles considered. Using the energy curves of the 1 nm silicon particle calculated by Allan et al., the transition to the outer well due to thermalization or tunnelling was studied by Nayfeh et al. [95]. The thermal activation time was calculated to be on the order of microseconds. However, due to the outer well actually being lower in energy for the 1 nm particle, there is no vibrational mode that is fully localized on the inner
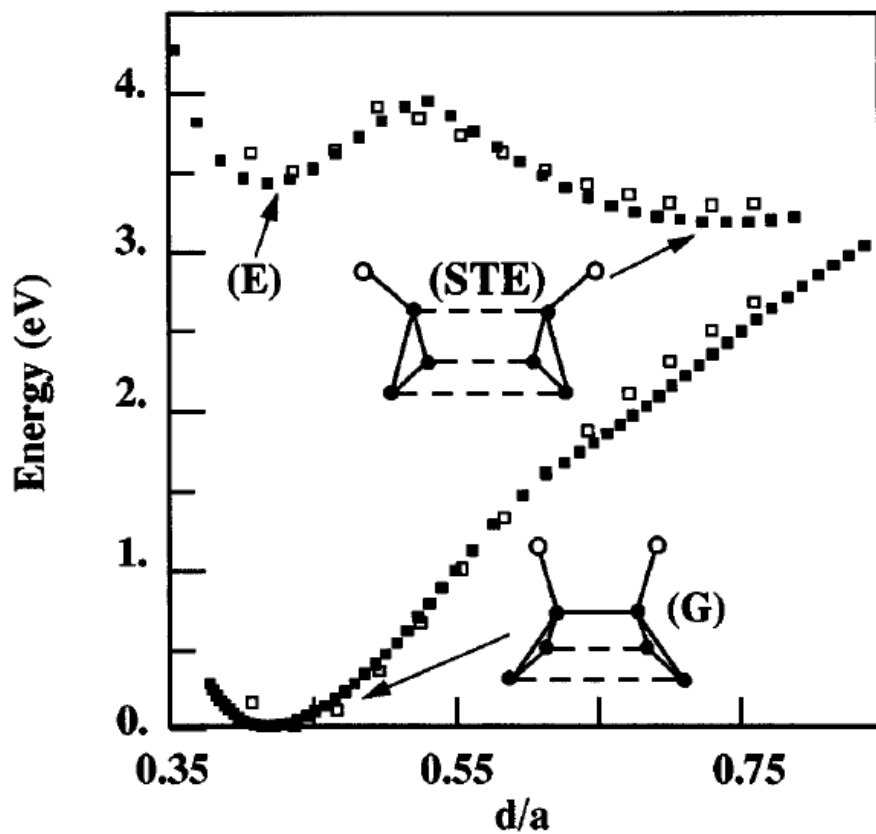
Figure 4.4: Dimer mechanism in $Si_{29}H_{34}$ from ref [2]. The ground state and excited state are calculated using LDA (■) and tight binding (□), as a function of dimer bond length d ($a = 5.4$ Å). The inset images show a schematic view of the surface in the ground state (G), and self trapped exciton state (STE) with ○ = hydrogen, ● = silicon.
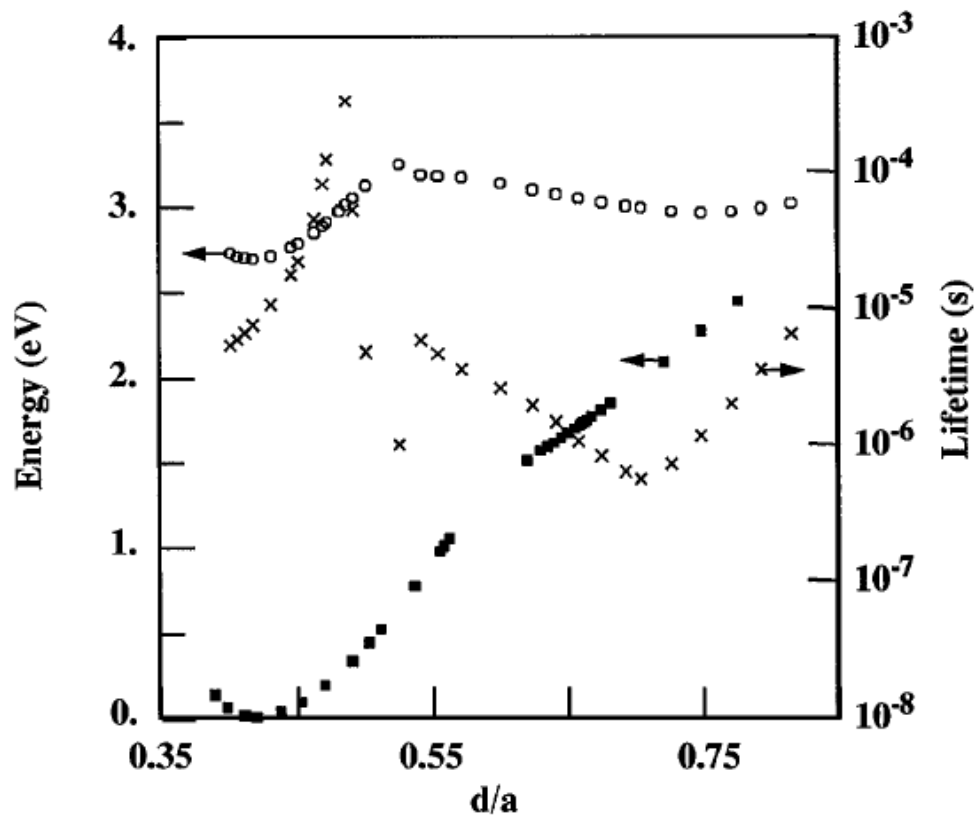
Figure 4.5: Dimer mechanism in 123 Si atom nanocrystal from ref [2]. Tight binding energies of the ground state (■) and excited state (○) are shown, with the calculated radiative lifetime (×).

well. Therefore a vertical excitation will bring the nuclear wave-function into a superposition of several double well states to start localized in the inner well. If these superpositions remain coherent, the 'tunnelling' due to the vibrational modes causing an oscillation between the wells is quite long from milliseconds to seconds for the first few levels. Nayfeh et al. argue that it is unlikely for coherence to remain in experimental conditions, and estimate thermalization between vibrational levels will bring the population the bottom of the outer well on a time scale of picoseconds [95].

For the larger 123 silicon atom particle, the outer-well is of higher energy. This allows vibrational states to be constrained to the inner well. Therefore this mechanism becomes truly efficient only for particles with the outer-well lower than the inner well, which is estimated to occur in particles below 70 silicon atoms corresponding to a diameter of about 1.4 nm [95].

4.3 Density functional theory (DFT)

Electrons are fermions which requires their description in a wavefunction to be antisymmetric to exchange of any two electrons. The wavefunction description of the many-body problem with N electrons depends on $3N$ spatial coordinates, and quickly becomes intractable. Since the electrons are indistinguishable from each other, it may appear that we shouldn't be labelling them in the first place and then requiring a symmetry under exchange of these labels. Density functional theory is based on the surprising result that, in principle, it is possible to calculate the properties of a multi-electron system as just a functional of the ground state density $n(\vec{r})$. Since the density is related to the normalized wavefunction Ψ by

$$n(\vec{r}) = N \int \mathrm{d}^3 r_2 \int \mathrm{d}^3 r_3 \cdots \int \mathrm{d}^3 r_N \Psi^*(\vec{r}, \vec{r}_2, \ldots, \vec{r}_N) \Psi(\vec{r}, \vec{r}_2, \ldots, \vec{r}_N) \quad (4.1)$$

density functional theory means that in some sense the wavefunction has so much redundant information, that integrating over all but one coordinate does not actually reduce the amount of information we have about the ground state. Instead of dealing with a function of $3N$ coordinates, it is ideally possible to deal with just one function of 3 coordinates.

Density functional theory was proposed in 1927 by Thomas [96] and Fermi [97], which gave the kinetic energy as a local functional of the density by as-

signing a kinetic energy density at each point equal to that of a homogeneous electron gas of the same density. The potential energy was then given in terms of the classical electrostatic interaction. This was extended by Dirac [98] to include a local approximation for the exchange energy in an electron gas. In atomic units the resulting Thomas-Fermi-Dirac functional is [99]

$$
E_{TFD}[n] = \int d^3r \ V_{ext}(\mathbf{r})n(\mathbf{r}) + \frac{1}{2} \int d^3r \ d^3r' \ \frac{n(\mathbf{r})n(\mathbf{r}')}{|\mathbf{r} - \mathbf{r}'|}
$$
$$
+ \frac{3}{10}(3\pi)^{2/3} \int d^3r \ n(\mathbf{r})^{5/3} - \frac{3}{4}\left(\frac{3}{\pi}\right)^{1/3} \int d^3r \ n(\mathbf{r})^{4/3}
$$
(4.2)

where V_{ext} is the external potential, usually taken to be the electric potential from a static set of nuclei. The first two terms are the classical external potential energy and the inter-electron electrostatic energy respectively. The third term is the local approximation to the kinetic energy, and the final term is the local exchange.

These original attempts at calculating the energy with the density were approximations with no strong theoretical backing, and missed some of the physics such as correlation energy. Density functional theory was put on a solid foundation in 1964 when Hohenberg and Kohn proved two important theorems [100]. First, that given the unique (ie. a non-degenerate system) ground state density $n_0(r)$ of a Hamiltonian with the form

$$
\hat{H} = -\frac{\hbar^2}{2m_e}\sum_i \nabla_i^2 + \sum_i V_{ext}(\mathbf{r}_i) + \frac{1}{2}\sum_{i \neq j} \frac{e^2}{|\mathbf{r}_i - \mathbf{r}_j|}
$$
(4.3)

that the external potential $V_{ext}(r)$ is determined uniquely up to a constant. Schematically this can be represented as

$$
\begin{array}{ccc}
V_{ext}(\mathbf{r}) & \stackrel{HK}{\Longleftarrow} & n_0(\mathbf{r}) \\
\Downarrow & & \Uparrow \\
\Psi_i(\{\mathbf{r}\}) & \Longrightarrow & \Psi_0(\{\mathbf{r}\})
\end{array}
$$

Starting with the external potential V_{ext} it is possible, in principle, to solve for all the eigen functions and their energies. With the eigen functions and energies, it is trivial to select the ground state as the one with the lowest energy. And with the ground state wavefunction it is likewise trivial to calculate the ground state density. What Hohenberg-Kohn proof added is

from the ground state density, the external potential is uniquely determined. This amazing fact closes the circle, allowing in principle all properties of the system to be determined just from the ground state density.

Second, Hohenberg-Kohn proved that there exists a *universal* functional for the energy $E[n]$ in terms of the density. By universal it is meant that all terms are independent of the external potential, except for one explicit term $\int d^3r \ V_{ext}(r)n(r)$ just like in Thomas-Fermi, and the functional $E[n]$ is valid for any external potential. For a given potential, the density which minimizes the functional is the ground state density, and the global minimum value of this functional is the ground state energy.

When solving the many body-problem for electrons in a material, the external potential is the Coulomb potential from the nuclei. The decoupling of the nuclei and electronic wavefunction by the Born-Oppenheimer, is what allows considering the nuclei as 'external'. More simply the nuclei are usually treated as classical fixed point charges defining a potential for the electrons. If necessary, the energy of the system at different nuclear positions can be used to define a potential energy surface for the nuclei.

The functional for a system of electrons and fixed nuclei is

$$E_{\text{HK}}[n] = F_{\text{HK}}[n] + \int d^3r \ V_{\text{ext}}(\mathbf{r})n(\mathbf{r}) + E_{\text{II}} \qquad (4.4)$$

where the term E_{II} is the classical interaction energy of the nuclear point charges, and V_{ext} is the coulomb potential from the nuclear as well as any externally applied potential to the system. The Hohenberg-Kohn functional $F_{\text{HK}}[n]$ accounts for all internal, kinetic, and potential energies of the interacting electron system. It can be further split into kinetic energy and interaction energy functionals

$$F_{\text{HK}}[n] = T[n] + E_{\text{int}}[n]. \qquad (4.5)$$

The proofs presented by Hohenberg-Kohn show that this functional is universal, in that it applies to any multi-electron system regardless of the number of electrons or the external potential. In this sense, density functional theory is just as 'fundamental' as the wavefunction approach. Unfortunately however, their proof is an existence proof and not a constructive proof. So the exact functional is not known. However, as in the case of Thomas-Fermi

density functional theory, approximations to the functional can be made.

The Hohenberg-Kohn proofs have since been extended to include degenerate systems, and even potentials where a time dependence is turned on. It can also be extended to include different types of particles by including multiple densities. Of particular interest is a systems with unpaired electrons ('open shell' in molecular orbitals terms). The functional can be written in terms of both a total electron density

$$n(\mathbf{r}) = n_\uparrow(\mathbf{r}) + n_\downarrow(\mathbf{r}) \tag{4.6}$$

and a spin density

$$s(\mathbf{r}) = n_\uparrow(\mathbf{r}) - n_\downarrow(\mathbf{r}). \tag{4.7}$$

The 'spin density functional' $E[n, s]$ can be used to describe spin polarized molecules, and solids with magnetic order [101]. As this is a relatively straight-forward extension, these methods are still referred to as DFT. Note however that for external coupling beyond a scalar potential, such as vector potential coupling like magnetic field interactions with orbital angular momentum, extensions to 'current density functional' theory are required [102].

Density functional theory is currently one of the most widely used approach for electronic structure calculations, due to the simplifying method proposed by Kohn and Sham in 1965. What they proposed was an ansatz which in principle allows exact calculations of interacting many body systems by relating it to a system of non-interacting particles. In practice this method has led to functional approximations which have shown to be successful in modelling multi-electron system properties.

The Kohn-Sham ansatz relies on two assumptions [103, 99].

1. There exists an 'auxiliary' system of non-interacting particles in which the ground state has the same density as the ground state for the interacting system. The class of problems which have such an auxiliary system is called "non-interacting-V-representability".

2. The Hamiltonian for the auxiliary system has the usual kinetic energy operator and an effective potential V_{eff}^σ acting on electrons of spin σ. While not required, this potential is taken to be local.

While there is no rigorous proof that any useful real systems are in the class of "non-interacting-V-representability", as this is an ansatz the usefulness of this approach is demonstrated by the resulting ability to model systems.

The Hamiltonian of the auxiliary non-interacting system is (in atomic units)

$$\hat{H}^{\sigma}_{\text{aux}} = -\frac{1}{2}\nabla^2 + V^{\sigma}_{\text{eff}}(\mathbf{r}). \tag{4.8}$$

Without specifying details of the potential yet, it is clear that given a potential it is in principle possible to solve for the the eigen functions and values. Since these orbitals are non-interacting, now a slater determinant is actually an exact solution of this. In terms of the occupied orbitals, the density and kinetic energy of this system is

$$n(\mathbf{r}) = \sum_{\sigma}\sum_{i=1}^{N_{\sigma}}|\phi_i^{\sigma}(\mathbf{r})|^2 \tag{4.9}$$

$$T_s = -\frac{1}{2}\sum_{\sigma}\sum_{i=1}^{N_{\sigma}}\langle\phi_i^{\sigma}|\nabla^2|\phi_i^{\sigma}\rangle = \frac{1}{2}\sum_{\sigma}\sum_{i=1}^{N_{\sigma}}\int d^3r\,|\nabla\phi_i^{\sigma}(\mathbf{r})|^2. \tag{4.10}$$

From Hohenberg-Kohn, there is a universal functional for kinetic energy, so the kinetic energy of the auxiliary system can also be written as $T_s[n]$ a functional of the density.

There is only one energy functional for the interacting system, as shown by Hohenberg-Kohn, so the Kohn-Sham method is to rewrite the functional as

$$E_{\text{KS}}[n] = T_s[n] + \int d^3r\, V_{ext}(\mathbf{r})n(\mathbf{r}) + E_{\text{Hartree}}[n] + E_{\text{II}} + E_{\text{xc}}[n] \tag{4.11}$$

where the Hartee energy is just the classical Coulomb interaction energy of an electron density n

$$E_{\text{Hartree}}[n] = \frac{1}{2}\int d^3r d^3r'\frac{n(\mathbf{r})n(\mathbf{r}')}{|\mathbf{r} - \mathbf{r}|} \tag{4.12}$$

and the exchange-correlation energy E_{xc} is *defined* to make the functional match Hohenberg-Kohn. This gives the exchange-correlation functional as

$$E_{\text{xc}}[n] = (T[n] - T_s[n]) + (E_{\text{int}}[n] - E_{\text{Hartree}}[n]). \tag{4.13}$$

Written this way the advantage of the Kohn-Sham method is much more clear. By explicitly taking the difference of the kinetic energy for the interacting and non-interacting case, as well as the difference in the long range interaction terms, the resulting exchange-correlation functional should be a nearly local functional and be much more amenable to approximation.

In practice, instead of varying the density directly to find the ground state energy, it is computationally more straightforward to use a basis set and solve for the eigen functions (the orbitals) of the non-interacting auxiliary system. The ground state density of the auxiliary system is then, by design of the Kohn-Sham ansatz, the same as the density for the interacting system. So the total energy in the interacting system can be calculated with the density.

Requiring the variation of the Kohn-Sham energy functional (eq. 4.11) with respect to changes in the orbitals while maintaining the orthogonalization constraint between the orbitals, results in eigen value equation [99]

$$(H_{\text{KS}}^{\sigma} - \epsilon_i^{\sigma})\phi_i^{\sigma} = 0 \tag{4.14}$$

with

$$H_{\text{KS}}^{\sigma} = \sigma_{\text{aux}} = -\frac{1}{2}\nabla^2 + V_{\text{eff}}^{\sigma}(\mathbf{r}) \tag{4.15}$$

$$\begin{aligned} V_{\text{eff}}^{\sigma}(\mathbf{r}) &= V_{\text{ext}}(\mathbf{r}) + \frac{\delta E_{\text{Hartree}}}{\delta n(\mathbf{r}, \sigma)} + \frac{\delta E_{xc}}{\delta n(\mathbf{r}, \sigma)} \\ &= V_{\text{ext}}(\mathbf{r}) + V_{\text{Hartree}}(\mathbf{r}) + V_{xc}(\mathbf{r}) \end{aligned} \tag{4.16}$$

While the particles are formally non-interacting, the V_{eff} depends on the orbitals. So we don't know V_{eff} to allow direct solving of the eigen value problem. As in the Hartree-Fock case, through iteration this is solved self consistently. It should be stressed that the resulting ground state wavefunction in the auxiliary basis is *not* equal to the wavefunction in the real life interacting case. This method gives the total energy and density of the ground state, but not the wavefunction.

The only piece remaining is to approximate the exchange-correlation functional. There are currently a multitude of functionals with different approximations to choose from. The first widely used functional was the local density approximation (LDA). The exchange and correlation were given locally as the same value in a homogeneous gas. The exchange is given by the same result Dirac calculated and added to the pre-Kohn-Sham attempts

at density function theory by Thomas and Fermi (eq. 4.2). The correlation energy came from quantum Monte Carlo calculations by Ceperley and Alder in 1980 which provided essentially exact results for a homogeneous electron gas [104]. This was then fit to analytical functions resulting in two widely used correlation functionals due to Perdew and Zunger (PZ) [105] and Vosko, Wilkes, and Nusair (VWN) [106].

Improvements beyond LDA include generalized gradient approximations (GGA) which provide corrections to the exchange-correlation functionals based on the local gradient of the density. Exchange energy is often treated with a GGA introduced in 1998 by Becke (B88) [107]. For correlation energy, a commonly used GGA is the Lee-Yang-Parr (LYP) functional [108].

Among the most accurate functionals for calculating the energy of structures are hybrid functionals. Because the orbitals are already calculated in the Kohm-Sham approach, it is possible to use these directly in a combination of an orbital dependent functional and a pure density functional. The functional used in this work is the 3 parameter Becke hydrid functional B3LYP, which consists of an exchange functional built from 0.8 LDA+0.72 B88+0.2 Hartree-Fock and a correlation functional built from 0.19 LDA(VWN) + 0.81 LYP.

Excited state properties such as energies, oscillator strengths, and nuclear gradients can be calculated by looking at the response of the system to a time dependent perturbation. Runge and Gross proved the extension to time dependent density functional theory (TDDFT) in principle allows response properties to be calculated without approximation in finite systems [109]. The properties can be calculated by starting with a ground state and solving the Kohn-Sham equations in time steps allowing the density to evolve. Taking the Fourier transform of this explicit time response can give the resonant modes (excited states) and their oscillator strengths [99].

Another means to obtain excited state properties is to look at only the linear response to a perturbation

$$\chi(\mathbf{r}, \mathbf{r}') = \frac{\delta n(\mathbf{r})}{\delta V_{\text{ext}}(\mathbf{r}')}. \tag{4.17}$$

This can be rewritten as

$$\chi = \frac{\delta n}{\delta V_{\text{eff}}} \frac{\delta V_{\text{eff}}}{\delta V_{\text{ext}}} = \frac{\delta n}{\delta V_{\text{eff}}} \left[\frac{\delta V_{\text{ext}}}{\delta V_{\text{ext}}} + \frac{\delta V_{\text{int}}}{\delta V_{\text{ext}}} \right] = \frac{\delta n}{\delta V_{\text{eff}}} \left[1 + \frac{\delta V_{\text{int}}}{\delta n} \chi \right]. \tag{4.18}$$

Noting the response of the non-interacting system is just

$$\chi^0 = \frac{\delta n}{\delta V_{\text{eff}}} \tag{4.19}$$

solving for the linear response gives

$$\chi = \frac{\chi^0}{1 - \chi^0 K}, \quad \text{where } K = \frac{\delta V_{\text{int}}}{\delta n}. \tag{4.20}$$

It is clear from this form that there can be poles in the response.

These poles in the linear response denote an excitation energy. So by expanding in terms of the orbitals the condition for a pole in the linear response to a frequency perturbation, will allow solving for the excitation energies and excitation 'vectors' without explicitly solving for the time dependence. The excitation vectors provide information on the combination of empty (also called virtual) and occupied orbitals which are having their populations oscillated at the pole. This resulting equation for the orbitals, is an eigen value equation for the excitation vectors [110]

$$(\Lambda - \Omega_n \Delta)|X_n, Y_n\rangle = 0 \tag{4.21}$$

where Ω_n is the excitation energy, $|X_n, Y_n\rangle$ is the excitation vector in the linear space $L = L_{\text{virt}} \times L_{\text{occ}} \oplus L_{\text{occ}} \times L_{\text{virt}}$, and

$$\Lambda = \begin{bmatrix} A & B \\ B & A \end{bmatrix}, \Delta = \begin{bmatrix} 1 & 0 \\ 0 & 1 \end{bmatrix}. \tag{4.22}$$

The tensors A and B called the "orbital rotation Hessians", which can be written in terms of the orbitals and given in explicit form in ref [110]. Operators acting on the excitation vector can give the transition dipole moment (and thus the oscillator strength), magnetic transition moment, and other properties.

Of particular importance here is that this method of finding excitation properties without explicitly solving the time dependence also allows the calculation of nuclear gradients to the excited state energy [111]. The excited state properties calculated in this manner have been found to be of better quality than calculations by configuration interaction singles (CIS) and time dependent Hartree-Fock (TDHF) methods.

4.4 Dimer calculations for $Si_{29}H_{24}$, $Si_{29}H_{26}$, $Si_{29}H_{34}$

The calculations of Delerue et al. [2, 1] of a 1 nm silicon particle with a single dimer used local density approximation (LDA) density functional theory (DFT) and an empirical tight-binding method. Here we investigate the dimer mechanism further by using a hybrid functional to provide improved calculations of the 1 dimer $Si_{29}H_{34}$ structure. We will also explore how the dimer mechanism works with structures containing multiple dimers. Of particular interest is the 6 dimer $Si_{29}H_{24}$ structure, which has been shown to be the most likely structure of the 1 nm particles from comparisons to calculated absorption and Raman scattering. Finally a particle with five dimers, $Si_{29}H_{26}$, is considered to give information on the trend as dimers are added.

The equilibrium ground state geometries for all structures were obtained using DFT with the B3LYP hybrid functional using the quantum chemistry computational package GAMESS (General Atomic and Molecular Electronic Structure System) [63, 64, 65] using the 6-311G(d,p) basis set. Given any position for the nuclei, even if not at the minimum of the ground state potential energy surface, time dependent density functional theory (TDDFT) can be used to obtain excited state energies and oscillator strengths. A series of calculations at different nuclear coordinates can therefore provide the excited state potential energy surface along a slice.

The radiative lifetime τ, the transition matrix element, and the Einstein coefficient A_{21} for spontaneous decay from the excited state 2 to state 1, can be obtained from the oscillator strength f_{osc} using the relations

$$f_{\mathrm{osc}} = \frac{2m\omega_{12}}{\hbar} \left| \langle \psi_2 | \vec{r} | \psi_1 \rangle \right|^2 \tag{4.23}$$

$$1/\tau = A_{21} = \frac{2e^2\omega_{12}^3}{3\epsilon_0 h c^3} \left| \langle \psi_2 | \vec{r} | \psi_1 \rangle \right|^2$$

$$\tau \approx 29.7 \text{ picosecond } \left(\frac{\mathrm{Hartree}}{\hbar\omega_{12}} \right)^2 \frac{1}{f_{\mathrm{osc}}} \tag{4.24}$$

The oscillator strengths obtained from TDDFT therefore allow mapping the radiative rate at each point on the excited state potential energy surface, to determine which regions emission are most likely to occur from.

At the time these calculations were performed GAMESS did not have

the capability to provide nuclear gradients for excited states, so it was not possible to relax structures in the excited state. DFT calculations were also limited to densities represented by closed shell slater determinants (RHF), or high spin opens shells using the slater determinants of restricted open shell Hartree-Fock (ROHF, which requires double occupied orbitals to use the same spatial function for both the spin up and spin down electron) and unrestricted Hartree-Fock (UHF, where the spatial orbitals can differ based on spin). This prevented the possibility of doing a ground state calculation with a singlet state in a different irreducible representation to take advantage of the symmetry of the molecules to obtain information about the excited state surface without using TDDFT. As the dimension of the excited state potential energy surface is 3N where N is the number of nuclei, the nuclear position freedom is prohibitively large to scan the surface with many single point calculations. A careful choice of a 'reaction path' to measure the excited state energies is required.

Constrained optimizations in the ground state were used to construct a reaction path. One dimer would be chosen in the structure, and stretched to a set value while allowing the rest of the nuclear coordinates to relax. This was repeated at multiple dimer lengths and the coordinates of the resulting structures were used as the reaction path to investigate a slice of the excited state energy surface. For all three molecules considered, the coordinates maintained C_{2v} point group symmetry along this path.

The lowest excitation of the single dimer $Si_{29}H_{34}$ structure along this reaction path displayed the characteristic double well of the dimer model (Figure 4.6). The excited state has a B_2 irreducible representation, which is antisymmetric to inversion across the plane perpendicular to the dimer. This is the correct representation if the excited electron is in an orbital of σ^* anti-bonding nature for the dimer bond. The bad gap of 4.4 eV obtained with B3LYP is significantly larger than the 3.5 eV band gap obtained by Allan et. al using LDA [2]. For comparison a B3LYP-TDDFT calculation was done on the bulk configuration $Si_{29}H_{36}$ structure with no dimers, which yielded a band gap of 4.5 eV. Therefore at this level of theory, the band gap is only reduced slightly by a single dimer.

Possibly due to the increased band gap according to B3LYP versus LDA, the peak barrier in the single dimer structure is found to be much smaller, only 0.17 eV as opposed to 0.5 eV with LDA. Additionally, the outer-well
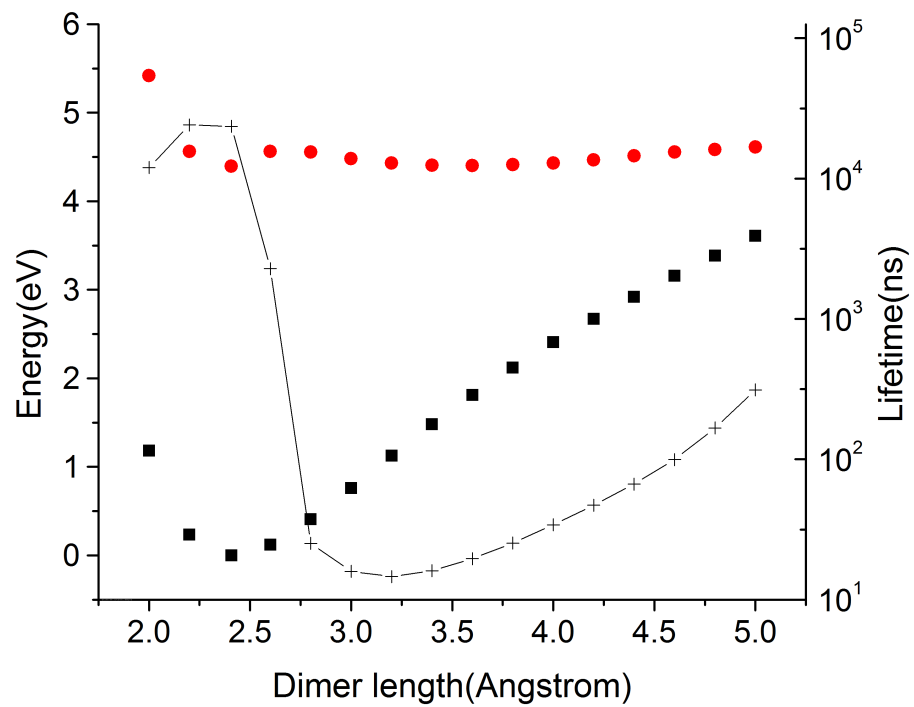
Figure 4.6: Radiative lifetime (+) of the lowest excited state as the dimer is stretched for $Si_{29}H_{34}$ (only has 1 dimer). The ground state (■) and excited state (•) energies relative to the ground state minimum are shown for reference.

minimum shifted outwards to ~ 3.6 Å whereas LDA calculations indicated 3.24Å . A drastic decrease in radiative lifetime from about 25 microseconds to about 15 nanoseconds is seen as the barrier is reached and crossed, validating the expectations of the dimer model.

The $Si_{29}H_{24}$ structure with a fully reconstructed surface (6 dimers, and no remaining di-hydride terminations), has T_d point group symmetry. In addition to simplifying the calculations, this high symmetry makes many of the electronic states degenerate, therefore allowing calculation of much higher energy states. The first 28 excited states, with their energies, irreducible representation and oscillator strengths are listed in Table 4.1. There is a band of states from 3.3-3.6 eV and then a gap until 4.0 eV.

When the structure is broken to C_{2v} symmetry by stretching the dimer, the B_2 states will arise from T_d representations splitting into C_{2v} representations as follows: $T_1 \rightarrow A_2 + B_1 + B_2$ and $T_2 \rightarrow A_1 + B_1 + B_2$. As seen from Table 4.1, the lowest state is no longer a B_2 representation. Only T_2 representations are dipole allowed, so the lowest B_2 excited state, which originates from T_1, is not even dipole allowed.

To identify which states participate in the dimer mechanism in this 6 dimer structure, the lowest two states of each C_{2v} representation were calculated at several dimer lengths. Again it is the B_2 state which plays a primary role, indicating the simple picture of a σ bonding and σ^* anti-bonding orbitals for a single dimer may still hold even though there are several dimers on the surface. The B_2 state crosses the other states to becomes the lowest excited state along the majority of this reaction coordinate. This occurs both when expanding or contracting the dimer length. When the dimer length is stretched even longer, the B_2 state separates in energy forming a gap from the other states which remain closely spaced (Figure 4.7). The outer well now goes lower than the inner well.

With the active state verified, more points along the dimer stretch coordinate path are calculated. The resulting slice of the potential energy surface, and radiative lifetimes are presented in Figure 4.8. Because the lowest B_2 state is dipole forbidden right at the ground state equilibrium, the first B_2 dipole allowed state is used at that point. This gives a better indication of the oscillator strength trends, and as seen in Figure 4.7 the two states have very similar energies with a separation of only 9 meV. At this small separation, it is possible the energy level ordering is incorrect.

Symmetry	eV	nm	Oscillator strength
A_2	3.3034	375.32	0
T_1	3.3178	373.69	0
E	3.3188	373.58	0
T_2	3.3262	372.75	0.0000442
T_1	3.4757	356.72	0
T_2	3.5458	349.66	0.0002496
T_1	3.5557	348.7	0
T_2	3.5765	346.66	0.0016496
E	3.5996	344.44	0
A_1	3.6267	341.87	0
T_1	3.9524	313.69	0
T_1	4.0645	305.04	0
A_2	4.1197	300.96	0
T_1	4.1388	299.57	0
E	4.1686	297.43	0
T_2	4.1687	297.41	0.0009384
T_2	4.196	295.48	0.0095007
E	4.2159	294.09	0
T_1	4.2164	294.05	0
T_2	4.2318	292.98	0.0011087
T_2	4.2606	291	0.0017732
T_1	4.2866	289.23	0
A_1	4.3285	286.44	0
E	4.3318	286.22	0
T_1	4.3387	285.77	0
T_2	4.3401	285.67	0.0144434
T_2	4.3802	283.06	0.0005031
T_1	4.3906	282.38	0

Table 4.1: B3LYP TDDFT results for excited states of $Si_{29}H_{24}$ in the ground state equilibrium geometry. Irreducible representation in T_d point group symmetry is given, along with energy in electron volts (eV) and corresponding photon wavelength (nm).
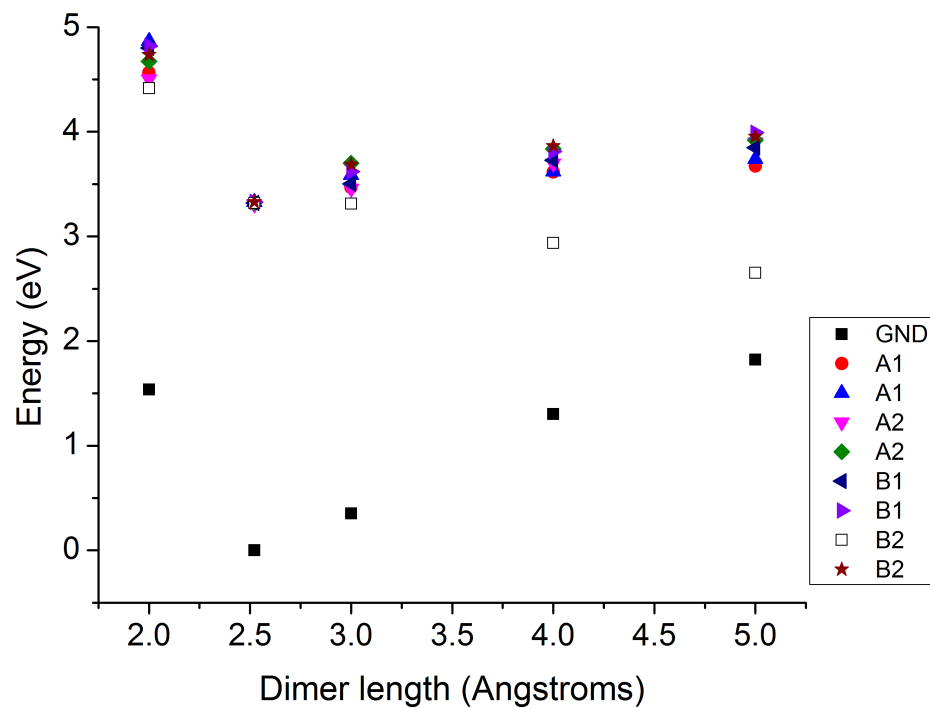
Figure 4.7: The lowest two excited levels of each irreducible representation of C_{2v} point group, at different dimer lengths. As the dimer stretches one B_2 state lowers in energy, separating from the other excited states which raise in energy and remain closely spaced.

Figure 4.8: Radiative lifetime (+) of the lowest excited state of B_2 irreducible representation as one dimer is stretched for $Si_{29}H_{24}$ (has 6 dimers total). The ground state (■) and excited state (●) energies relative to the ground state minimum are shown for reference. At the ground state minimum this structure has higher symmetry (T_d point group symmetry), and the lowest B_2 excited state is actually dipole forbidden. At that one point the second B_2 excited state is used instead (whose energy almost coincides with the lowest energy state at this scale).
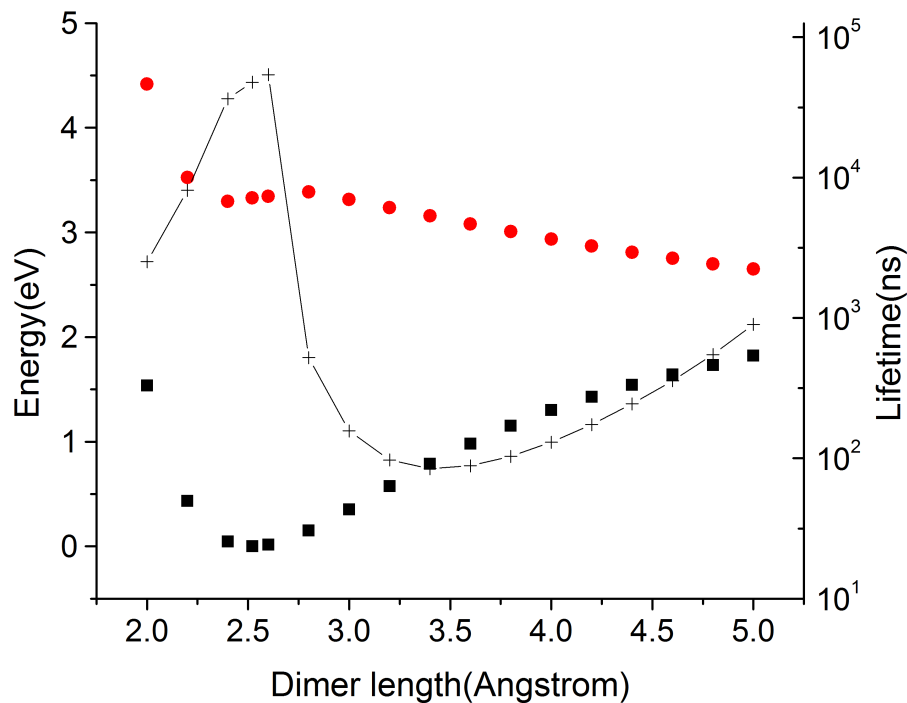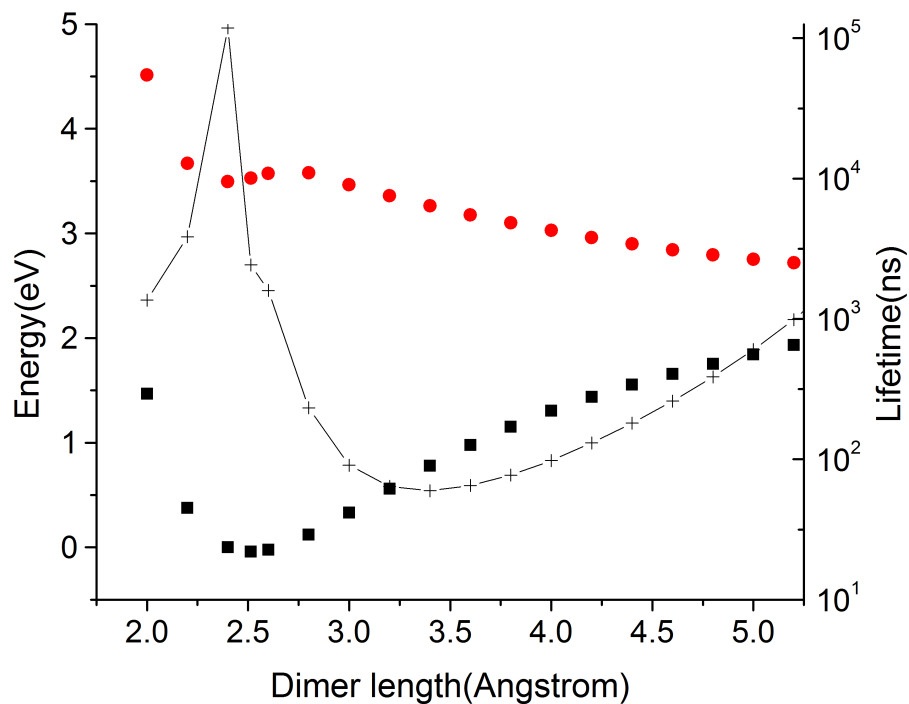
Figure 4.9: Radiative lifetime ($+$) of the lowest excited state of B_2 irreducible representation as one dimer is stretched for $Si_{29}H_{26}$ (has 5 dimers total). The ground state ($\blacksquare$) and excited state ($\bullet$) energies relative to the ground state minimum are shown for reference.

As in the single dimer case, there is a drastic decrease in the radiative lifetime as the dimer length approaches and crosses the barrier. Before the barrier the maximum lifetime is about 55 microseconds and after the barrier reaches a minimum of about 100 nanoseconds. The inner well minimum corresponds with the ground state minimum, and the barrier is now decreased to about 60 meV. While the outer well now goes significantly below the inner well minimum, it no longer appears to have a local minimum.

Attempts to go to longer dimer distances resulted in the hydrogens on the dimer atoms to move to the inside of the dimer, and a smooth transition was not found. Increasing the length further led to the triplet state running into the singlet ground state, making it an unstable reference for TDDFT. This could be interpreted as escape to the outer well resulting in a non-radiative process of returning to the ground state. However this could be an artifact of how the reaction coordinate path was obtained, and may not be appropriate at these longer lengths. A further study using relaxation in the excited state will be needed to conclude where, or if, a local minimum in the outer well occurs.

As an intermediary case, the five dimer $Si_{29}H_{26}$ structure was also studied. The band gap is found to be 3.5 eV. Like the 6 dimer case, it also didn't have a B_2 state as the lowest energy state at the ground state equilibrium. Moving along the reaction coordinate the B_2 state again crosses the others and forms a substantial gap as the dimer length is increased. The barrier is only about 85 meV, larger than the 6 dimer case but still much below the single dimer case. Again the double well structure doesn't appear to have an outer minimum (Figure 4.9). In agreement with the other structures with a surface reconstruction dimer, the radiative lifetime decreases several orders of magnitude as the barrier is approached.

The dimer model appears quite robust showing a double well structure and decrease in radiative life time with all the structures studied. The band gap is found to decrease with an increasing number of dimers, while the barrier height decreases. These calculations estimate a lifetime on the order of 100 ns for states near the barrier. As the sharp increase in oscillator strength occurred near the barrier top, it is possible that crossing over the barrier to achieve strong fluorescence in not fully necessary and merely being in a state that reaches near the barrier may be enough. Either way, the B3LYP-TDDFT calculations show that the barrier height is much more accessible

than the 0.5 eV barrier calculated using LDA.

4.5 Vibrational structure in low temperature photoluminescence

At low temperatures the measurement of the fluorescence can reveal a structure in the spectrum due to vibrational coupling with the excited state. Satish Rao obtained fluorescence measurements of 1 nm silicon particles at 120 K that had resolvable peaks on the usually broad emission spectra [23]. The background subtracted resolved peaks are shown in Figure 4.10.

The results show at least three groupings of peaks with an even spacing. One group has a spacing of 40 meV, while the other two groups have a spacing of 33 meV. These repeated spacings correspond to the energy of a vibrational mode which is coupled to the emission process in some manner.

Of the normal modes previously calculated, there is a mode at 320 cm^{-1} which corresponds to 40 meV. This mode is triply degenerate, and is of T_2 irreducible representation. Each of these degenerate modes involves a different pair of surface dimers. The pair of dimers are opposite of each other on the particle, and are involved in an anti-symmetric stetching motion. When one dimer expands the other contracts and vice versa. The remaining four dimers just rock back and forth during this motion, and the other silicon atoms are relatively stationary. The vibrational mode is illustrated in Figure 4.11 in a series of snapshots of the nuclei displaced (exaggeratedly) along the normal mode.

There is also a mode at 282 cm^{-1} (35 meV) which involves an anti-symmetric dimer stretch and is within the calculation accuracy of the 33 meV experimental value. This mode is also triply degenerate and of T_2 irreducible representation. Each mode is again an opposite dimer pair stretching anti-symmetrically, but now it is the four silicon atoms attached to each of those dimers that moves in tandem. When a dimer contracts, its four adjacent silicon atoms 'pinch' in simultaneously with it.

The anti-symmetric dimer modes fit well with the proposed dimer role in fluorescence. The dimers are each under 'stress' in the sense that if a dimer bond was removed the other dimers would relax to a shorter length. As an example, in the $Si_{29}H_{26}$ structure studied earlier, the dimers are all shorter in

74

length than in $Si_{29}H_{24}$. Therefore an anti-symmetric dimer stretching mode probably corresponds with the initial direction of the coordinate path leading over the minimum barrier to the outer well.
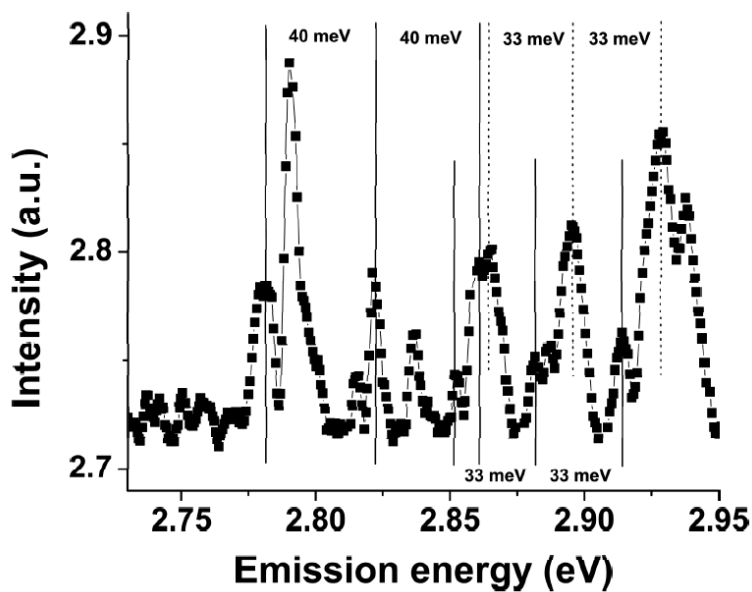
Figure 4.10: Vibronic structure in low temperature photoluminescence of 1 nm silicon nanoparticles, from ref [23].
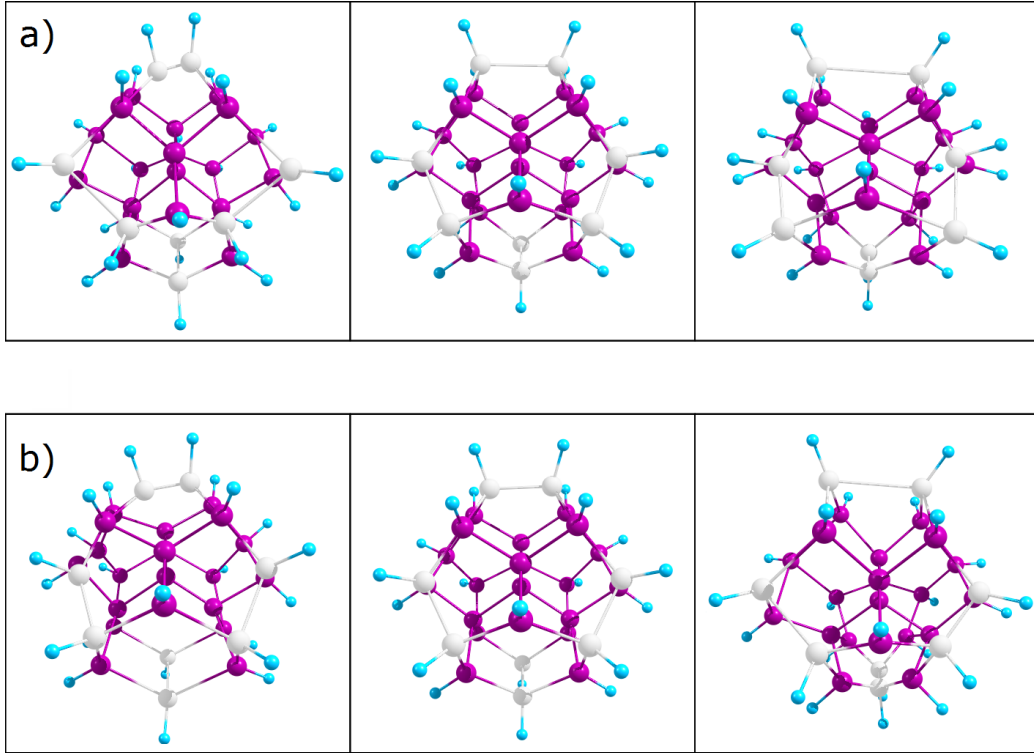
Figure 4.11: Vibrational modes which primarily involve dimer stretching. Snapshots of the particle undergoing exaggerating motion along a vibrational mode are shown to illustrate the movement. The Si atoms of 4 of the dimers are highlighted. In both vibrations the top dimer stretches while the bottom contracts and vice versa in an anti-symmetric stretch. a) Dimer stretch and rocking, 320 cm^{-1} = 40 meV. Two dimers stretch while the others rock back and forth. b) Dimer stretch and pinch, 282 cm^{-1} = 35 meV. Due to orientation the 'pinch' can best be seen on the bottom dimer. When the bottom dimer expands, the four silicon atoms attached to it expand out, when it contracts they pinch in.

4.6 Excited state potential energy surface

The calculation of the double well in the excited state energy in the previous section 4.4 used structures optimized in the ground state. Relaxation of the nuclear coordinates to minimize the energy in the excited state gives paths on the excited state potential energy surface which are more relevant to emission, as this relaxation contributes to the Stokes shift. This also allows answering the question of the existence and stability of the outer well minimum which could not be determined with relaxation in the ground state. Additionally, knowledge of how much the barrier between the two wells can be reduced by relaxation in the excited state determines if direct excitation over the barrier is energetically allowed.

Calculation of the excited state potential energy surface of $Si_{29}H_{24}$ was done at the TD-DFT level using the B3LYP functional with the TURBO-MOLE quantum computational package [112]. The TZVP basis was used which is a triple split valence basis with polarization functions added for each atom [113, 114, 115]. The excited state energy gradients with respect to the nuclear positions are available, allowing excited state geometry relaxation.

The minimum ground state energy structure was found with this new codebase and atomic orbital basis. The excitation energies are slightly lower compared to the GAMESS 6-311G(d,p) calculation, with the lowest dipole allowed state (T_2 representation) 3.29 eV above the ground state. However the representations of the energy levels are in the same order at least up to the the 3.6 eV state, which is the last level below the 'gap' to the next band of energy levels.

To improve on the previously shown $Si_{29}H_{24}$ double well curve, the path on the excited state surface was chosen now by minimizing the energy of the first excited state geometry with one dimer constrained to a given length. This should be a more representative slice of the potential energy surface since the geometries are relaxed in the excited state instead of the previous path which was obtained by relaxing in the ground state. To allow a more direct comparison with the previous calculation, the structure was also constrained to C_{2v} symmetry.

The comparison of the energies for the ground state optimized and excited state optimized structures are shown in Figure 4.12. All energies are relative to the minimum ground state energy, therefore allowing easy comparison and calculation of the Stokes shift. Absorption is a vertical excitation process from the ground state energy minimum to the excited state of that same geometry. The structure can then change to one of lower energy in the excited state, where emission occurs to the ground state of this new structure. The relaxation decreased the inner well excited state 0.28 eV, and also increased the ground state 0.30 eV for an overall ~ 0.6 eV Stokes shift for emission from the inner well. In the entire inner well and at the barrier the energy difference between the excited state and ground state remains close to 2.7 eV. Emission at the barrier would be 2.73 eV (455 nm).

The barrier height between the inner and outer well is now 3.25 eV (rel-
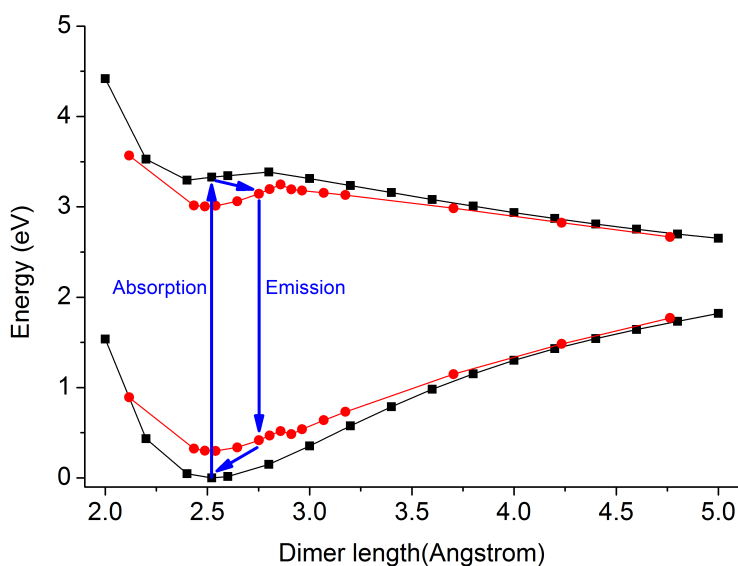
Figure 4.12: The ground and excited state energies calculated with structures relaxed in the ground state (■), compared to the ground and excited state energies with structures relaxed in the excited state (●). All energies are relative to the ground state minimum. The structures were calculated with one dimer constrained to a given length and the structure having C_{2v} symmetry. Absorption (excitation) proceeds vertically from the ground state minimum, the emission energy reduction is the Stokes shift which is due both to a decrease in the excited state energy and an increase in the ground state energy at the relaxed geometry. After emission the structure can then relax back to the ground state minimum.

ative to the minimum ground state structure). As the minimum excitation energy is 3.29 eV, this means direct excitation over the barrier is energetically allowed. Beyond the barrier in the outer well the ground state optimized and excited state optimized energies converge, showing that the ground state optimized geometry is a good approximation for the excited state optimized geometry in the outer well.

The resulting energies and radiative lifetimes along this C_{2v} path are shown in Figure 4.13. The first two energy levels shown are of B_2 irreducible representation. At the inner well minimum, these are the lowest two excited states. This is one advantage of calculating the energy of the C_{2v} symmetric structures. The high symmetry makes it clear that these B_2 levels can cross the other levels without an avoided crossing. These levels originate from the T_1 and T_2 representations of T_d symmetry after the symmetry is broken to C_{2v} during relaxation in the excited state.

The second B_2 level originates from the T_2 to which the state is vertically excited upon absorption. The ~ 0.5 eV difference between the two B_2 levels found when relaxing in the lowest excited state makes it appear unclear how the state can relax to the lowest singlet as expected from Kasha's rule. However this is clearified by attempting to relax the structure in the second B_2 excited state. When doing so the 0.5 eV gap disappears and the levels become nearly degenerate.

Once the B_2 levels become essentially degenerate, it is difficult to search for a minimum energy on the potential surface where this occurs. The gradient calculations do not handle this near degeneracy well, often leading to sporadic steps when trying to minimize the energy of the second excited state. One structure found had an energy of ~ 3.24 eV (relative to the minimum ground state structure), which is close to the absorption energy. The ground state energy of this structure was raised 0.34 eV, which would give a fluorescence emission of about 2.9 eV (430 nm) if the fluorescence occurred from this minimum. This corresponds to an overall Stokes shift of ~ 0.4 eV.

However the excited state getting 'stuck' in the second B_2 level is unlikely. When the energy levels are not well separated relative to the vibrational energies, then the Born approximation allowing separation of the electronic and nuclear wave functions begins to fail. Therefore the excited state relaxation probably occurs via mixing of the B_2 levels, and once in the lower B_2 level the state can relax to much lower energy. This in turn opens up the gap
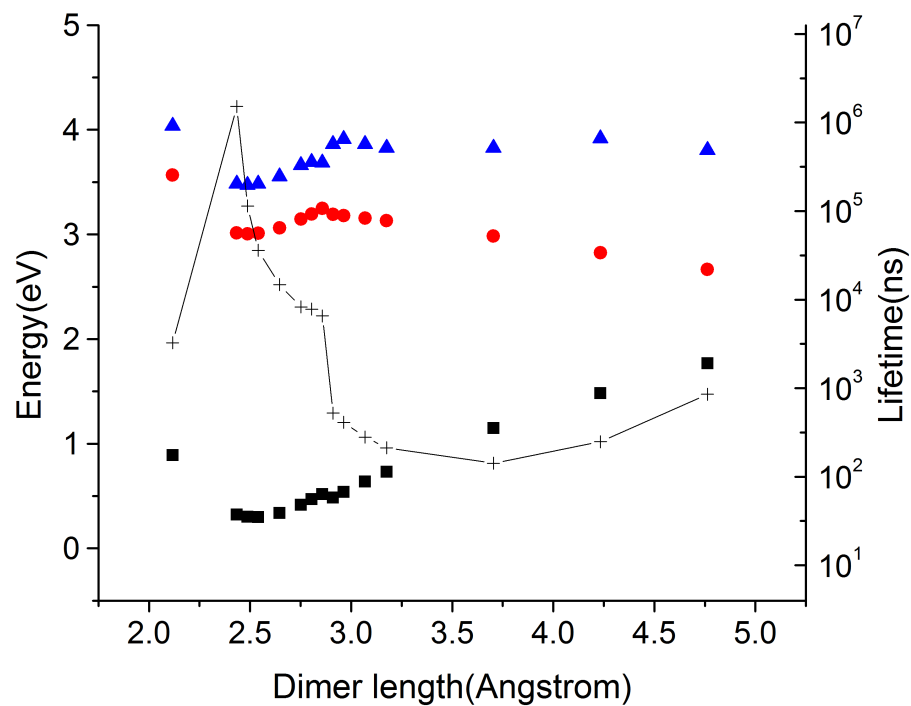
Figure 4.13: Geometries obtained by relaxing $Si_{29}H_{24}$ in the first excited state with one dimer constrained to a given length and the structure having C_{2v} symmetry. Radiative lifetime (+) of the first excited state is given versus dimer length. The ground state (■) and first two excited states (●,▲) energies relative to the ground state minimum are shown for reference.

to the nearest excited state level, so the Born approximation becomes valid again.

The C_{2v} symmetric geometries were found to not be the minimum energy structures. Relaxing the lowest excited state without symmetry constraints resulted in a geometry with C_s symmetry. This inner well minimum was verified to be a local minimum by numerically calculating the Hessian. A new path was then calculated by 'walking' the structure along the excited state potential energy surface by expanding the dimer length, allowing the structure to relax in C_s symmetry while holding the dimer length fixed, and repeating to obtain the path.

Surprisingly this path did not appear to be yielding a double well structure, and the oscillator strength remained low. At about 3.2 Å the geometry relaxation resulted in a quite different structure, which lowered both the excited state and the ground state energies. Performing geometry relaxations from this structure as the dimer was now shortened led to a different path toward a different inner well minimum. These two paths are shown in Figure 4.14. Therefore the excited state energy surface must be fairly roughly with several different 'troughs' in it. In the first trough the excited state energy increased beyond 3.5 eV without a sign of a double well, beyond this the trough must have become very shallow or unstable to allow the relaxation into a different trough. Moving along the minimum energy structures in this second trough gives a path with a larger oscillator strength as well as a double well.

The double well path along the excited state surface for structures with C_s symmetry is shown in Figure 4.15. The lower ground state energy of this path reduces the Stokes shift. Also the barrier to the outer well is lowered to about 3.15 eV (relative to the minimum ground state), making direct excitation over the barrier energetically more favorable than seen in the C_{2v} path.

A small kink in the ground state energy is seen at about 3.0 Å along these excited state optimized paths. This is due to the 'direction' in nuclear coordinate space not being just a straight line. Near the barrier peak the ground state energy briefly decreases even though the dimer is being stretched further. This indicates that the outer well is closer to the ground state minimized structure (at that dimer length) than the inner well structure is. This seems to be a generic feature as this kink is seen in all the excited state

Figure 4.14: Geometries obtained by relaxing $Si_{29}H_{24}$ in the first excited state with one dimer constrained to a given length and the structure having C_s symmetry. Two different structures were found. The ground state and first excited state for the two paths (■,●) are shown with energies relative to the ground state minimum.
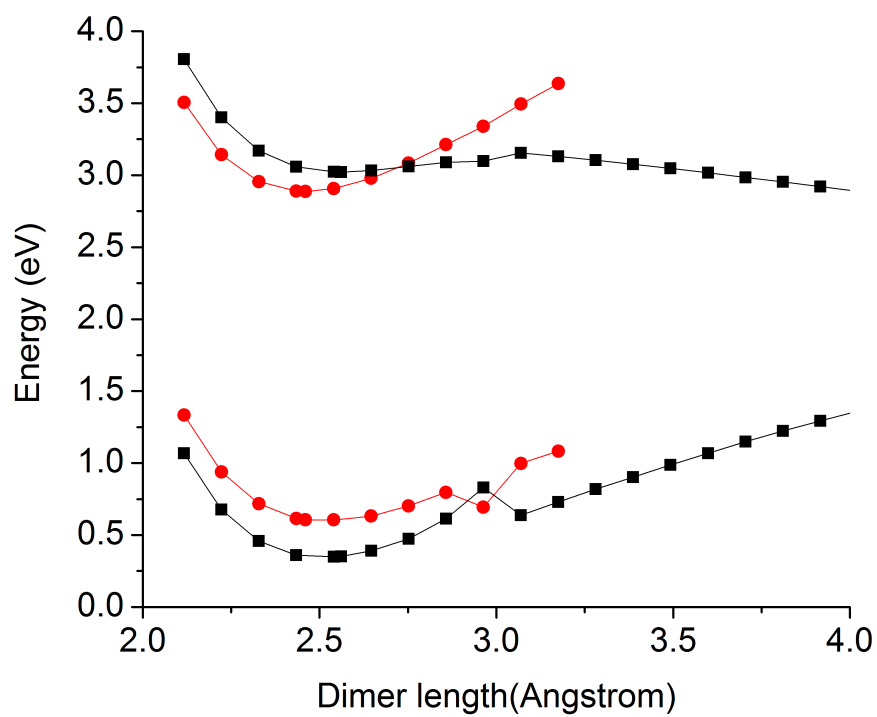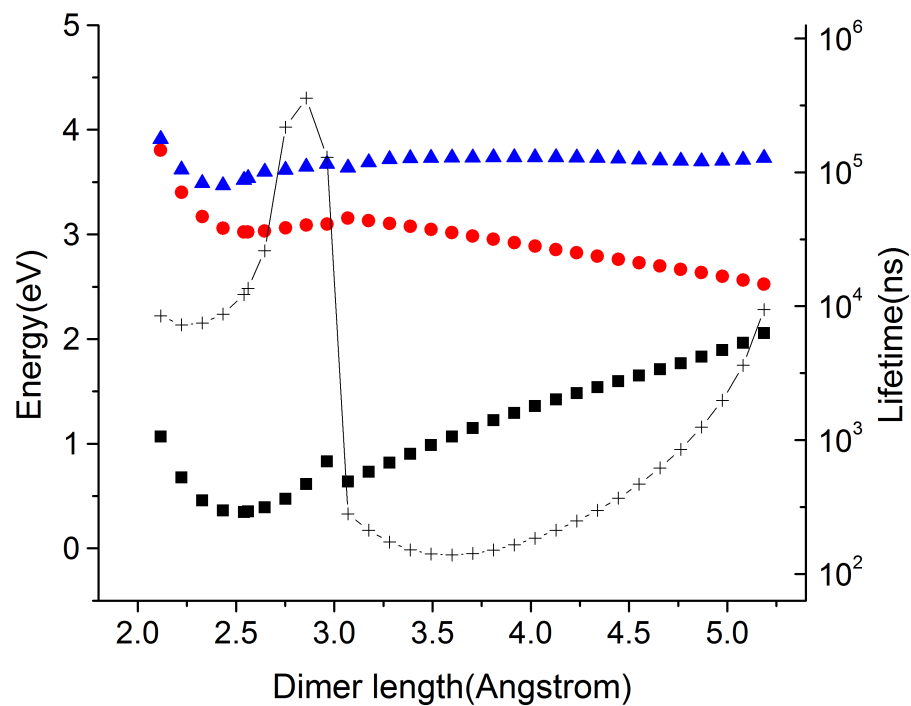
Figure 4.15: Geometries obtained by relaxing $Si_{29}H_{24}$ in the first excited state with one dimer constrained to a given length and the structure having C_s symmetry. Radiative lifetime (+) of the first excited state is given versus dimer length. The ground state (■) and first two excited states (●,▲) energies relative to the ground state minimum are shown for reference.

optimized paths.

Along the C_s double well path the lifetime drops several orders of magnitude as the dimer length increases past the barrier length. The lifetime minimum is on the order of 100 ns. Emission at the barrier would be 2.52 eV (490 nm), while emission from the structure on the path with the shortest lifetime would be 1.95 eV (640 nm). The outer well was found to have no minimum. The expected minimum can be estimated from the distance of the Si atoms of the 'missing' dimer in the $Si_{29}H_{26}$ (5 dimer) structure which was found to be 5.2 Å . However along the double well path, at about 5.2 Å the structure becomes unstable to relaxing with the excited state (A_2 representation) running into the singlet ground state (A_1 representation).

The dimer mechanism therefore demonstrates some of the correct qualitative features. It provides a means for the fluorescent lifetime to be decreased by several orders of magnitude. There is also a board range of emission energies which can have short lifetimes. The shorter lifetime can be reached by direct excitation, either to the outer well, or just to a shallow inner well with access to the top of the barrier is sufficient.

Now that the dimer mechanism has been explored in more detail, it is clear there is still need for improvement. Adam Smith studied the fluorescence lifetime of the 1 nm silicon nanoparticles and reported broad emission with a peak at 410-430 nm (3-2.9 eV) with a tail to over 600 nm (2.1 eV) and a lifetime of 3 ns independent of the emission wavelength [83]. The dimer double well mechanism shown here allows for broad emission from the 1 nm silicon nanoparticles. However the Stokes shift from the outer well is predicted to be too high for emission near 3 eV. Additionally, while the predicted lifetime is fairly flat on the log scale in the outer well, it still varies by a factor of two between the 490 nm and 640 nm emission.

The outer 'well' poses other difficulties as well. Instead of a minimum, there is a conical intersection with the ground state. Therefore relaxation after crossing the barrier leads to a method for non-radiative recombination back to the ground state potential energy surface. Furthermore, as internal conversion should happen on the order of picoseconds [93], which is orders of magnitude faster than the radiative lifetime, relaxation in the outer well would not result in the emission seen. The proposed 'self-trapped' exciton does not exist as the outer well is not stable.

If the calculated energy curve was slightly incorrect and a shallow mini-

mum in the outer-well did exist, there is another problem with stability. The relaxation in the outer well results in a structure similar to the $Si_{29}H_{26}$, except with two hydrogens replaced with dangling bonds. With a dimer bond dissociated this far, and the dangling bonds on the two Si atoms protruding where solvent can easily access it, this should not be chemically stable. However the particles are experimentally found to be robust against photo-bleaching [88].

These issues indicate that population of the outer well must actually be a slow process for the dimers to play a vital role in the fluorescence mechanism of the 1 nm silicon nanoparticle. The existence of the outer well is crucial as it provides for orders of magnitude increase of the radiative rate near the transition between the wells as well as the outer well. Thus it is only necessary to be near the barrier, and not over the barrier to access the regions of increased radiative rates. Furthermore, while direct excitation across the barrier is energetically allowed, vertical excitation during absorption and the large nuclear deformation required to go over the barrier should suppress such transitions. It is emission near the barrier, not from the outer well, which is the leading radiative process here.

The discovery of multiple troughs in the excited state potential energy surface indicate even the inner well potential surface is likely to be rich in structure. The double well path of C_s symmetric structures, gave an inner well minimum only 130 meV below the barrier height. Such a shallow well is only about twice the energy spacing of most of the silicon vibrations in the particle. This is ideal for confining the particle in the inner well, but still allowing access to the radiative regions near the barrier peak.

At the inner well minimum the ground state energy of the C_s double well path is 50 meV lower than the C_{2v} path. However the excited state energies are nearly degenerate, with some portions of the C_s inner well lower in energy than the corresponding dimer length structure of C_{2v} symmetry while other portions are slightly higher in energy. Therefore if the structure relaxes into the 'trough' of the C_s double-well path, the C_{2v} double-well path is energetically accessible as well.

If there are many local minima in the excited state surface near the barrier peak, the large change in the ground state energy (~ 0.25 eV) between the two known C_s troughs indicate such a scenario could help explain the large range of Stokes shift. Direct excitation to these local minima 'traps' is guaranteed

to be energetically allowed due to the barrier height itself being slightly less than the absorption energy. As the local minima are in the inner well, this is also more favorable than outer-well excitation due to vertical transition during absorption.

The C_s double well barrier has an emission of 455 nm, and the C_{2v} double well barrier has an emission of 490 nm. There are N=53 nuclei in the 1 nm particle, so after removing translations and rotations the excited state potential energy surface is a 3N-6=153 dimensional surface. Here we have only focused on some symmetric paths on this surface. However the excited state minimum energy geometry was found to have C_s symmetry. Therefore the C_s symmetry double well path is expected to represent the minimum energy path to the barrier, a saddle point. Likewise, the C_{2v} symmetry path is expected to be a higher order saddle point. Therefore while there are many more paths across the barrier, these stationary points should give the predominant energies in the emission. This predicts there are two broad peaks in the emission at 490 and 455 nm.

These predictions can be compared to the experimental emission energy of 1 nm silicon nanoparticles which were recently measured at the Daresbury Synchrotron Radiation Source [116]. The particles were dried on a substrate, placed in a vacuum, and cooled to 10 Kelvin. The emission in response to a range of excitation energies is show in Figure 4.16. The emission spectra is found to be largely independent of excitation energy from 4.6 eV up to 7.5 eV. The emission appears to be a peak near 435 nm with a shoulder in the longer emission wavelengths.

The emission is fit well with two gaussians as shown in Figure 4.17. The fitted peaks are at 435 and 480 nm, with full width-half max of 48 nm and 103 nm respectively. The fit error for the center location of the peaks is less than 1 nm for the main 435 nm peak, and 6 nm for the broad 480 nm peak. This fits the prediction of two peaks, although the predicted wavelengths were overestimated by 20 and 10 nm respectively.

The view that the silicon nanoparticles retain a sense of their 'indirect gap' nature even as small nanostructures [82, 78, 79, 80, 81], fits conceptually with the radiative rate increase at the edge of the inner well instead of the bottom. Due to that indirect nature seen in this current study, it is suggested single-point energy calculations are not well suited for discussing the fluorescence. Furthermore the shallow inner well and importance of the region near the

barrier illustrates that a harmonic calculation of the vibrational modes in the excited state is insufficient as the strongly an-harmonic nature of the surface cannot be ignored. Calculating the values along at least a couple paths has been shown here to allow a description of the emission spectra.
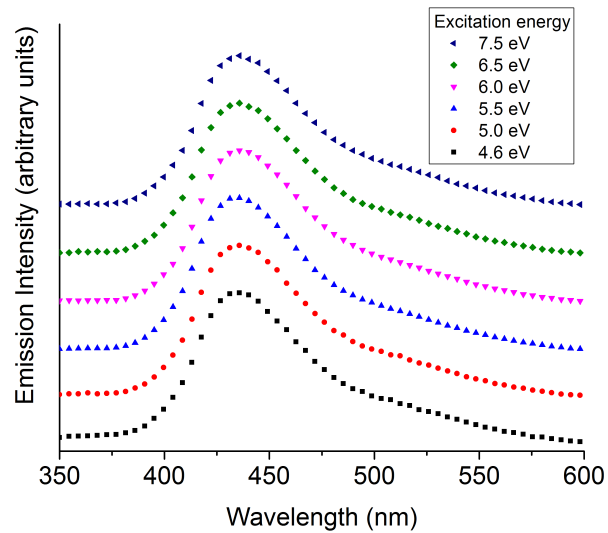
Figure 4.16: Emission spectra of 1 nm particles under a range of excitation energies. Spectra have been vertically offset for ease of comparison.
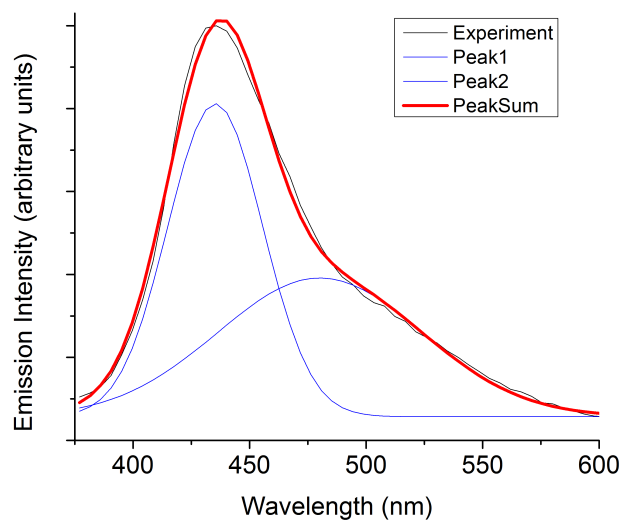

Figure 4.17: Emission of 1nm particles under 4.6 eV excitation, fit to two gaussian peaks. The peak centers were found to be at 435 and 480 nm.

Chapter 5

Interaction with Aqueous Fe(II) Ion

In principle, any interactions of the silicon naonparticles with the environment can be used to manipulate the particles or sense details of the environment. Recent experiments in our group and that of collaborators have shown particular promise for interactions with ions in solutions. They have demonstrated that such interactions can be used to pattern thin films of particles via electro-plating them in the presence of salts [19]. Also of note is an electrochemical device capable of using the particles to sense glucose in the presence of the particles, demonstrating the potential of these silicon nanocrystals in biosensing applications [20].

The success of existing applications is encouraging, however these devices were made with little understanding of the underlying charge interactions with the particles. Furthermore, it is clear that these devices have only begun to touch upon the full variety of interactions with ions that can occur. More knowledge of the electronic structure of these particles, and the effect ion interactions can have on this structure is crucial to allow greater diversity of applications and better selectivity in sensing devices.

In this chapter, first we will present experimental evidence of charge complexes forming between 1 nm silicon particles and aqueous ferrous (Fe^{+2}) ions. Then density functional theory (DFT) calculations will be presented with a proposed model of the charge complex structure. Solvation energies for the ions will be included with the Conductor-like Screening Model (COSMO) to estimate the stability of this complex in solution.

5.1 Absorbance measurements of silicon nanoparticle and ion solutions

Silicon nanoparticles were created with the anodization etching technique previously described (Chap. 2) with a predominant size of 1 nm, and suspended in isopropanol. The suspsension was then filtered with a 0.22 micron filter. The resulting solution appeared clear to the eye in visible light and fluoresced strongly blue under a UV lamp. Further filtering with a 50 nm filter negligibly changed the concentration as indicated by fluorescence.

Five solutions were created for absorption measurements. A 1.1 mM solution of ferrous chloride ($FeCl_2$) and ferric chloride ($FeCl_3$) were each created by adding the corresponding salt to de-ionized water. After the absorbance of an iron solution was measured, it was mixed 9:1 with the stock silicon nanoparticle solution and the absorbance of the resulting mixture was measured. A solution containing 9:1 de-ionized water to nanoparticle solution was also created, to provide a solution with the same amount of water and silicon nanoparticle solution as the previous mixtures.

While the proposed structure of the nanoparticles is non-polar, the 9:1 mixture of water and isopropanol resulted in no precipitation and appeared stable. Water was chosen to be the predominant solvent for the ease in obtaining solutions of metallic ions. The iron chlorides separate into iron and chloride ions with solvation shells in water [117], while iron interactions with isopropanol are comparitively weak, requiring strong anhydrous conditions for isopropanol coordination with iron [118].

Absorbance measurements were recorded with a Varian Cary 5G spectrophotometer, with samples placed in a fused quartz cuvette. The background was corrected for dark counts and the spectra from a cuvette with de-ionized water was subtracted as a blank. The result is show in Figure 5.1.

The dilute silicon nanoparticles absorb very little, although features at 225nm and 275nm can still be seen. This corresponds to the 4.5 and 5.5 eV peak seen by measurements previously reported of more concentrated samples [37]. The $FeCl_2$ solution containing Fe^{+2} ions is relatively featureless in this range, while the $FeCl_3$ (Fe^{+3} ions) absorbs strongly with a broad peak at 290nm.

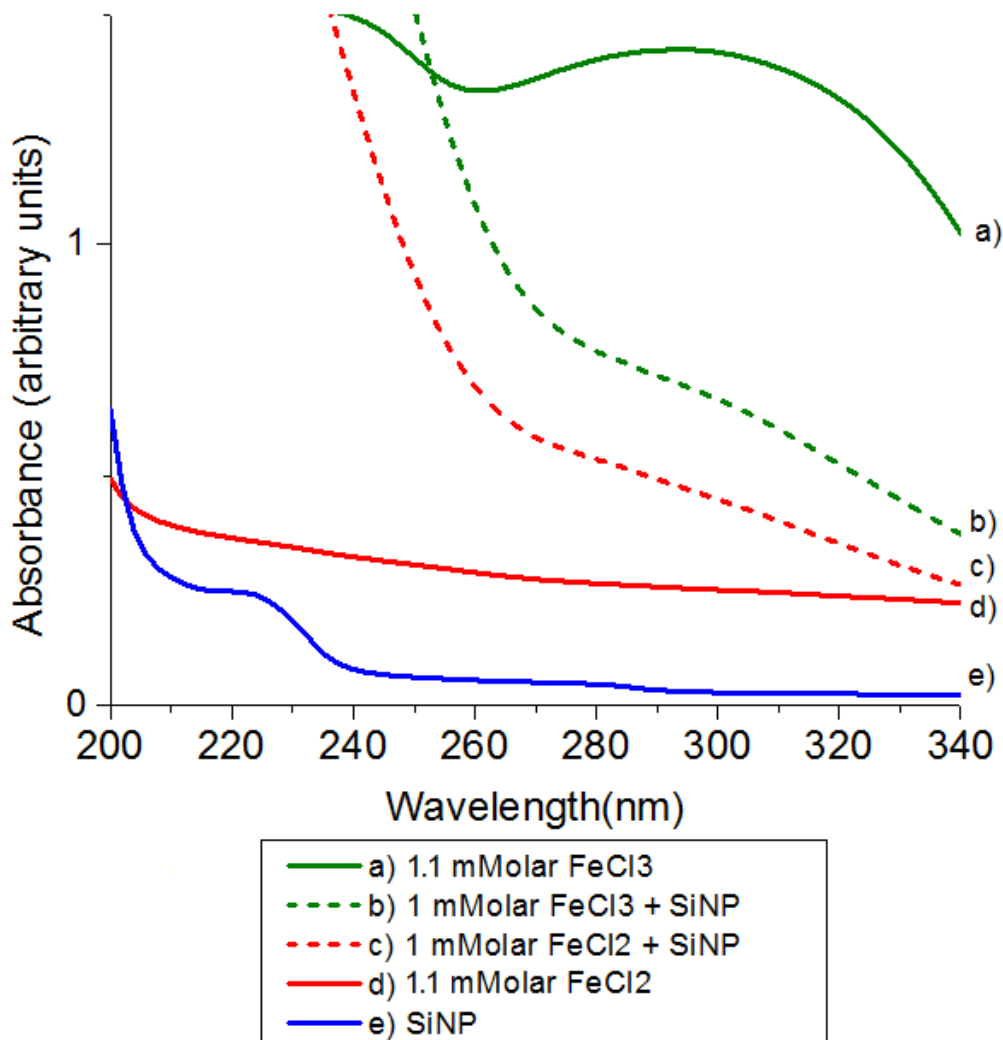With both ions, mixing with the silicon nanoparticle solution significantly

Figure 5.1: Absorbance of solution of 1 nm silicon particles (SiNP), Fe(II), Fe(III), and combinations. The concentration of silicon nanoparticles are the same in the three solutions containing them.

affects the absorption spectra. Neither ion and particle mixture is a linear combination of the absorbance of the parts, indicating a strong interaction and possibly the formation of a charge complex. Furthermore, the features of both mixtures have the same general feature. As the wavelength decreases, the absorbance slowly increases until about 270 nm where a bend occurs in the spectra with a faster increase in absorbance at lower wavelengths. This may indicate the resulting structures are similar in each case.

5.2   COSMO solvation model

A general method of treating interaction with solvents are continuum solvation models [119]. From the point of view of the solute, solvent molecules will move stochastically presenting on average a continuum dielectric material which locally polarizes in response to the charge distribution of the solute. In the simplest models, the solute is placed in a spherical cavity surrounded by dielectric medium. More realistic models form the cavity from an enlarged Van der Waals sphere around each atom. The difficulty then becomes solving for the resulting potential due to this complicated dielectric surface.

The Conductor-like Screening Model (COSMO) simplifies this greatly by treating the cavity as a conductor surface and then scaling the surface charge to approximate a finite permittivity [120]. This works because the surface charge density on a dielectric material of a given geometry in response to a charge distribution will scale as [121]

$$f(\epsilon) = \frac{\epsilon - 1}{\epsilon + x} \tag{5.1}$$

where ϵ is the relative dielectric permittivity, and $0 < x \leq 2$ depending on the geometry [120]. The conductor screening limit is equivalent to $\epsilon \to \infty$ where $f(\epsilon) = 1$. A solvent with a large permitivity is thus well approximated by the conductor limit. The COMSO method solves for the conductor case, and estimates $x = 1/2$ to scale the results to realistic dielectrics. For most dielectric solvents, and particularly water, the relative error will be small as the dependence on x is small. Weak dielectrics can have a larger relative error, but the charging screening energy is small in this case and thus the absolute error is small.

A representation of the solvent cavity is created by denoting an excluded radius for the solvent molecules from an atom, equal to the characteristic radius of the atom plus the characteristic radius of the solvent 'probing'. In the COMSO method, a set of points are evenly distributed on such a sphere from each solute atom. If the point is inside one of the other excluded volumes, it is discarded. The remaining points are then collected into segments of roughly equal area, and then a surface point charge assigned to the center of the segment.

With the surface defined as a set of charges, solving the charge distribution then becomes a boundary value problem for a conductor. If the electrostatic potential at each surface location is collected in a vector Φ, the vanishing of the potential at the conductor surface gives

$$\Phi_{\text{total}} = \Phi_{\text{solute}} + \mathbf{A}\mathbf{q} = 0 \tag{5.2}$$

where the total potential is broken into the term due charge distribution of the molecule in the cavity and a term due to the surface charges. This is represented with q as a vector listing all the surface charges, and a matrix A representing the Coulomb potential operation. The matrix A depends only on the geometry and once calculated, can be inverted to solve directly for the charges

$$\mathbf{q} = \mathbf{A}^{-1}\Phi_{\text{solute}}. \tag{5.3}$$

The solvent charges can therefore be solved for efficiently once the geometry is specified and A^{-1} is calculated. This is important because the solution of the solute molecule charge distribution will depend on the solvent polarization, and therefore this interaction is included in the self consistent field (SCF) iterations when solving for the molecular orbitals. This can be used at the Hartree-Fock or Kohn-Sham density functional level of theory.

5.3 Charging and aqueous energies of $\text{Si}_{29}\text{H}_{24}$ and Fe

The interaction of a silicon nanoparticle with metallic ions may result in a redox type reaction resulting in two free charged species in water. It is also possible that charge is transfered between the species even if a charge com-

plex is formed. Because the bonds in a solvation complex are much more ionic than covalent in nature, and the ligand bonds are usually longer than ordinary single covalent bonds, the oxidation state of the metallic atom remains a useful quantity when discussing charge complexes. Therefore knowledge of the energies of various ions of the nanoparticle in solution compared to metallic ions is helpful in narrowing the range of possible interactions. Here iron is used as a test case, whose known ionizations and solvation energies allow testing the accuracy of the calculation methods at each step. Additionally iron is a first row transition metal, providing for easier computations.

Calculation of the charging energies of $Si_{29}H_{24}$ and Fe were done at the UHF-DFT level using the B3LYP functional with the TURBOMOLE quantum computational package [112]. The TZVP basis was used which is a triple split valence basis with polarization functions added for each atom [113, 114, 115]. The energy of the species in water were obtained with the COSMO method of approximating the particles embedded in a continuum dielectric of $\epsilon = 78.4$ and using a solvent radius of 1.3 Angstrom.

The energy of the silicon particle and iron atom in vacuum (or 'gas phase') at various charging energies is given in Table 5.1. The electronic density used for the density functional calculations is built from an unrestricted Hartree-Fock (UHF) type slater determinant, which cannot correctly handle the degeneracy of the iron orbitals. Instead of the electrons being shared equally between the 5d atomic orbitals, the electrons are placed in the first unfilled shell. The calculated ionization energies of iron are with-in 3% of the known experimental results, showing the accuracy of this method. The spin state of iron as well as its +2 and +3 ions are predicted as expected.

It is noted however that the calculation predicts the electronic structure of the Fe(+1) ion to be $[Ar]3d^7$, while the known configuration is $[Ar]3d^64s^1$ [122]. The DFT calculation with 3 unpaired spins had negligible spin contamination $\langle S^2 \rangle = 3.754$, as did the 5 unpaired spins calculation with $\langle S^2 \rangle = 8.752$, so the calculations are converging appropriately. This problem with the Fe(+1) spin has been commented on by other researchers, noting however that DFT has displayed good performance with the properties of many transition metal compounds [123].

The neutral silicon nanoparticle initially has T_d point group symmetry, with a triply degenerate highest occupied orbital (HOMO). This provides for the possibility that the doubly charged ion will be a triplet state. While

the T_d symmetry is broken in the charged states, the doubled charged state retains enough symmetry for the triplet to be slightly lower than the singlet at this level of calculation, having only a spacing of 4 meV.

The silicon particle ionization energy and electron affinity are found to be 7.29 eV and 1.46 eV respectively. This is much closer to the atomic values of silicon (8.15 eV and 1.38 eV respectively) than to the crystalline bulk silicon values of 4.05 eV and 5.17 eV. This further demonstrates the silicon nanoparticle is most appropriately discussed in the molecular regime than approximations from the crystalline condensed matter regime.

The energy of the silicon particle and iron atom in water at various charging energies is given in Table 5.2. The predicted spin state of the species is not changed from the vacuum computation. As the dielectric screening is only sensitive to the charge distribution, this indicates that the charge distribution of the different spin states is not sufficiently different to allow the screening energy to change the spin level ordering.

The solvation energy is calculated as the drop in energy from the gas phase to liquid phase energy. These values are known experimentally for the ferrous and ferric iron ions, and the calculations provide a poor fit with close to a 40% relative error. This indicates the interactions of iron with water are not adequately represented here. The relative error is quite similar for the two ions compared to experiment (Fe^{+2} and Fe^{+3}), hinting that a common interaction could resolve the discrepancy.

The inadequacy of the continuum solvent model for the transition metal ion is due to a failure of the assumption that the solvent molecules will move sufficiently randomly about the ion for a continuum average approximation to be appropriate. Clearly the water molecules far from the ion will be uncorrelated to the iron atom and therefore fit the approximation well, but at short distance the lone pairs of the oxygen in water will interact with the unfilled orbitals (weak 'dangling bonds') of iron to form a complex with water.

The solvation shell is not made of strong covalent bonds, and the water molecules still do rearrange with inner solvation shell exchanges occurring on a time scale of about 10 nsec for Fe^{+2} ions [117]. The structure lasts long enough to be studied via NMR, x-ray scattering, and neutron diffraction which determined the first solvation shell of Fe^{+2} and Fe^{+3} (as well as most transition metals) to contain 6 water molecules.

1 nm silicon nanoparticle $Si_{29}H_{24}$			
charge	unpaired electrons	energy (Hartree)	eV (relative to neutral)
-1	1	-8409.20012	-1.462
0	0	-8409.14638	0
+1	1	-8408.8784	7.292
+2	0	-8408.53407	16.662
	2	-8408.53422	16.658

Iron atom			
charge	unpaired electrons	energy (Hartree)	eV (relative to min)
Fe(0)	0	-1263.46682	3.531
	2	-1263.56065	0.978
	4 (lowest energy)	-1263.59658	0
Fe(+1)	1	-1263.26616	8.991
	3 (lowest energy)	-1263.31269	7.725
	5	-1263.30575	7.914
Fe(+2)	0	-1262.37438	33.258
	2	-1262.64292	25.951
	4 (lowest energy)	-1262.70319	24.311
	6	-1262.53584	28.864
Fe(+3)	1	-1261.35176	61.085
	3	-1261.36543	60.713
	5 (lowest energy)	-1261.54936	55.708
	7	-1259.19302	119.828

energy relative to neutral atom				
	calculated (eV)	experimental value	error	%error
Fe(+1)	7.725	7.9024	-0.1774	-2.2
Fe(+2)	24.311	24.0901	0.2209	0.9
Fe(+3)	55.708	54.7421	0.9659	1.8

Table 5.1: Calculated ion energies of silicon nanoparticle and iron in vacuum. Experimental values are from ref. [124].

1 nm silicon nanoparticle $Si_{29}H_{24}$ in water			
charge	unpaired electrons	energy (Hartree)	eV (relative to neutral)
-1	1	-8409.23676	-2.314
0	0	-8409.15173	0
+1	1	-8408.95054	5.475
+2	0	-8408.73897	11.232
	2	-8408.73911	11.228

Iron atom in water			
charge	unpaired electrons	energy (Hartree)	eV (relative to min)
Fe(0)	0	-1263.46914	3.484
	2	-1263.56114	0.98
	4 (lowest energy)	-1263.59717	0
Fe(+1)	1	-1263.38399	5.801
	3 (lowest energy)	-1263.43046	4.536
	5	-1263.42526	4.678
Fe(+2)	0	-1263.09697	13.611
	2	-1263.11084	13.234
	4 (lowest energy)	-1263.17117	11.592
	6	-1263.00512	16.111
Fe(+3)	1	-1262.4044	32.457
	3	-1262.41824	32.086
	5 (lowest energy)	-1262.60196	27.081
	7	-1260.24751	91.15

Iron solvation energy in water				
	calculated (eV)	experimental value	error	%error
Fe(+2)	12.734	20.82	-8.086	-38.8
Fe(+3)	28.643	46.547	-17.904	-38.5

Table 5.2: Calculated ion energies of silicon nanoparticle and iron in water. Experimental values for solvation energy are from ref. [117].
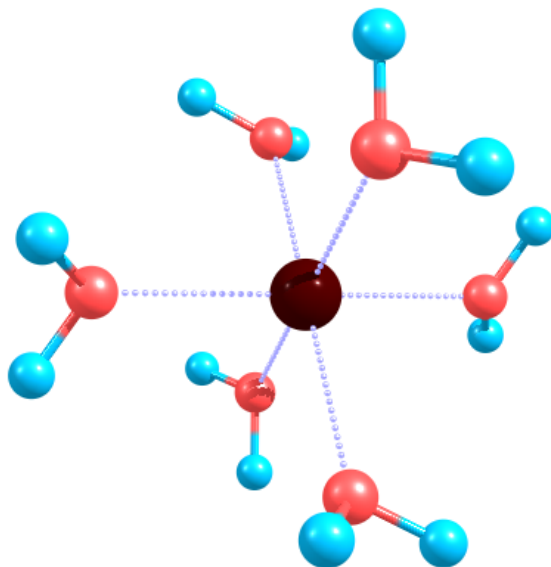
Figure 5.2: Structure of ferrous ion (Fe^{+2}) in hexa-aqua complex.

iron hexa-aqua solvation complex			
	energies in Hartree		
	Fe	$Fe(H_2O)_6$	$Fe(H_2O)_6$ in dielectric
Fe(0)	-1263.596579	-1722.239998	-1722.273072
Fe(+1)	-1263.312692	-1722.100865	-1722.197558
Fe(+2)	-1262.703186	-1721.786762	-1722.089763
Fe(+3)	-1261.549362	-1721.175465	-1721.853877

	energies in eV			
	relative	solvation	experiment	%error
Fe(0)	0	1.293		
Fe(+1)	2.055	6.964		
Fe(+2)	4.988	20.616	20.82	-0.98
Fe(+3)	11.407	45.594	46.547	-2.05

Table 5.3: Calculated iron ion and solvation energies of ion in water. Experimental values for solvation energy are from ref. [117].

The gas phase hexa-aqua complex structure for ferrous iron (Fe^{+2}) is illustrated in Fig. 5.2. The oxygen attach as ligands in a cubic structure. Hydroxide ions can also serve as a ligand, but the hexaaqua structure is the preferred structure for ferrous ions in acidic as well as weak basic conditions having a pH less than about 8 [125].

Higher order and weaker solvation shells of water will form around this inner solvation complex due to hydrogen bonding with the inner shell water molecules. While including the higher order complexes leads to some improvement, a combined first inner-cluster + external continuum model for water has been found to account for the vast majority of the complex shell interaction for Cu(+2) ions [126, 127] and has preformed will in studies with iron ions [125, 128].

The hexa-aqua solvation complex with an iron atom was calculated with the spin values previously determined. The results are summarized in Table 5.3. For the singly charged and neutral iron the hexa-aqua structures relaxed away from the cubic like structure, especially for the neutral iron the water molecules primarily are aligning to each other. In order to remain consistent for comparison, six water molecules were used for the solvation of each of the four iron atom charges considered here. The solvation energy was calculated from the change in energy of the reaction

$$Fe^{+x}{}_{(gas)} + 6\ H_2O_{(solv)} \longrightarrow [Fe(H_2O)_6]^{+x}{}_{(solv)} \qquad (5.4)$$
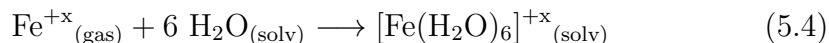
where the solvent phase energy of a single water molecule was found to be -76.43816 Hartree (and a gas phase energy of -76.42592 Hartree). The resulting solvation energies are now with-in 3% of the experimental values, therefore bringing the calculation accuracy to the same level as the ionization energies in vacuum.

In the explicit water complexes with iron, Mulliken or Loewdin population analysis does not give a charge assignment matching the expected oxidation state. The Loewdin charge ranges from -0.29 to 0.40 (atomic units), never even reaching a full charge when the oxidation state is Fe(+3). The Mulliken charge assignment doesn't even demonstrate a monotonic increase with oxidation state. The inability to extract the oxidation state from population analysis has been previously noted in literature, where charge assignments were found to depend more heavily on the electro-negativity of the ligand

[129]. However the spin density of Mulliken, Loewdin, and Natural orbital population analysis all gave matching assignments of unpaired d-orbital electrons on the iron atom. The unpaired electron assignments therefore provide the best trend to allow identification of the iron oxidation state for these ion complexes.

With vacuum surroundings, the charge in the silicon particle is distributed quite uniformly over the particle. The dipole moment for the negatively charged, neutral, singly positive charged, and the singlet state of the doubly positive charged nanoparticle were all less than 0.01 Debye. Only the doubly charged triplet state had significant non-uniform charge distribution, with a dipole of 3.13 Debye.

Embedded in the aqueous dielectric, the dipole moment of the silicon nanoparticle changed appreciably only for the singly positive charge (now 5.62 Debye) and the doubly charged triplet state (now 7.37 Debye). Unlike the iron atom, the silicon particle does not have dangling unfilled orbitals for solvation bonding with the lone pairs in the oxygen atoms of water. The solvent interactions with the silicon atom are therefore expected to be modelled adequately with the dielectric continuum model alone.

The calculated charging energies indicate a ferrous (Fe^{+2}) ion cannot be oxidized to Fe(+3) by the silicon nanoparticle in water due to energy constraints. Furthermore an Fe^{+2} ion cannot strip one or two electrons from a silicon nanoparticle in water and then freely separate. Therefore without additional energy somehow supplied externally, the ion energies restrict the interactions to those resulting in bound complexes.

If forming a complex with the nanoparticle, the iron will not have a full hexa-aqua shell. Therefore in the complex the relevant charge transfer energies for iron will be somewhere between the continuum dielectric alone and the hexa-aqua complex. Therefore it may be energetically favorable to transfer charge between a ferrous ion and a neutral nanoparticle in water, resulting in each being singly charged and bound.

While the iron(+1) oxidation state is not common in complexes, there are several known examples. One such complex is $[Fe(H_2O)_5NO]^{+2}$ from the well known 'brown ring test' used in organic chemistry, with both charged species in the complex having a single positive charge (NO^{+1}, Fe^{+1}) [130, 131]. Another example is $[(RS^-)_2Fe^+(NO^+)_2]^+$ again involving other singly charged species [132]. Monovalent iron is also known to occur in complexes

with porphyrins [133].

This leaves three classes of interactions for Fe^{+2} and $Si_{29}H_{24}$ in aqueous solutions. First, there is the possibility of no binding with the nanoparticle if water complexing in strongly energetically favorable. Since a redox type reaction resulting in charge transfer and free separate species is already ruled out, this first case of no bound complex at all would mean there is no direct reaction between the species. The second possibility is a charge complex forms in which the iron ion retains its double charge. The third possibility is a charge transfer between the species, and the interaction is strong enough to form a stable complex preventing the two (now charged) species from dissociating. A computational study of a proposed charge complex will provide an indication of the most likely scenario.

5.4 Charge complex of $Si_{29}H_{24}$ and $Fe(II)$

The 1 nm silicon nanoparticle $Si_{29}H_{24}$ has no terminations on its surface with lone electron pairs, such as an oxide or nitrogen group, which are commonly found in the ligands of a charge complex. However the surface reconstruction dimers pull to open up 4 hexagonal rings on the surface. A ferrous ion may sit within one of these rings, reducing the energy by effectively spreading the charge over a larger volume represented by the silicon nanoparticle. If the particle can act as an 'effective polarizable medium' better than the water, the charge complex may then be stable.

Structures were calculated at the UHF-DFT level with a TZVP basis set and the B3LYP functional using the TURBOMOLE quantum computational package [112]. The first structures were calculated without solvation models to investigate if the polarization of the silicon particle was a sufficient reduction in energy to prevent each species just becoming singly charged and separating due to Coulomb repulsion.

Initial attempts at placing the iron atom above the hexagonal silicon ring resulting in the iron atom falling below the ring into the particle interior during relaxation. A local minimum energy structure was found as shown in Figure 5.3. This 'interior' minimum was calculated for 0, 2, 4, and 6 unpaired electrons and found to exist in each case. The lowest energy structure contained 4 unpaired electrons, and $\langle S^2 \rangle = 6.066$ showing low spin contam-

ination. Mulliken and Loewdin population analysis both gave 3 unpaired electrons in the Fe d orbitals and none in the s and p orbitals. Considering the electronic configuration predictions of Fe(+1), this is in agreement with one charge transfered between the SiNP and the initial ferrous ion, leaving each singly charged.

The energy of the complex in vacuum as a function of the iron distance from the center of the silicon nanoparticle (the center nuclei) was calculated for this structure. At each distance the structure was relaxed in the 4 unpaired electron configuration. The inner local minimum was found to be a 0.09 eV deep well from the top of a transition point when moving through the hexagonal ring. Outside the silicon nanoparticle a second minimum was found (Figure 5.6). In this configuration the Fe atom rests on top of the hexagonal silicon ring. The minimum of this well is 0.43 eV below the barrier through the ring, and 1.90 eV below the energy of a distantly separated Fe(+1) ion and a singly charged nanoparticle as calculated from the previously obtained ion energies.

The COSMO solvation model was used to calculate how the dieletric screening energy of water affects this potential energy surface. The result is shown in Figure 5.5. The inner equilibrium is now shallower, with the barrier 0.07 eV above the inner minimum. The outer minimum is 0.57 eV below the barrier through the ring, and 2.45 eV below the long distance limit of a Fe(+1) ion and single charged nanoparticle in water. Near the outer minimum, the structure was allowed to relax for a configuration with 2 unpaired electrons and 4 unpaired electrons. The 4 electron case was the minimum energy, consistent with the silicon particle and iron atom each having a single charge and remaining spin aligned.

To obtain a better estimation of the binding energy of this complex, the first solvation shell of water around the iron atom must be included. When in the equilibrium position above the hexagonal silicon ring, roughly half of the iron atom is obscured from direct interaction with the solvent. So the silicon nanoparticle must replace 3 of the 6 water molecules in the iron solvation shell. The resulting structure is shown in Figure 5.4. The structure was allowed to relax and the total binding energy was evaluated by considering the dissociation reaction

$$[(Si_{29}H_{24})Fe(H_2O)_3]^{+2} + 3\ H_2O \longrightarrow [Fe(H_2O)_6]^{+1} + [Si_{29}H_{24}]^{+1} \qquad (5.5)$$

102
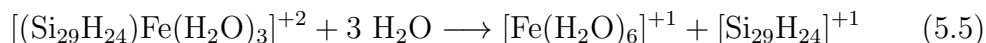
where all energies used the COSMO solvation model. The binding energy was found to be 0.49 eV. So the proposed complex is predicted to be stable against dissociation in water, despite the Coulomb repulsion due to each species being charged.
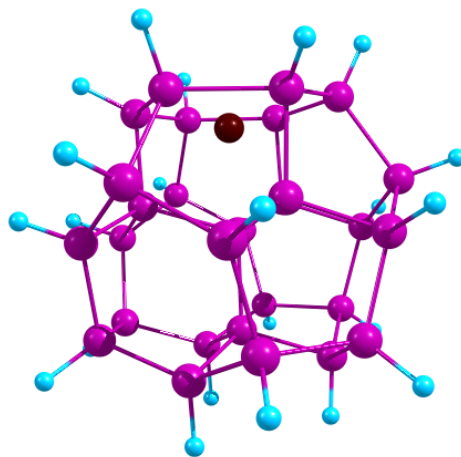
Figure 5.3: Complex of Fe(+2) and silicon nanoparticle, with ion sitting inside of particle.
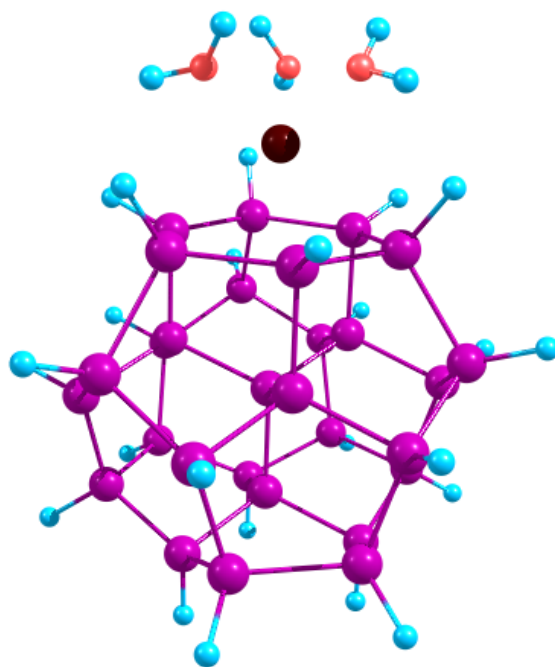

Figure 5.4: Proposed structure of complex of silicon nanoparticle, Fe(+2) ion, and water.

Figure 5.5: Energy of complex in vacuum versus Fe and center silicon atom separation. The zero of the energy is taken to be the energy of Fe(+1) and singly charged nanoparticle.
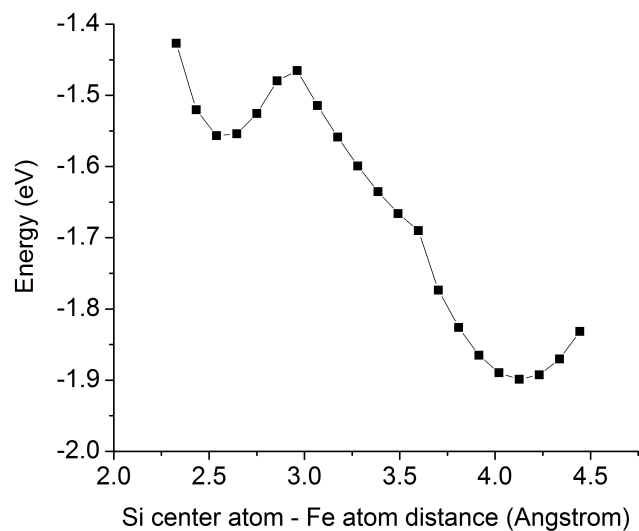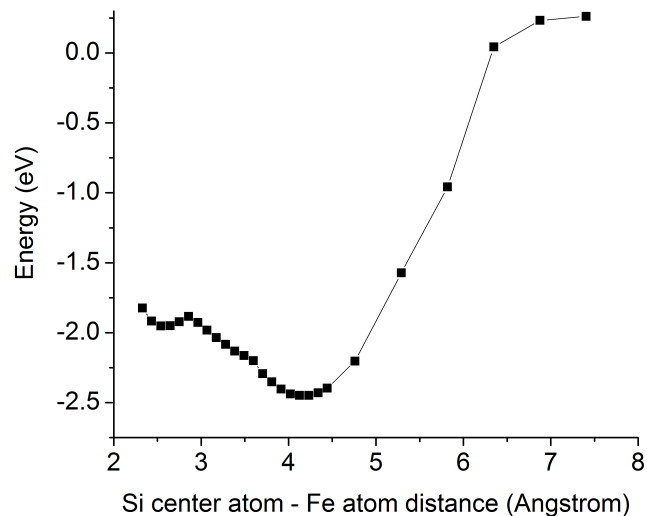

Figure 5.6: Energy of complex in water versus Fe and center silicon atom separation. The zero of the energy is taken to be the energy of Fe(+1) and singly charged nanoparticle.

Chapter 6

Conclusion

A comparison of Raman spectra of 1 nm silicon nanoparticles to the Hartree-Fock calculated vibrational modes of six different potential molecular structures found $Si_{29}H_{24}$ to be the most likely structure. This confirms previous findings by Mitas et al. in 2001 based on comparison of absorption spectra to calculated spectra [37], although disagrees with more a recent structure assignment based primarily on emission energies by Lehtonen et al. [51]. The $Si_{29}H_{36}$ bulk-like structure suggested by Lehtonen was also found to have a band gap of 4.5 eV according to TD-DFT B3LYP, while the $Si_{29}H_{24}$ structure with surface reconstruction dimers had a band gap of 3.3 eV in better agreement with experiment.

The calculated vibrational modes of the 1 nm particle were also compared to vibrational structure seen in low temperature photoluminescence data. The data indicated vibrational modes of 33 meV and 40 meV are coupled to the emission. These vibrations were assigned to two anti-symmetric dimer stretching modes calculated to be at 35 meV and 40 meV. This provides support for the proposal by Lannoo et al. [1, 2] that the dimers have a significant role in the fluorescence.

The double well of the dimer mechanism has been shown to exist, along with the associated increase in radiative rate near the barrier between the wells. With this mechanism fluorescent lifetimes are predicted to be ~ 100 ns. The self-trapped exciton proposed by Lannoo et al. was found to be unstable, with the outer well leading to non-radiative recombination with a conical intersection between the ground state and excited state. To match the peak emission seen in experiment as well as the robustness against photo-bleaching, emission should predominantly occur at the barrier instead of across it in the outer well.

The discovery of a complex excited state potential energy surface with multiple local minima in the inner well is suggested to play a role in the

fluorescence for the 1 nm silicon nanoparticle. The local minima can each have different minimum paths to a barrier transitioning to the outer well. They can also have different ground state energies, corresponding to different Stokes shifts. Because these structures are in the inner well, direct excitation populating these states should be efficient. The minimum barrier crossing (C_s symmetry) and a higher order saddle point (C_{2v} symmetry) predict emission of 490 and 455 nm respectively. These overestimate the experimental measurements by 10 and 20 nm respectively.

Absorption measurements of 1 nm silicon particles and iron in water indicate a strong interaction between the species. DFT with COSMO calculation of the ionization energies of $Si_{29}H_{24}$ and iron in water show that it is energetically forbidden to have a redox type reaction where charge is transfered and the resulting ions then freely leave in solution. A bound charge complex was found with the Fe atom sitting over a ring of silicon atoms on the nanoparticle's surface. The oxidation state of the iron is predicted to be $+1$, indicating a charge transfer between the species even though they remain bound. The structure is found to be stable with a minimum of 0.49 eV required to dissociate the complex.

References

[1] M. Lannoo, C. Deleue, and G. Allan. Theory of radiative and nonradiative transitions in for semiconductor nanocrystals. *J. Luminescence*, 70:170, 1996.

[2] G. Allan, C. Delerue, and M. Lannoo. Nature of luminescent surface states of semiconductor nanocrystallites. *Phys. Rev. Lett.*, 76:2961, 1996.

[3] GE Moore. Cramming more components onto integrated circuits. *Electronics*, 38(8):114–117, APR 19 1965.

[4] LT Canham. Silicon Quantum Wire Array Fabrication by Electrochemical and Chemical Dissolution of Wafers. *Applied Physics Letters*, 57(10):1046–1048, SEP 3 1990.

[5] AD Yoffe. Low-Dimensional Systems - Quantum-Size Effects and Electronic-Properties of Semiconductor Microcrystallites (Zero Dimensional Systems) and Some Quasi-2-Dimensional Systems. *Advances in Physics*, 42(2):173–266, MAR-APR 1993.

[6] Akram I. Boukai, Yuri Bunimovich, Jamil Tahir-Kheli, Jen-Kan Yu, William A. Goddard, III, and James R. Heath. Silicon nanowires as efficient thermoelectric materials. *Nature*, 451(7175):168–171, JAN 10 2008.

[7] Allon I. Hochbaum, Renkun Chen, Raul Diaz Delgado, Wenjie Liang, Erik C. Garnett, Mark Najarian, Arun Majumdar, and Peidong Yang. Enhanced thermoelectric performance of rough silicon nanowires. *Nature*, 451(7175):163–U5, JAN 10 2008.

[8] A. Feltrin, R. Bartlome, C. Battaglia, M. Boccard, G. Bugnon, P. Buehlmann, O. Cubero, M. Despeisse, D. Domine, F. J. Haug, F. Meillaud, X. Niquille, G. Parascandolo, T. Soederstroem, B. Strahm, V. Terrazzoni, N. Wyrsch, and C. Ballif. An Introduction to the Technology of Thin Film Silicon Photovoltaics. *Informacije Midem-Journal of Microelectronics Electronic Components and Materials*, 39(4):231–236, DEC 2009.

[9] JL Heinrich, CL Curtis, GM Credo, KL Kavanagh, and MJ Sailor. Luminescent Colloidal Silicon Suspensions From Porous Silicon. *Science*, 255(5040):66–68, JAN 3 1992.

[10] L. Patrone, D. Nelson, V. Safarov, M. Sentis, and W. Marine. Size dependent photoluminescence from si nanoclusters produced by laser ablation. *J. Lum.*, 80:217, 1998.

[11] K. A. Littau, P. J. Szajowski, A. J. Muller, A. R. Kortan, and L. E. Brus. A luminescent silicon nanocrystal colloid via a high-temperature aerosal reaction. *J. Phys. Chem.*, 97:1224, 1993.

[12] Aycan Yurtsever, Matthew Weyland, and David A. Muller. Three-dimensional imaging of nonspherical silicon nanoparticles embedded in silicon oxide by plasmon tomography. *Applied Physics Letters*, 89(15), OCT 9 2006.

[13] Xiaoming Zhang, Doinita Neiner, Shizhong Wang, Angelique Y. Louie, and Susan M. Kauzlarich. A new solution route to hydrogen-terminated silicon nanoparticles: synthesis, functionalization and water stability. *Nanotechnology*, 18(9), MAR 7 2007.

[14] Z. Yamani, W. H. Thompson, L. AbuHassan, and M. Nayfeh. Ideal anodization of silicon. *App. Phys. Lett.*, 70:3404, 1997.

[15] G. Belomoin, J. Therrien, A. Smith, S. Rao, R. Twesten, S. Chaieb, M.H. Nayfeh, L. Wagner, and L. Mitas. Observation of a magic discrete family of ultrabright si nanoparticles. *Appl. Phys. Lett.*, 80:841, 2002.

[16] G. Belomoin, J. Therrien, and M. Nayfeh. Oxide and hydrogen capped ultrasmall blue luminescent si nanoparticles. *Appl. Phys. Lett.*, 77:779, 2000.

[17] M.H. Nayfeh, S Rao, O. Nayfeh, A. Smith, and J. Therrien. Uv photodetectors with thin-film si nanoparticle active medium. *IEEE Trans. Nanotech.*, 4:660, 2005.

[18] Osama M. Nayfeh, Dimitri A. Antoniadis, Kevin Mantey, and Munir H. Nayfeh. Memory effects in metal-oxide-semiconductor capacitors incorporating dispensed highly monodisperse 1 nm silicon nanoparticles. *Applied Physics Letters*, 90(15), APR 9 2007.

[19] A Smith, G Belomoin, MH Nayfeh, and T Nayfeh. Spatially selective electrochemical deposition of composite films of metal and luminescent Si nanoparticles. *Chemical Physics Letters*, 372(3-4):415–418, APR 29 2003.

[20] Gang Wang, Kevin Mantey, Munir H. Nayfeh, and Siu-Tung Yau. Enhanced amperometric detection of glucose using Si-29 particles. *Applied Physics Letters*, 89(24), DEC 11 2006.

[21] MIJ Beale, JD Benjamin, MJ Uren, NG Chew, and AG Cullis. An Experimental and Theoretical-Study of the Formation and Microstructure of Porous Silicon. *Journal of Crystal Growth*, 73(3):622–636, DEC 1985.

[22] M Christophersen, J Carstensen, S Ronnebeck, C Jager, W Jager, and H Foll. Crystal orientation dependence and anisotropic properties of macropore formation of p- and n-type silicon. *Journal of the Electrochemical Society*, 148(6):E267–E275, JUN 2001.

[23] Satish Rao. *A study of the molecular behavior in the vibronic and excitonic properties of silicon nanoparticles.* PhD thesis, University of Illinois at Urbana-Champaign, Champaign, IL USA, 2006.

[24] Z. Yamani, O. Gurdal, A. Alaql, and M. Nayfeh. Correlation of diffuse scattering with nanocrystallite size in porous silicon using transmission microscopy. *J. App. Phys.*, 85:8050, 1999.

[25] Z. Yamani, S. Ashhab, A. Nayfeh, W. H. Thompson, and M. Nayfeh. Red to green rainbow photoluminescence from unoxidized silicon nanocrystallites. *J. Appl. Phys.*, 83:3929, 1998.

[26] Osama M. Nayfeh, Dimitri A. Antoniadis, Kevin Mantey, and Munir H. Nayfeh. Uniform delivery of silicon nanoparticles on device quality substrates using spin coating from isopropyl alcohol colloids. *Applied Physics Letters*, 94(4), JAN 26 2009.

[27] Joel Therrien. *Size dependence of the electrical characteristics of silicon nanoparticles.* PhD thesis, University of Illinois at Urbana-Champaign, Champaign, IL USA, 2003.

[28] D. Nielsen, L. Abuhassan, M. Alchihabi, A. Al-Muhanna, Jon Host, and M. H. Nayfeh. Current-less anodization of intrinsic silicon powder grains: Formation of fluorescent Si nanoparticles. *Journal of Applied Physics*, 101(11), JUN 1 2007.

[29] JP Proot, C Delerue, and G Allan. Electronic-structure and Optical-Properties of Silicon Crystallites - Application to Porous Silicon. *Applied Physics Letters*, 61(16):1948–1950, OCT 19 1992.

[30] LW Wang and A Zunger. Electronic-structure Pseudopotential Calculations of Large (Approximate-to-1000 Atoms) Si Quantum Dots. *Journal of Physical Chemistry*, 98(8):2158–2165, FEB 24 1994.

[31] M Rohlfing and SG Louie. Electron-hole excitations in semiconductors and insulators. *Physical Review Letters*, 81(11):2312–2315, SEP 14 1998.

[32] LX Benedict, A Puzder, AJ Williamson, JC Grossman, G Galli, JE Klepeis, JY Raty, and O Pankratov. Calculation of optical absorption spectra of hydrogenated Si clusters: Bethe-Salpeter equation versus time-dependent local-density approximation. *Physical Review B*, 68(8), AUG 15 2003.

[33] B Delley and EF Steigmeier. Quantum Confinement in Si Nanocrystals. *Physical Review B*, 47(3):1397–1400, JAN 15 1993.

[34] S Ogut, JR Chelikowsky, and SG Louie. Quantum confinement and optical gaps in Si nanocrystals. *Physical Review Letters*, 79(9):1770–1773, SEP 1 1997.

[35] I Vasiliev. Optical excitations in small hydrogenated silicon clusters: comparison of theory and experiment. *PHYSICA STATUS SOLIDI B-BASIC RESEARCH*, 239(1):19–25, SEP 2003.

[36] AJ Williamson, JC Grossman, RQ Hood, A Puzder, and G Galli. Quantum Monte Carlo calculations of nanostructure optical gaps: Application to silicon quantum dots. *Physical Review Letters*, 89(19), NOV 4 2002.

[37] L. Mitas, J. Therrien, R. Twesten, G. Belomoin, and M.H. Nayfeh. Effect of surface reconstruction on the structural prototypes of ultrasmall ultrabright si-29 nanoparticles. *Appl. Phys. Lett.*, 78:1918, 2001.

[38] L. Wagner, A. Puzder, A. Williamson, Z. Helms, J. Grossman, L. Mitas, G. Galli, and M. Nayfeh. The structure and stokes shift of hydrogenated silicon nanoclusters, 2004.

[39] C. Delerue, G. Allan, and M. Lannoo. Theoretical aspects of the luminescence of porous silicon. *Phys. Rev. B*, page 11024, 1993.

[40] A. Puzder, A. Williamson, J. Grossman, and G. Galli. Computational studies of the optical emission of silicon nanocrystals. *J. Am. Chem. Soc.*, 125:2786, 2003.

[41] A. Puzder, A. Williamson, F. Reboredo, and G. Galli. Structural stability and optical properties of nanomaterials with reconstructed surfaces. *Phys. Rev. Lett.*, 91:157405, 2003.

[42] E. Draeger, J. Grossman, A. Williamson, and G. Galli. Optical properties of passivated silicon nanoclusters: The role of synthesis. *J. Chem. Phys.*, 120:10807, 2004.

[43] I Vasiliev and RM Martin. Optical properties of hydrogenated silicon clusters with reconstructed surfaces. *Physica Status Solidi B-Basic Research*, 233(1):5–9, SEP 2002.

[44] M. Nishida. Electronic structure calculations of si quantum dot: effects of dimer formation and oxidation on electronic and optical properties. *Phys. Lett. A*, 323:449, 2004.

[45] M Nishida. Electronic state calculations of Si quantum dots: Oxidation effects. *Physical Review B*, 69(16), APR 2004.

[46] M. Nishida. Effect of oxidation on the electronic structure of a si_{29} quantum dot: Calculations of redshifts in energy gap. *J. Appl. Phys.*, 99:053708, 2006.

[47] C. S. Garoufalis and A. D. Zdetsis. High accuracy calculations of the optical gap and absorption spectrum of oxygen contaminated si nanocrystals. *Phys. Chem. Chem. Phys.*, 8:808, 2006.

[48] I Vasiliev, JR Chelikowsky, and RM Martin. Surface oxidation effects on the optical properties of silicon nanocrystals. *Physical Review B*, 65(12), MAR 15 2002.

[49] C. S. Garoufalis and A. D. Zdetsis. Optical properties of ultra small Si nanoparticles: potential role of surface reconstruction and oxygen contamination. *Journal of Mathematical Chemistry*, 46(3, Sp. Iss. SI):952–961, OCT 2009.

[50] S. Rao, J. Sutin, R. Clegg, E. Gratton, M.H. Nayfeh, S. Habbal, A. Tsolakidis, and R. Martin. Excited states of tetrahedral single-core si_{29} nanoparticles. *Phys. Rev. B*, 69:205319, 2004.

[51] O Lehtonen and D Sundholm. Density-functional studies of excited states of silicon nanoclusters. *Physical Review B*, 72(8), AUG 2005.

[52] Nurbosyn U. Zhanpeisov and Hiroshi Fukurnura. What Silicon Nanocluster is Most Likely Formed in Etching Experiments? Theoretical DFT Study. *Journal of Nanoscience and Nanotechnology*, 8(7):3478–3482, JUL 2008.

[53] D.A. Long. *Raman Spectroscopy*. McGraw-Hill International Book Company, London, UK, 1977.

[54] Peter F. Bernath. *Spectra of Atoms and Molecules*. Oxford University Press, New York, NY, USA, 2nd edition, 2005.

[55] Attila Szabo and Neil S. Ostlund. *Modern Quantum Chemistry: Introduction to Advanced Electronic Structure Theory*. Dover Publications, Mineola, New York, USA, 1st, revised edition, 1996.

[56] ER Davidson and D Feller. Basis Set Selection For Molecular Calculations. *Chemical Reviews*, 86(4):681–696, AUG 1986.

[57] N.J. Harris. A systematic theoretical study of harmonic vibrational frequencies and deuterium isotope fractionation factors for small molecules. *J. Phys. Chem.*, 99:14689, 1995.

[58] KK Irikura, RD Johnson, and RN Kacker. Uncertainties in scaling factors for ab initio vibrational frequencies. *Journal of Physical Chemistry A*, 109(37):8430–8437, SEP 22 2005.

[59] A.P. Scott and L. Radom. Harmonic vibrational frequencies: An evaluation of hartree-fock, moller-plesset, quadratic configuration interaction, density functional theory, and semiempirical scale factors. *J. Phys. Chem.*, 100:16502, 1996.

[60] National Institute of Standards and Technology. Computational chemistry comparison and benchmark database (cccbdb).

[61] Leonid Izrailevich Trakhtenberg, Sheng Hsien Lin, and O. J. Ilegbusi. *Physico-chemical phenomena in thin films and at solid surfaces.* Academic Press, San Diego, CA, USA, 1st edition, 2007.

[62] W. J. Staszewski, Christian Boller, and Geoffrey R. Tomlinson. *Health monitoring of aerospace structures: smart sensor technologies and signal processing.* John Wiley and Sons, Chichester, West Sussex, UK, 1st edition, 2004.

[63] M.W. Schmidt, K.K Baldridge, J.A. Boatz, S.T. Elbert, M.S. Gordon, J.H. Jensen, S. Koseki, N. Matsunaga, K.A. Nguyen, S.J. Su, T.L. Windus, M. Dupuis, and J.A. Montgomery. General atomic and molecular electronic structure system. *J. Comp. Chem.*, 14:1347, 1993.

[64] M.S. Gordon and M.W. Schmidt. *Advances in electronic structure theory: GAMESS a decade later.* Elsevier, Amsterdam, 2005.

[65] http://www.msg.ameslab.gov/gamess/gamess.html.

[66] R Krishnan, JS Binkley, R Seeger, and JA Pople. Self-Consistent Molec-ular-Orbital Methods. XX. Basis Set for Correlated Wave-Functions. *Journal of Chemical Physics*, 72(1):650–654, 1980.

[67] AD McClean and GS Chandler. Contracted Gaussian-Basis Sets for Molecular Calculations. I. 2nd Row Atoms, Z=11-18. *Journal of Chemical Physics*, 72(10):5639–5648, 1980.

[68] Satish Rao, Kevin Mantey, Joel Therrien, Adam Smith, and Munir Nayfeh. Molecular behavior in the vibronic and excitonic properties of hydrogenated silicon nanoparticles. *Physical Review B*, 76(15), OCT 2007.

[69] A. H. Kuptsov and German Nikolaevich Zhizhin. *Handbook of Fourier Transform Raman and Infrared Spectra of Polymers*. Elsevier, Amsterdam, The Netherlands, 1998.

[70] HORIBA Jobin Yvon Inc. Raman bands: Raman data and analysis.

[71] http://www.chemcraftprog.com.

[72] T Shimaga, Y Katayama, K Nakagawa, H Matsubara, M Migitaka, and E Maruyama. Raman-Scattering in Low Wavenumber Region as a New Probe to Structural-Properties of Microcrystalline Silicon. *JOURNAL OF NON-CRYSTALLINE SOLIDS*, 59-6(DEC):783–786, 1983.

[73] J. Zi, H. Buscher, C. Falter, W. Ludwig, K. Zhang, and X. Xie. Raman shifts in si nanocrystals. *Appl. Phys. Lett.*, 69:200, 1996.

[74] I.H. Campbell and P.M. Fauchet. The effects of microcrystal size and shape on the one phonon raman spectra of crystalline semiconductors. *Solid Stat. Comm.*, 58:739, 1986.

[75] GE Jellison, FA Modine, CW White, RF Wood, and RT Young. Optical-Properties of Heavily Doped Silicon Between 1.5 and 4.1 eV. *Physical Review Letters*, 46(21):1414–1417, 1981.

[76] Milan Sykora, Lorenzo Mangolini, Richard D. Schaller, Uwe Kortshagen, David Jurbergs, and Victor I. Klimov. Size-dependent intrinsic radiative decay rates of silicon nanocrystals at large confinement energies. *Physical Review Letters*, 100(6), FEB 15 2008.

[77] D Kovalev, H Heckler, G Polisski, and F Koch. Optical properties of si nanocrystals. *Physica Status Solidi B-Basic Research*, 215(2):871–932, OCT 1999.

[78] LE Brus, PF Szajowski, WL Wilson, TD Harris, S Schuppler, and PH Citrin. Electronic Spectroscopy and Photophysics of Si Nanocrystals - Relationship to Bulk C-Si and Porous Si. *JOURNAL OF THE AMERICAN CHEMICAL SOCIETY*, 117(10):2915–2922, MAR 15 1995.

[79] AP Alivisatos. Semiconductor clusters, nanocrystals, and quantum dots. *SCIENCE*, 271(5251):933–937, FEB 16 1996.

[80] W. D. A. M. de Boer, D. Timmerman, K. Dohnalova, I. N. Yassievich, H. Zhang, W. J. Buma, and T. Gregorkiewicz. Red spectral shift and enhanced quantum efficiency in phonon-free photoluminescence from silicon nanocrystals. *Nature Nanotechnology*, 5(12):878–884, DEC 2010.

[81] M Nirmal and L Brus. Luminescence photophysics in semiconductor nanocrystals. *Accounts of Chemical Research*, 32(5):407–414, MAY 1999.

[82] SH Tolbert, AB Herhold, CS Johnson, and AP Alivisatos. Comparison of Quanum Confinement Effects on the Electronic Absorption-Spectra of Direct and Indirect Gap Semiconductor Nanocystals. *Physical Review Letters*, 73(24):3266–3269, DEC 12 1994.

[83] Adam Smith. *A Time-Resolved Fluorescence Study of Silicon Nanoparticles: Testing the Dimer Stretching Model*. PhD thesis, University of Illinois at Urbana-Champaign, Champaign, IL USA, 2008.

[84] VSY Lin, K Motesharei, KPS Dancil, MJ Sailor, and MR Ghadiri. A porous silicon-based optical interferometric biosensor. *Science*, 278(5339):840–843, OCT 31 1997.

[85] J Harper and MJ Sailor. Detection of nitric oxide and nitrogen dioxide with photoluminescent porous silicon. *Analytical Chemistry*, 68(21):3713–3717, NOV 1 1996.

[86] Qi Wang, Hongjun Ni, Annette Pietzsch, Franz Hennies, Yongping Bao, and Yimin Chao. Synthesis of water-dispersible photoluminescent silicon nanoparticles and their use in biological fluorescent imaging. *Journal of Nanoparticle Research*, 13(1):405–413, JAN 2011.

[87] Folarin Erogbogbo, Ken-Tye Yong, Indrajit Roy, GaiXia Xu, Paras N. Prasad, and Mark T. Swihart. Biocompatible luminescent silicon quantum dots for imaging of cancer cells. *ACS Nano*, 2(5):873–878, MAY 2008.

[88] Kevin Mantey, Matthew Kwit, M. H. Nayfeh, Ashok Kumar, Larry D. Stephenson, and Andrew J. Nelson. Measurement of the photostability of silicon nanoparticles under UVA and near infrared irradiation. *Journal of Applied Physics*, 107(6), MAR 15 2010.

[89] E Rogozhina, G Belomoin, A Smith, L Abuhassan, N Barry, O Akcakir, PV Braun, and MH Nayfeh. Si-N linkage in ultrabright, ultrasmall Si nanoparticles. *APPLIED PHYSICS LETTERS*, 78(23):3711–3713, JUN 4 2001.

[90] O Akcakir, J Therrien, G Belomoin, N Barry, JD Muller, E Gratton, and M Nayfeh. Detection of luminescent single ultrasmall silicon nanoparticles using fluctuation correlation spectroscopy. *Applied Physics Letters*, 76(14):1857–1859, APR 3 2000.

[91] Gaiping Li, Junfeng Zhai, Dan Li, Xiaona Fang, Hong Jiang, Qingzhe Dong, and Erkang Wang. One-pot synthesis of monodispersed ZnS nanospheres with high antibacterial activity. *Journal of Materials Chemistry*, 20(41):9215–9219, 2010.

[92] Kouki Fujioka, Masaki Hiruoka, Keisuke Sato, Noriyoshi Manabe, Ryosuke Miyasaka, Sanshiro Hanada, Akiyoshi Hoshino, Richard D. Tilley, Yoshinobu Manome, Kenji Hirakuri, and Kenji Yamamoto. Luminescent passive-oxidized silicon quantum dots as biological staining labels and their cytotoxicity effects at high concentration. *Nanotechnology*, 19(41), OCT 15 2008.

[93] Joseph R. Lakowicz. *Principles of Fluorescence Spectroscopy.* Springer, New York, NY, USA, 3rd edition, 2006.

[94] Michael Kasha. Characterization of electronic transitions in complex molecules. *Discussions of the Faraday Society*, 9:14–19, 1950.

[95] M. Nayfeh, N. Rigakis, and Z. Yamani. Photoexcitation of si-si surface states in nanocrystallites. *Phys. Rev. B*, 56:2079, 1997.

[96] L.H. Thomas. The calculation of atomic fields. *Proc. Cambridge Phil. Roy. Soc.*, 23:542–548, 1927.

[97] E Fermi. Un metodo statistico per la determinazione di alcune priorieta dell'atmoe. *Rend. Accad. Naz. Lincei*, 6:602–607, 1927.

[98] P.A.M. Dirac. Note on exchange phenomena in the Thomas-Fermi atom. *Proc. Cambridge Phil. Roy. Soc.*, 26:376–385, 1930.

[99] Richard M. Martin. *Electronic Structure: Basic Theory and Practice Methods.* Cambridge University Press, Cambridge, UK, 2004.

[100] P. Hohenberg and W. Kohn. Inhomogeneous electron gas. *Phys. Rev.*, 136:B864–871, 1964.

[101] U. von Barth and L. Hedin. A local exchange-correlation potential for the spin polarized case: I. *J. Phys. C*, 5:1692, 1972.

[102] G. Vignale and M. Rosalt. Current- and spin-density-functional theory for inhomogeneous electronic systems in strong magnetic fields. *Physical Review B*, 10:1319–1327, 1974.

[103] W. Kohn and L. Sham. Self-consistent equations including exchange and correlation effects. *Phys. Rev.*, 140:A1133–1138, 1965.

[104] D. Ceperley and B. Alder. Ground state of the electron gas by a stochastic method. *Phys. Rev. Lett.*, 45:566, 1980.

[105] J.P. Perdew and A. Zunger. Self-interaction correction to density-functional approximations for many-electron systems. *Physical Review B*, 23:5048, 1981.

[106] S. Vosko, L. Wilk, and M. Nusair. Accurate spin-dependent electron liquid correlation energies for local spin density calculations: a critical analysis. *Can. J. Phys.*, 58:1200, 1983.

[107] A.D. Becke. Density-functional exchange-energy approximation with correct asymptotic behavior. *Phys. Rev. A*, 38:3098–3100, 1988.

[108] C. Lee, W. Yang, and R.G. Parr. Developement of the colle-salvetti correlation-energy formula into a functional of the electron density. *Phys. Rev. B*, 37:785–789, 1988.

[109] E. Runge and E.K.U. Gross. Density-functional theory for time-dependent systems. *Physical Review Letters*, 52:997–1000, 1984.

[110] F Furche. On the density matrix based approach to time-dependent density functional response theory. *JOURNAL OF CHEMICAL PHYSICS*, 114(14):5982–5992, APR 8 2001.

[111] F Furche and R Ahlrichs. Adiabatic time-dependent density functional methods for excited state properties. *JOURNAL OF CHEMICAL PHYSICS*, 117(16):7433–7447, OCT 22 2002.

[112] TURBOMOLE V6.3 2011, a development of University of Karlsruhe and Forschungszentrum Karlsruhe GmbH, 1989-2007, TURBOMOLE GmbH, since 2007; available from
`http://www.turbomole.com`.

[113] F. Weigend and R. Ahlrichs. Balanced basis sets of split valence, triple zeta valence and quadruple zeta valence quality for H to Rn: Design an assessment of accuracy. *Phys. Chem. Chem. Phys.*, 7:3297, 2005.

[114] F. Weigend, M. Haser, H. Patzelt, and R. Ahlrichs. RI-MP2: Optimized Auxiliary Basis Sets and Demonstration of Efficiency. *Chem. Phys. Letters*, 294:143, 1998.

[115] A. Schafer, C. Huber, and R. Ahlrichs. Fully Optimized Contracted Gaussian Basis Sets of Triple Zeta Valence Quality for Atoms Li to Kr. *J. Chem. Phys.*, 100:5829, 1994.

[116] Munir H. Nayfeh, Huw Morgan, Kevin Mantey, Shadia Habbal, Adam Smith, Jack Pobari, Nigel Poolten, Geraint Jones, and Andy Evans. Bright trion states above the ionization limit in 1 nm hydrogenated si29 nanoparticles. Currently in submission process, 2011.

[117] Arthur E. Martell and Robert D. Hancock. *Metal Complexes in Aqueous Solutions.* Plenum Press, New York, NY, 1996.

[118] GG Nunes, RCR Bottini, DM Reis, PHC Camargo, DJ Evans, PB Hitchcock, GJ Leigh, EL Sa, and JF Soares. New Fe-II starting materials: preparation, characterisation and structural features of iron halide complexes with alcohol ligands. *INORGANICA CHIMICA ACTA*, 357(4):1219–1228, MAR 10 2004.

[119] J Tomasi, B Mennucci, and R Cammi. Quantum mechanical continuum solvation models. *CHEMICAL REVIEWS*, 105(8):2999–3093, AUG 2005.

[120] A Klamt and G Schuurmann. COSMO - A new approach to dielectric screening in solvents with explicit expressions for the screening energy and its gradient. *JOURNAL OF THE CHEMICAL SOCIETY-PERKIN TRANSACTIONS 2*, (5):799–805, MAY 1993.

[121] J.D. Jackson. *Classical Electrodynamics.* Wiley, New York, 3rd edition, 1975.

[122] National Institute of Standards and Technology. Atomic reference data for electronic structure calculations.

[123] Nino Russo, Dennis R. Salahub, and Malgorzata Witko. *Metal-ligand interactions: molecular-, nano-, micro-, and macro-systems in complex environments.* Kluwer Academic Publishers, Dordrecht, The Netherlands, 2003.

[124] David R. Lide. *CRC Handbook of Chemistry and Physics.* CRC Press, 89th edition, 2008.

[125] Luciana Guimaraes, Heitor Avelino de Abreu, and Helio Anderson Duarte. Fe(II) hydrolysis in aqueous solution: A DFT study. *CHEMICAL PHYSICS*, 333(1):10–17, MAR 6 2007.

[126] Vyacheslav S. Bryantsev, Mamadou S. Diallo, Adri C. T. van Duin, and William A. Goddard, III. Hydration of copper(II): New insights from density functional theory and the COSMO solvation model. *JOURNAL OF PHYSICAL CHEMISTRY A*, 112(38):9104–9112, SEP 25 2008.

[127] Vyacheslav S. Bryantsev, Mamadou S. Diallo, and William A. God-dard, III. Calculation of solvation free energies of charged solutes using mixed cluster/continuum models. *JOURNAL OF PHYSICAL CHEMISTRY B*, 112(32):9709–9719, AUG 14 2008.

[128] HA De Abreu, L Guimaraes, and HA Duarte. Density-functional theory study of iron(III) hydrolysis in aqueous solution. *JOURNAL OF PHYSICAL CHEMISTRY A*, 110(24):7713–7718, JUN 22 2006.

[129] Gabriel Aullon and Santiago Alvarez. Oxidation states, atomic charges and orbital populations in transition metal complexes. *THEORETICAL CHEMISTRY ACCOUNTS*, 123(1-2):67–73, MAY 2009.

[130] Anil Kumar De. *A Text Book of Inorganic Chemistry*. New Age International, Daryaganj, New Delhi, 9th edition, 2003.

[131] W.P. Griffith, J. Lewis, and G. Wilkinson. Some nitric oxide complexes of iron and copper. *J. Chem. Soc.*, pages 3993–3998, 1958.

[132] Anatoly F. Vanin. Dinitrosyl iron complexes with thiolate ligands: Physico-chemistry, biochemistry and physiology. *Nitric Oxide*, 21(1):1 – 13, 2009.

[133] Christopher A. Reed. *Iron(I) and Iron(IV) Porphyrins*, chapter 16, pages 333–356.